

**STRUCTURAL PERFORMANCE OF A FULL-DEPTH
PRECAST CONCRETE BRIDGE DECK SYSTEM**

A Thesis

by

THOMAS JOHN MANDER

Submitted to the Office of Graduate Studies of
Texas A&M University
in partial fulfillment of the requirements for the degree of
MASTER OF SCIENCE

August 2009

Major Subject: Civil Engineering

**STRUCTURAL PERFORMANCE OF A FULL-DEPTH
PRECAST CONCRETE BRIDGE DECK SYSTEM**

A Thesis

by

THOMAS JOHN MANDER

Submitted to the Office of Graduate Studies of
Texas A&M University
in partial fulfillment of the requirements for the degree of
MASTER OF SCIENCE

Approved by:

Chair of Committee,	Monique Hite Head
Committee Members,	Rashid Abu Al-Rub
	Julian Kang
Head of Department,	David Rosowsky

August 2009

Major Subject: Civil Engineering

ABSTRACT

Structural Performance of a Full-Depth Precast Concrete Bridge Deck System.

(August 2009)

Thomas John Mander, B.E. (Hons), University of Canterbury

Chair of Advisory Committee: Dr. Monique Hite Head

Throughout the United States accelerated bridge construction is becoming increasingly popular to meet growing transportation demands while keeping construction time and costs to a minimum. This research focuses on eliminating the need to form full-depth concrete bridge deck overhangs, accelerating the construction of concrete bridge decks, by using full-depth precast prestressed concrete deck panels. Full-depth precast overhang panels in combination with cast-in-place (CIP) reinforced concrete are experimentally and analytically investigated to assess the structural performance. Experimental load-deformation behavior for factored AASHTO LRFD design load limits is examined followed by the collapse capacity of the panel-to-panel seam that exists in the system. Adequate strength and stiffness of the proposed full-depth panels deem the design safe for implementation for the Rock Creek Bridge in Fort Worth, Texas. New failure theories are derived for interior and exterior bridge deck spans as present code-based predictions provide poor estimates of the ultimate capacity. A compound shear-flexure failure occurs at interior bays between the CIP topping and stay-in-place (SIP) panel. Overhang failure loads are characterized as a mixed failure of flexure on the loaded panel and shear at the panel-to-panel seam. Based on these results design recommendations are presented to optimize the reinforcing steel layout used in concrete bridge decks.

ACKNOWLEDGEMENTS

The success of this thesis would not have been possible without the input from a number of people. Firstly, I would like to thank my research partners Captain Matt Henley and Reece Scott for their endless support in the lab throughout the experimental phase of this thesis. I would also like to acknowledge the help on John Orsak, an undergraduate assistant, who dedicated significant time in the lab. The experimental work was a significant undertaking in time and effort; an experience that was much better in outcome and enjoyment due to the contributions of time and effort of Matt Henley, Reece Scott and John Orsak.

Deep gratitude must be given to Dr. Monique Hite Head, my thesis advisor, for her guidance, advice and financial support. I would like to thank Dr. Rashid Abu Al-Rub from the Civil Engineering Department and Dr. Julian Kang from the Construction Science Department, for serving on my committee and providing their support and professional advice. The input provided from my committee members has been useful in achieving a high standard of results from both the experimental and analytical studies.

The experimental work presented in this thesis was funded by the Texas Department of Transportation (Project 0-6100) for which Dr. David Trejo was the Research Supervisor. I am grateful to have been involved in this project, especially as the tested design is being used for the Rock Creek Bridge in Fort Worth, Texas. Gratitude is given to Dr. Peter Keating and Mr. Matt Potter for their guidance and expertise during the experimental phase of work in the High-Bay Structural and Materials Testing Laboratory at Texas A&M.

Finally, a special thank you to all of my family and friends who have been supportive throughout this project and entire degree, making life much more enjoyable and balanced over the past 18 months.

NOMENCLATURE

AASHTO	American Association of State Highway and Transportation Officials
ACI	American Concrete Institute
ASTM	American Society for Testing and Materials
C-BAR	precast panel-to-panel reinforcing steel tie bar
CIP	cast-in-place
HBSMTL	High-Bay Structural and Materials Testing Laboratory
IM	dynamic load allowance factor
LRFD	Load and Resistance Factor Design
NCHRP	National Cooperative Highway Research Program
R-BAR	conventional shear connection for CIP or SIP panel construction
SIP	stay-in-place
TR	threaded rod shear connection
TTI	Texas Transportation Institute
TxDOT	Texas Department of Transportation
U-BAR	embedded reinforcing steel lifting bar in precast panels
Z-BAR	reinforcing steel bar cast in precast panels to prevent overturning
w/p	water-to-powder ratio
A_b	area of individual reinforcing bar
b_1	short side of reaction area
b_2	long side of reaction area
[C]	matrix of finite differences coefficients
d_b	nominal diameter of reinforcing bar
D	average effective depth of section
E_c	modulus of elasticity of plain concrete
E_{ci}	initial elastic modulus of plain concrete
E_s	modulus of elasticity of reinforcing steel

E_{sec}	secant modulus of plain concrete
E_{sh}	elastic modulus at onset of strain-hardening of steel reinforcing
EA	axial rigidity of bridge deck slab section
EI	flexural rigidity of bridge deck slab section
EZ	non-linear coupling between axial load and bending moment
f'_c	compressive strength of plain concrete
f_c	stress of concrete for given strain, ϵ_c
f_{cu}	compressive strength of grout
f_s	stress of steel reinforcing for given strain, ϵ_s
f_{su}	ultimate stress of steel reinforcing
f_t	diagonal tensile strength of concrete
f_u	ultimate strength of steel
f_{uf}	tensile strength of shear connector
f_y	reinforcement yield stress
f_{yf}	yield stress of shear connector
H	depth of slab
l_d	development length of mild steel reinforcing bar
l_x	length of the yield lines in transverse direction
l_y	length of the yield lines in longitudinal direction
l_x^*	modified length of the yield lines in transverse direction
l_y^*	modified length of the yield lines in longitudinal direction
M_x	positive moment capacity in transverse direction
M_y	positive moment capacity in longitudinal direction
M'_x	negative moment capacity in transverse direction
M'_y	negative moment capacity in longitudinal direction
N	applied horizontal axial load on bridge deck
P_f	flexural component of failure load of SIP panels
P_u	ultimate failure load of slab
p	shape parameter based on the slope of the strain-hardening curve

V_c	punching shear capacity of slab
w_d	self-weight of slab
x	transverse direction of bridge axis
y	longitudinal direction of traffic of bridge axis
z	vertical displacement of bridge deck slab
α_x	rotation of slab about yield line about transverse axis
α_y	rotation of slab about yield line about longitudinal axis
β_c	ratio of long side of reaction area to short side (b_2/b_1)
γ	finite differences scaling factor for unevenly spaced nodes
Δx	horizontal spacing of displacement transducers
δ	arbitrary vertical displacement at the location that P_u is applied
δ_{edge}	arbitrary vertical displacement at the slab overhang edge
ε_c	strain of plain concrete
ε_{co}	compressive crushing strain of plain concrete
ε_o	strain of deck section taken at some reference point
ε_s	strain of steel reinforcing
ε_{sh}	strain at onset of strain-hardening of steel reinforcing
ε_{su}	ultimate strain of steel reinforcing
ε_{to}	ultimate tensile strain of plain concrete
ε_y	yield strain of steel reinforcing
θ	angle (in degrees) between horizontal and assumed failure plane
Φ_f	inferred curvature at failure load
Φ_y	calculated yield curvature

TABLE OF CONTENTS

ABSTRACT		iii
ACKNOWLEDGEMENTS		iv
NOMENCLATURE.....		v
TABLE OF CONTENTS		viii
LIST OF FIGURES.....		xi
LIST OF TABLES		xv
 CHAPTER		
I	INTRODUCTION.....	1
	1.1 Research Motivation	1
	1.2 Research Objectives	2
	1.3 Organization of Thesis	2
II	STATE-OF-THE-PRACTICE AND –ART.....	4
	2.1 Introduction	4
	2.2 State-of-the-Practice.....	4
	2.2.1 Partial-depth stay-in-place (SIP) panels.....	4
	2.2.2 Full-depth precast panels.....	9
	2.2.3 Example of conventional construction in College Station, Texas	15
	2.3 State-of-the-Art	19
	2.3.1 Full-depth overhang panel design	19
	2.3.2 Precast construction of full-depth panels	20
	2.3.3 Overview of full-depth overhang panel design	23
	2.3.4 Key construction and design issues.....	25
	2.3.5 Alternative construction: lab-cast panels	34
III	EXPERIMENTAL INVESTIGATION	38
	3.1 Introduction	38
	3.2 Experimental Design	38
	3.2.1 Basis of design for double-panel specimens	38

CHAPTER	Page
3.2.2 Details of Specimen 1	40
3.2.3 Details of Specimen 2	43
3.2.4 Material properties	45
3.2.5 Loading protocol	49
3.3 Experimental Testing Plan	51
3.3.1 AASHTO LRFD loading	51
3.3.2 Overhang failure load.....	54
3.3.3 Interior loads	56
3.3.4 Instrumentation.....	57
3.4 Experimental Grout Track.....	61
 IV EXPERIMENTAL RESULTS.....	 64
4.1 Introduction	64
4.2 AASHTO Overhang Seam Load.....	64
4.3 AASHTO Overhang Mid-panel (Quarter-point) Loads	66
4.4 Overhang Failure Loads	67
4.5 Interior Loads	70
4.6 Additional Measured Strains.....	73
4.7 Discussion	74
4.8 Experimental Conclusions.....	75
 V ANALYTICAL INVESTIGATION: EXTERIOR	 77
5.1 Introduction	77
5.2 Failure Load Analysis	80
5.2.1 Yield line theory	80
5.2.2 Modified yield line theory.....	81
5.2.3 Yield line analysis	82
5.2.4 Mixed shear-yield line mechanism at the seam	84
5.3 Experimental Displacement Profiles and Inferred Curvature Results	84
5.3.1 Load Case 1.3.....	85
5.3.2 Load Case 1.6.....	86
5.3.3 Load Case 2.7.....	89
5.3.4 Load Case 2.3.....	90
5.4 Analytical Results	93
5.4.1 Load Case 1.3.....	94
5.4.2 Load Cases 1.6 and 2.7.....	95
5.4.3 Load Case 2.3.....	98
5.5 Discussion	99
5.6 Conclusions	100

CHAPTER	Page
VI	ANALYTICAL INVESTIGATION: INTERIOR 102
	6.1 Introduction 102
	6.2 Modes of Failure in Bridge Decks 103
	6.2.1 Shear in CIP slabs 103
	6.2.2 Flexure in CIP slabs 105
	6.2.3 Membrane action 106
	6.3 Compound Shear-Flexure Failure Mode in SIP-CIP Decks 106
	6.3.1 Shear at a panel-to-panel seam 107
	6.4 Experimental Displacement Profiles and Inferred Curvatures 107
	6.4.1 Load Case 2.4 111
	6.4.2 Load Case 2.8 111
	6.5 Results of Collapse Load Analysis 112
	6.5.1 Load Case 2.4 113
	6.5.2 Load Case 2.8 115
	6.6 Discussion 117
	6.7 Conclusions 119
VII	CONCLUSIONS 121
	7.1 Summary 121
	7.2 Design Considerations 122
	7.3 Recommendations for Future Work 124
	REFERENCES 127
	APPENDIX I 133
	APPENDIX II 138
	APPENDIX III 144
	VITA 153

LIST OF FIGURES

FIGURE		Page
1	Comparison of bridge deck construction with and without SIP panels.....	5
2	Precast construction of SIP panels	6
3	Shear connections used for CIP and SIP panel bridge deck construction	8
4	Placement of SIP panel on levelling strip	9
5	Different shear connector for steel plate girder bridges	11
6	Full-depth precast concrete deck without wearing surface (from Issa et al., 1995).....	12
7	Comparison of different transverse panel-to-panel shear keys	15
8	Construction of Rock Prairie exit bridge in College Station, TX, US – 2009	17
9	Precast construction and on-site placement of full-depth overhang panels.....	21
10	Isometric view of two adjacent precast overhang panels (Mander et al., 2009).....	23
11	Shear connections used for full-depth overhang panel bridge deck	26
12	Full-depth overhang panel-to-panel seam	27
13	Percentage of final deflections during construction (Merrill, 2002).....	28
14	Leveling bolt and haunch forming for full-depth precast overhang	29
15	Test apparatus for grout mixtures.....	32

FIGURE		Page
16	Z-bars cast into Stage I to prevent overturning of full-depth overhang panels.....	34
17	Lab-cast panel construction.....	36
18	Basis of experimental setup.....	39
19	Specimen 1 dimensions (mm).....	42
20	Specimen 2 dimensions (mm).....	44
21	Steel stress-strain curves	47
22	Schematic of experimental testing equipment.....	50
23	HL-93 design truck and design tandem loads per axle	51
24	AASHTO LRFD (2007) overhang loading position (dimensions in mm).....	53
25	Load plate positions for AASHTO LRFD (2007) overhang loads	54
26	Overhang failure loads	55
27	Load plate positions for overhang failure loads.....	55
28	Load plate positions for interior bays.....	56
29	Plan view of Specimen 1 instrumentation for overhang failure load (dimensions in mm).....	58
30	Plan view of Specimen 2 instrumentation for overhang failure load (dimensions in mm).....	59
31	Instrumentation used on bridge deck specimens.....	60
32	Experimental grout track on 4% slope	61
33	Placement of grout on experimental grout track	63
34	Force-displacement for AASHTO load at overhang midspan	66

FIGURE	Page
35	Force-displacement for AASHTO load at overhang mid-panel.....67
36	Force-displacement for overhang failure loads.....68
37	Observed failure modes for Specimens 1 and 2 overhangs69
38	Force-displacement for interior failure cases71
39	Observed failure modes for Specimens 1 and 2 interior bays.....72
40	Transverse bar strains in precast prestressed overhang of Specimen 273
41	Comparison of two overhang systems78
42	Assumed yield line mechanism for conventional overhang loaded to failure.....83
43	Load Case 1.3 – conventional overhang loaded to failure at 476 kN87
44	Load Case 1.6 – precast prestressed overhang loaded to failure at 374 kN88
45	Load Case 2.7 – lab-cast overhang loaded to failure at 298 kN.....91
46	Load Case 2.3 – precast prestressed overhang, tandem axle load loaded to failure at 360 kN92
47	Load Case 1.3; surface cracks and critical failure mode for conventional overhang95
48	Surface cracks and credible failure mechanisms for Load Case 1.6 and Load Case 2.7; the precast prestressed overhang and lab-cast overhang, respectively97
49	Load Case 2.3; surface cracks and critical failure mode for precast prestressed overhang with tandem axle load98
50	Shear-flexural failure and punching-shear failure of CIP-SIP bridge deck specimen105

FIGURE		Page
51	Load Case 2.4 – tandem axle (wheel) load on single panel, loaded to failure at 565 kN	109
52	Load Case 2.8 – tandem axle (wheel) load straddling seam, loaded to failure at 667 kN	110
53	Load Case 2.4; credible failure modes for tandem axle (wheel) load on single panel.....	114
54	Load Case 2.8; credible failure modes for tandem axle (wheel) load straddling seam.....	116
55	Schematic of potential improved panel-to-panel connections	126

LIST OF TABLES

TABLE		Page
1	Consistency values for SikaGrout™ 212.....	31
2	Method for placing haunch grout for full-depth overhang panels (adapted from Trejo et al., 2008).....	33
3	Compressive and tensile strengths of cementitious materials	46
4	Stress-strain values for steel reinforcement.....	47
5	Moment capacities (per unit width) for bridge deck sections using actual material properties	48
6	AASHTO LRFD (2007) load factors and maximum factored loads.....	52
7	Load cases for tested double-panel bridge deck specimens	65
8	Peak loads and factors of safety for ultimate failure load cases.....	74
9	Summary of yield loads and failure curvatures for longitudinal profiles.....	85
10	Exterior experimental and theoretical failure loads in kN (and experimental/theoretical load ratios)	94
11	Interior experimental and theoretical failure loads in kN (and theoretical/experimental load ratios)	112

CHAPTER I

INTRODUCTION

1.1 Research Motivation

Stay-in-place (SIP) precast panels were first used in the 1950s in Illinois, and became incorporated for use in other states in the late 1960s and early 1970s (Goldberg, 1987). One of the main difficulties with this system is forming the deck overhang to cast a full 200 mm thick deck section, which can be time consuming and potentially unsafe. SIP panels have shown to have comparable strength to full-depth cast-in-place bridge decks while adding additional value in accelerated construction, increased safety, and reduced construction costs through less on-site labor requirements (Buth et al., 1972). Furthermore, other research has shown the added value of the SIP concrete deck panels to be stronger, stiffer, and more crack-resistant when compared to completely cast-in-place (CIP) concrete decks (Tsui et al., 1986). The system proposed in this thesis uses SIP panels in the interior bays of the deck but a full-depth precast prestressed overhang at the exterior girder to reduce the need for formwork of the overhang on-site.

Full-depth, 200 mm thick, precast panels used in both interior and exterior bays have been investigated previously by Yamane et al. (1998) and Fallaha et al. (2004). These panels are placed next to each other with transverse continuity achieved using female-female grouted shear keys (Issa et al., 2003). Shear transfer between the girders and deck are achieved in the same way as the system developed in the research herein. A significant volume of grout is required for shear keys and shear pockets at all girders. Where negative moments occur, cracks may open up around shear pockets and shear keys, allowing for chloride and moisture ingress, reducing the durability of the deck system. Although these full-depth panel systems have considerable merit, they have only been adopted for field application on a few occasions. Their lack of widespread use is considered to be due to the difficulty in grading the deck within a given span.

This thesis follows the style of *Journal of Structural Engineering*.

The proposed full-depth overhang system eliminates the need for exterior formwork and utilizes SIP panels in the interior bays of the bridge deck. The system is not dissimilar to conventional bridge deck construction at interior bays, allowing for easy adaptation to the new construction process for on-site workers. This has the potential to reduce construction costs, improve safety and increase construction speed. While the interior SIP construction process is widely used, the American Association of State Highway Transportation Officials (AASHTO) Load and Resistance Factor Design (LRFD) Bridge Design Specifications (2007) do not explicitly define how to analyze such systems. A new theory is required to analyze the interaction between the SIP panels and CIP deck. This theory has the potential to improve the efficiency of bridge deck design as conventional designs have sufficient reserve capacity over the maximum AASHTO LRFD factored design load.

1.2 Research Objectives

To validate the performance and practicality of field implementation of a full-depth precast, prestressed overhang bridge deck system, the following objectives are achieved:

- a) To experimentally evaluate the panel's stiffness under normal service loads and the ultimate strength capacity per AASHTO LRFD (2007) design load criteria.
- b) To derive new theories that determine the failure load of interior and exterior bridge deck spans accurately. Existing theories provide poor estimates of the ultimate capacity of bridge decks with SIP panels. These theories tend to focus on either shear or flexure alone, without considering boundary conditions in a holistic sense. To this end, a new theory that considers a compound flexural-shear failure of interior bridge decks is presented.

1.3 Organization of Thesis

This thesis is divided into eight core chapters that together provide a comprehensive study on the use of full-depth precast prestressed overhang panels. Chapter II focuses on the state-of-the-practice of current bridge deck construction, from which construction

and design issues were assessed for the newly proposed state-of-the-art design. Experimental tests were performed on the new full-depth precast prestressed overhang panels, with the experimental design and testing plan covered in Chapter III. Experimental results from the sixteen load cases applied to the constructed bridge deck specimens are presented in Chapter IV. From the results obtained analyses are performed on the bridge deck overhangs in Chapter V, and the interior bays in Chapter VI. Chapter VII focuses on developing a finite element model for the shear connection between the full-depth overhang panels and precast concrete girders that they are seated on. Finally, Chapter VIII provides a summary of the work performed, along with design recommendations and future research.

CHAPTER II

STATE-OF-THE-PRACTICE AND -ART

2.1 Introduction

This chapter first addresses the current state-of-the-practice for new bridge deck construction using precast prestressed concrete panels. Continuous full-depth precast panels proposed by other researchers are also presented to provide background knowledge of precast bridge deck panel systems. Merits of both systems are discussed as well as construction and design issues that can be instructive in improving the new full-depth precast overhang system evaluated in this research. The latter part of this chapter covers the state-of-the-art of the full-depth precast overhang system, as recently developed by Texas Department of Transportation (TxDOT). Design and construction issues are addressed along with comparisons made with the state-of-the-practice background provided in this chapter.

2.2 State-of-the-Practice

2.2.1 *Partial-depth stay-in-place (SIP) panels*

Fig. 1(a) illustrates a monolithic cast-in-place (CIP) reinforced concrete bridge deck. This was the conventional method of new bridge deck construction up to the 1980s. Either plywood or stay-in-place (SIP) metal formwork was required throughout the entire deck to support the casting of a 200 mm thick reinforced concrete deck on-site. First used on the Illinois Tollway Project in the 1950s (Goldberg 1987), the bottom 100 mm of CIP concrete was replaced with precast prestressed concrete panels. As shown in Fig. 1(b), these panels act as SIP formwork while contributing necessary stiffness and strength to the deck system. The panels became incorporated into bridge construction in other states in the US between the 1960s and 1970s, and first used in Texas in 1963 (Merrill, 2002). Contractors showed diminutive interest in adapting to a new system until the early 1980s after which SIP panels became increasingly popular. They are now

the preferred method of construction in the state of Texas and are used in approximately 85 percent of new concrete bridge decks (Merrill, 2002). SIP panels are used on both precast prestressed concrete girders and steel girders, bridges of all lengths, and lightly (less than 15°) skewed bridges (Tadros and Baishya, 1998 and Sprinkel, 1985). For larger skews and at interior piers, where a high negative moment exists and diaphragms are poured, the deck is cast in the monolithic fashion.

SIP panels are typically 100 mm thick, 2.44 m long (in the direction of travel) and sufficiently wide to span longitudinal girders. The panels are prestressed in the direction transverse to traffic flow to allow for transport to site without developing unwanted cracks. It has also been shown by Tsui et al. (1986) that prestressed SIP panels increase the stiffness and strength of the system compared to a CIP deck. Panels rest on a continuous bedding surface on the top flange of the girders, and are placed adjacent to one another along the bridge length. A transverse connection does not exist at the panel-to-panel seam between adjacent panels. Continuity is achieved through a second stage 100mm thick CIP concrete pour that has continuous mild reinforcement. Studies of decks built using SIP panels show construction cost savings due to the reduction of required on-site labor and traffic control required (Hieber et al., 2005). However, the system is not without flaws; key construction and durability issues of the bridge deck are discussed in the next subsections, where the main focus of this research is to evaluate the strength and stiffness of a new full-depth precast overhang system designed by Texas Department of Transportation (TxDOT).

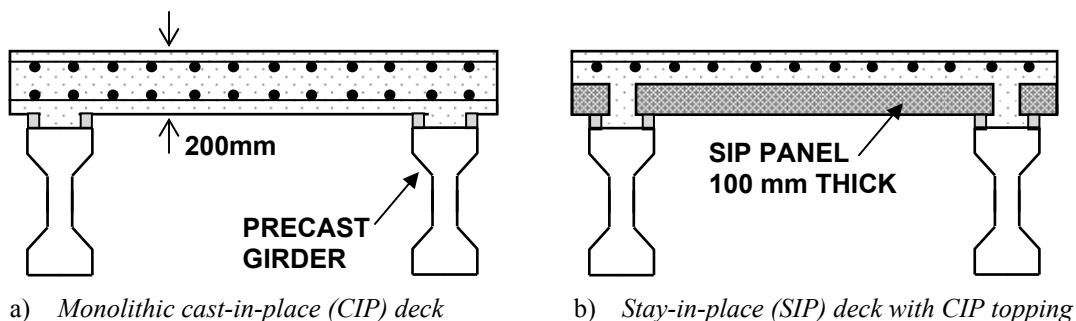


Fig. 1. Comparison of bridge deck construction with and without SIP panels

2.2.1.1 Strand extension

SIP panels are constructed in a long-line prestressing bed under controlled conditions at a precast yard. Fig. 2(a) shows the prestressing strands in a standard 100 mm deep multi-purpose steel form used to cast the panels. The strands are pretensioned to 70% of their tensile stress after which a welded wire mesh is put in place for longitudinal reinforcing steel temperature and shrinkage requirements. Steel end forms are used to separate panels to the desired length, resulting in approximately 150 mm of exposed strand between panels in the long-line bed. Once the concrete is cast and adequate strength is reached the strands are released and the forms are stripped. The exposed strands are cut midway between adjacent panels, leaving a 75 mm strand extension at either end face of the SIP panels.



a) *Long-line prestressing bed*



b) *Lifting SIP panels out of steel forms*

Fig. 2. Precast construction of SIP panels

Research conducted by Fagundo (1985), and Klingner and Bieschke (1988) showed that strand extensions did not affect the deck system behavior. Section 9.7.4.3.2 of AASHTO LRFD Bridge Design Specifications (2007) does not require strand

extensions to extend into the CIP concrete above the beams. However, the commentary suggests that the lack of strand extension may affect transverse load distribution due to lack of positive moment reinforcement over beams. It is for this reason that in the state of Texas TxDOT uses 75 to 100 mm strand extensions for SIP panels to prevent transverse cracking on the deck surface.

2.2.1.2 Composite action between SIP panels and CIP deck

Composite action between SIP panels and CIP concrete greatly affects the deck system performance. Failure to achieve an adequate bond between the two surfaces will result in reduced stiffness, strength and durability of the bridge deck system. SIP panels are typically roughened on their surface to enhance the bond with the CIP concrete deck (Goldberg, 1987 and Fagundo, 1985). Improved bonding leads to superior composite action between the two layers, increasing the moment capacity of the deck system (Goldberg, 1987). Section 9.7.4.3.3 of AASHTO LRFD Bridge Design Specifications (2007) suggests that mechanical connectors or bond enhancers need not be used between layers. It is customary in Texas to have four mild steel bent U-bars cast into the SIP panels to act as lifting points, as shown in Fig. 2(b). Research by Klingner and Bieschke (1988) concluded that these connectors did not significantly affect the bond between roughened SIP panels and CIP concrete.

2.2.1.3 Shear connections for CIP and SIP panel construction

An adequate shear connection between the concrete bridge deck and girders is imperative for a composite deck system. Composite action allows the deck to deflect simultaneously with the girder under live load. For CIP and SIP panel construction, the required interface shear is obtained through the use of shear connectors that are connected to the top girder flange and go into the bridge deck. The schematic of Fig. 3 shows typical connections used for SIP panel construction and also applies to monolithic CIP decks. The precast concrete girder of Fig. 3(a) uses a bent reinforced steel stirrup (referred to as R-bar herein) that extends above the top flange of the girder. This system has been proven to have adequate shear capacity through experiments by Scholz et al.

(2007) and Henley (2009). The stirrups are spaced according to the shear demand along the bridge, with a closer spacing at the ends of the girders. Fig. 3(b) shows the use of a plate welded girder that has steel welded studs attached to the top flange. This system has been more widely used than precast concrete girders and widely tested by Slutter and Driscoll (1965), Olgaard et al. (1971) and Xue et al. (2008).

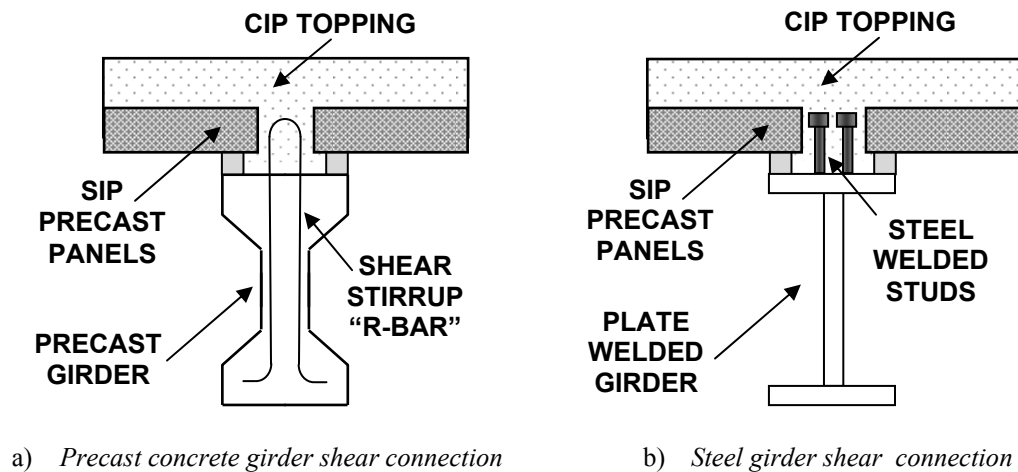


Fig. 3. Shear connections used for CIP and SIP panel bridge deck construction

2.2.1.4 Leveling and bearing of SIP panels

Achieving the correct grade using a stiff bearing surface is imperative for bridge decks using SIP panels for road user comfort and lifetime durability. The panels generally bear on high-density expanded polystyrene foam strips that are continuous along either edge of the girder top flange. A two part adhesive keeps the foam in place on the girder and bonds with the soffit of the SIP panel. Fig. 4 shows a close up of a SIP panel bearing on the foam strips along with a layer of adhesive prior to the foam being laid. The foam is cut to the correct height on-site to grade the bridge deck based on the variable camber of the girders. This can be a time consuming and tedious exercise. Expanded polystyrene foam is sufficiently stiff, which is required to prevent bearing settlement resulting in cracks of the CIP deck around the bearing area (Fagundo, 1985). Failure to provide a

stiff bearing surface will result in cracking and possibly delamination between the CIP deck and SIP panels at the girder face.

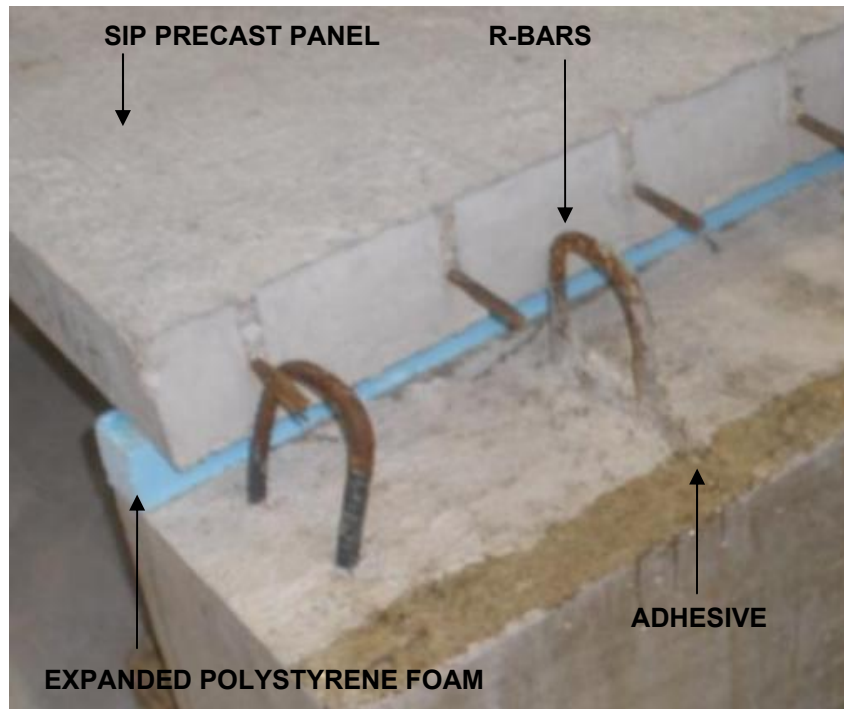


Fig. 4. Placement of SIP panel on leveling strip

2.2.2 Full-depth precast panels

Accelerated construction techniques have become increasingly popular to increase bridge deck construction speed. This is particularly advantageous in areas of high traffic where road closures are inconvenient to the public. Full-depth precast panels were first used in the United States in 1965 by Biswas (1986) to alleviate this issue while also reducing on-site construction costs. Bridges were originally used for non-composite construction, which resulted in the deck slab cracking. Composite action between full depth panels and girders was addressed in 1973 (Biswas, 1986) which improved the performance of the structures. Typically full-depth panels are used on steel girders as a shear connection is achieved more straightforward than for precast prestressed concrete

girders. Panels can be used for new bridge decks or for replacement of damaged or deteriorated CIP deck slabs.

Panels are precast the full 200 mm depth for the width of the bridge deck and overhang, requiring alternate shear connections at the girders. As with SIP panels the full-depth panels are placed adjacent to one another along the bridge axis and prestressed transverse to the direction of the vehicle travel. Shear keys at the transverse edges of the panels are formed to produce an adequate shear connection between adjacent panels. In some decks longitudinal post-tensioning is applied to close any gaps that exist at transverse seams for greater durability.

One main advantage of a full-depth precast bridge deck system is having a precast overhang, eliminating the need for onsite formwork and falsework at the overhang. However, new issues arise with the use of full-depth panels such as the need for (1) alternative shear connections, (2) design of panel-to-panel connections and (3) leveling the panels to the correct grade. These three main issues are discussed individually in the following subsections as they relate to the design of the full-depth overhang panels used in this research.

2.2.2.1 Shear connections for full-depth precast panels

As panels are full-depth and continuous over a girder, traditional shear connections discussed in Section 2.2.1.3 of this thesis can no longer be used. An adequate connection is required for full-composite action to develop. Insufficient composite action between the full-depth panel and girder will cause cracking on the bridge deck surface and at transverse joints. For this reason, a number of shear connection techniques have been researched. Fig. 5 illustrates three methods discussed in this section; shear pockets, tie down connections and bolted connections. Shear pocket connections of Fig. 5(a) are used in both precast concrete girder and steel girder construction, whereas the latter two techniques, tie down construction in Fig. 5(b) and bolted connections in Fig. 5(c) can only be used in steel girder construction.

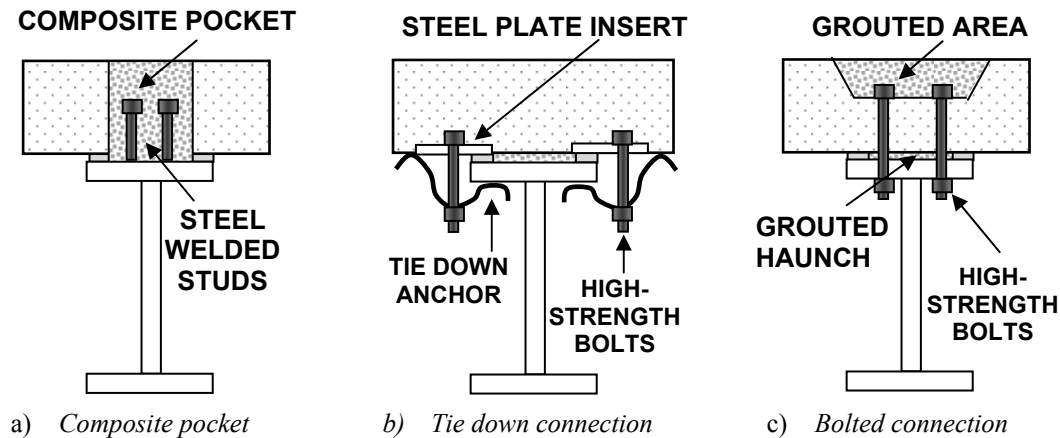


Fig. 5. Different shear connector for steel plate girder bridges

2.2.2.1.1 Shear pockets

Shear pockets are the most common method for achieving composite action between a full-depth panel and girder. For this system shear pockets (block-outs) are cast in the precast panel to provide discrete locations for shear connectors to be located. These pockets can be either rectangular or circular in shape, with the size determined on a project specific basis. Pockets are typically spaced at 850 mm or less depending on the shear demand and connector strength. Headed shear studs are commonly used for steel girders as in CIP construction. Full-depth panels have mostly been used on steel girder bridges. Issa et al. (1995) recommends the use of full-depth panels on precast prestressed girders instead of steel girders due to the increased stiffness, which results in reduced cracking and fatigue at the precast panel surface.

Limited field use of full-depth panels with prestressed concrete girders is attributed to inadequate research on the subject due to the challenges of obtaining a reliable shear connection. A coupled set of papers by Shirvani et al. (2004) and Muratli et al. (2004) provides the most comprehensive work on the subject. Research by Shirvani et al. (2004) focuses on the breakout strength of concrete anchors in tension, for which predictive methods are developed. Muratli et al. (2004) considers the breakout capacity of anchors in concrete under shear for both CIP and post-installed connectors. The study

concluded that the breakout capacity of post-installed connections was approximately 10% less than CIP connections. Further research is required on the topic to gain contractor confidence, such as looking at the strength of connectors in narrow webbed precast prestressed concrete girders.

For either steel or concrete girder systems, once the panels are in place grout is poured into the shear pocket. The grout is required to fill the haunch and embed the shear connectors forming a composite pocket. Grout is used rather than concrete as it is highly fluid and only contains fine aggregate. This makes it highly suitable for filling the variable height haunch, which can be as narrow as 6 mm. A shear pocket system requires a large volume of grout, and careful site placement to avoid unwanted voids from forming in the haunch. Fig. 6 is a photograph taken from Issa et al. (1995) of a full-depth precast concrete deck that used shear pockets to accomplish composite action with the girder. It is evident from this picture that a number of issues need to be addressed when using full-depth panels so that strength and durability are not compromised.



Fig. 6. Full-depth precast concrete deck without wearing surface (from Issa et al., 1995)

As full-depth deck panels are typically prestressed in a lone-line bed, as discussed in Section 2.2.1.1, strands are spaced uniformly across the panel. However, after the panel has cured, strands have to be gas cut out of block-outs to allow sufficient room for shear connectors in the composite pockets. As a result, the strength of the panels is reduced at girders, where high negative moment exists. Negative moment due to traffic loads also makes the pockets prone to cracking, which affects the durability of the system. It is for this reason, as well as driver comfort, that a wearing surface is applied in most cases. This can be an asphalt, latex modified concrete, or micro-silica modified concrete (Hieber et al., 2005).

2.2.2.1.2 Tie down connections

Tie down connections can only be used for steel girder bridges. A mechanical connector is bolted into the full-depth panel soffit and hooked under the girder top flange. This requires a steel plate with nut to be accurately cast into the full-depth panel. As illustrated in Fig. 5(b) a block-out is not required, allowing for uniform steel placement across the panel. It was found by Issa et al. (2003) that some level of composite action was developed through interface friction. However, this level of composite action is insufficient over time as the connections loosen with traffic vibrations. The connections have also been found to fracture from fatigue thus are not a recommended option (Kropp et al., 1975).

2.2.2.1.3 Bolted connections

For steel girders, it is possible to avoid having a composite pocket through the use of bolted connections. Bolts are secured to the deck through ducts and bolted to the girder top flange. Drilling of holes in the flange reduces the moment capacity of the girder, thereby reducing the stiffness and strength and requiring a thicker plate to be used. Composite action is achieved provided a solid grout haunch exists between the top flange and panel soffit (Biswas, 1986). Once bolts are pretensioned the deck concrete is prone to cracking, reducing the stiffness, thus degree of composite action, making this system unpopular for use (Yamane et al., 1998).

2.2.2.2 Panel-to-panel seam for full-depth precast panels

In contrast to bridge deck construction using SIP panels, there is not a second stage on-site reinforced concrete pour for full-depth panels. This requires a new means to achieve continuity at the transverse panel-to-panel seam that exists. Transverse panels edges are finished with shear keys to provide continuity so a loaded panel can distribute impact load to the adjacent panel. Shear keys are typically either non-grouted male-to-female connections, Fig. 7(a), or grouted female-to-female connections as shown in Fig. 7(b). The connections must be designed to have adequate shear strength and negative moment capacity and also prevent leakage through the deck. Male-to-female connections are less common as these requirements are difficult to satisfy, requiring a high level of construction precision (Kropp et al., 1975). It has also been noted in projects that spalling of concrete occurred after bridges had been in service for a short time (Badie et al., 2006). It is for this reason that female-to-female grouted connections are primarily used at transverse joints of full-depth precast panels.

Female-to-female joints provide inclined surfaces at the shear key to enhance shear strength. A full gap exists between the panels to allow for irregularities at the shear face of the panel and to increase the bearing area (Issa et al., 1995). The panel-to-panel gap at the deck soffit is typically 12.5 mm, and plugged with a polyethylene backer rod. A sufficient transverse panel-to-panel gap at the top of the deck allows visual inspection and easy pouring of the grout to fill the shear key. Grout used in shear keys has high flowability, while still possessing high strength and low shrinkage. It is recommended that the shear keys are sand blasted to enhance the bond (Nottingham, 1996).

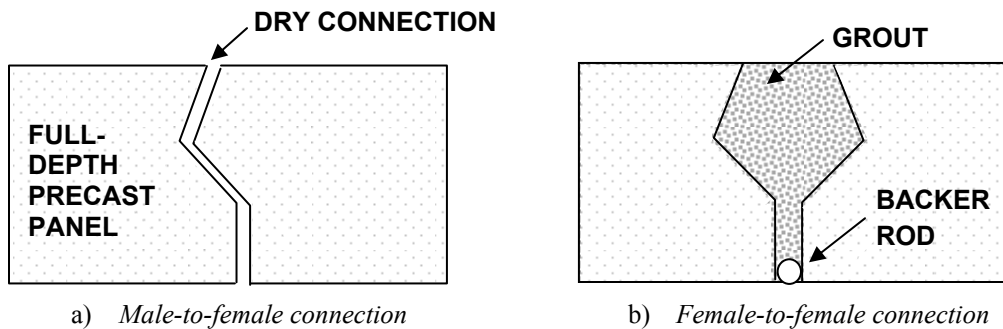


Fig. 7. Comparison of different transverse panel-to-panel shear keys

2.2.2.3 Leveling bolts and haunch forming

Coil inserts are cast in select locations of full-depth panels to house leveling bolts. These bolts are used to level the deck at each girder to achieve the correct grade. Once the bolt, and therefore deck, is at the correct height, the haunch is formed and grouted. In some cases steel shims are used for the haunch, or once the deck is leveled to the correct height foam backer rods are put in place (Badie et al., 2006). This requires access from under the bridge which reduces the efficiency of the system. Leveling bolts are removed once the grout has cured to reduce the likelihood of a stress concentration forming on the girder flange (Hieber et al., 2005). The removal of the bolt also eliminates durability concerns and reduces material costs as bolts can be reused on other panels that will be constructed.

2.2.3 Example of conventional construction in College Station, Texas

Recent changes in entrance and exit ramp locations for State Highway (SH) 6 in College Station, Texas, have resulted in the need of a new off ramp and bridge. The bridge spans over two lanes of traffic entering and exiting SH 6. As with 85% of other new concrete bridge decks in Texas, this deck is constructed using SIP panels seated on precast prestressed concrete girders. The deck consists of four girders spaced at 1.83 m with a 915 mm overhang either side resulting in a 9.14 m wide double lane bridge. Six simply supported spans are estimated to have a length of approximately 30 m, making the overall bridge length around 180 m. The construction of the bridge has been particularly

slow, with the deck alone taking some 5 months before completion. Photographs shown in Fig. 8 provide a fairly accurate description of task completion times for the new concrete bridge deck.

Fig. 8(a) shows the precast prestressed concrete girders in place spanning between piers. The placement of these girders took about one week, with road closures required for a short period of time for lifting the girders off shipping trucks. Once the girders were in place, the placement of SIP panels began, as shown in Fig. 8(b). Panels were first laid at an end abutment and progressed along the bridge length. At the same time steel brackets were attached to fascia girders at approximately 915 mm centers for the overhang formwork. Road closures at this time were common, thereby disrupting traffic and rerouting commuters, as crane access from the road below was required. Once the brackets were in place the plywood floor for the overhang was constructed, requiring a large amount of timber. Fig. 8(c) illustrates this, where the overhang is shown along with a temporary wooden safety railing. Note that the wooden forms required for the deck walls were not installed at the time the photograph of Fig. 8(c) was taken.

The construction of the overhang was ongoing for some 1.6 months, over which numerous traffic delays occurred. CIP deck concrete pours were cast in three segments, with the final pour finishing on April 9, 2009. Fig. 8(d) shows a completed deck pour that is covered with plastic to ensure adequate curing. After this time the guardrail was cast, taking around 3 weeks to complete. As of June 1, 2009 the overhang formwork was still in place. This generates motivation towards the use of a full-depth overhang system in Texas, thereby reducing the time of bridge deck construction. Section 2.3 provides the details of the state-of-the-art system proposed by TxDOT to achieve this.



a) *Placement of precast prestressed concrete girders: Jan 15-Jan 22, 2009*



b) *Placement of extruded foam and SIP panels: Jan 22- Mar 1, 2009*

Fig. 8. Construction of Rock Prairie exit bridge in College Station, TX, US - 2009



c) *Overhang formwork attached (without deck walls): Feb 1-Mar 20, 2009*



d) *One day after final bridge deck pour: Apr 10, 2009*

Fig. 8. *(Continued)*

2.3 State-of-the-Art

From the study of the current state-of-the-practice, it is evident that full-depth precast panels have considerable merit in concrete bridge deck construction. However, they have only been adopted for field application on a few occasions when prestressed precast concrete girders are used. Their lack of widespread use is considered to be due to the difficulty in accommodating the variable grade that inevitably occurs amongst the several precast prestressed concrete girders within a given span. Also, insufficient work has been done on providing a design basis for determining a reliable shear connection between the full-depth panels and precast prestressed concrete girder. It is for this reason that the well proven partial-depth SIP panel system is commonly used in the construction of bridge decks. However, one of the main difficulties with the current SIP panel system is forming the deck overhang to cast a full 200 mm thick overhang deck section. The Texas Department of Transportation (TxDOT) recently proposed a precast, prestressed full-depth overhang bridge system that potentially reduces the cost of construction and improves safety, and the speed of construction of bridges. Full-depth precast panels are used on the overhang while SIP panel are used at interior bays.

2.3.1 Full-depth overhang panel design

The objective of the full-depth panel design by TxDOT was to eliminate the need for external formwork while not drastically changing the current design and construction of concrete bridge decks. This reduces the likelihood of increased precast and on-site costs as well as errors from contractors having to use a completely new bridge deck system. It is for this reason that conventional SIP panels are used on the interior span along with a full-depth overhang panel that spans to the first interior girder. Shear connections are achieved between the full-depth overhang panels and concrete girders using a composite pocket. Subsections that follow provide more details on the design for precast construction as well as an overview of the system.

2.3.2 Precast construction of full-depth panels

Full-depth overhang panels are constructed and cast in two stages. The first stage, Stage I, is constructed in the same long-line prestressing bed as SIP panels. This eliminates the need for special forms and permits the use of the same prestressing at the first interior bay as the remainder of interior spans that use SIP panels. Panels are prestressed using 9.5 mm diameter Grade 270 seven-wire strand. The tendons are spaced at 150 mm centers and stressed to 70% of ultimate tensile strength. Standard strand extensions, as discussed in Section 2.2.1.1 of this thesis, of 75 mm are used. A welded wire mesh providing $465 \text{ mm}^2/\text{m}$ of reinforcement is placed perpendicular to the prestressing to provide temperature and shrinkage reinforcement. The panels are designed for a 915 mm overhang with a variable overall length depending on the girder spacing of the bridge. A common girder spacing of 1.83 m was used in this thesis. The completed Stage I pour is shown in Fig. 9(a). Standard U-bar lifting hooks and coil inserts for the leveling bolts are cast into the Stage I pour. As the strands are spaced at a standard 150 mm, notched timber block-outs, 250 mm x 180 mm in the longitudinal axis of the bridge are used for the composite pockets.

Tendons are released a day after the completion of the Stage I pour. This reduces the likelihood of differential creep and elastic shortening between the Stage I and Stage II pours. The top surface of the Stage I concrete is also roughened, as done with SIP panels, to enhance the bond between the two layers. Steel formwork, as illustrated in Fig. 9(b), is used for the Stage II reinforced concrete pour. The forms are notched so that the mild steel reinforcing can pass through it, as shown in Fig. 9(c). This allows for lap splices for the steel that is placed in the CIP deck pour. The transverse steel is #5 (15.9 mm) at a nominal spacing of 150 mm and spaced wider around composite pockets. The top longitudinal steel consists of #4 (12.5 mm) bars at 150 mm centers. Standard hooks are on the ends of the bars to allow for a panel-to-panel connection. Complete details of reinforcing layouts are given in Appendix 1. Once the timber block-outs are removed, the tendons are gas cut out to not interfere with the placement of shear connectors. A completed panel being lifted into place is shown in Fig. 9(d).



a) *Stage I prestressed concrete pour*



b) *Steel forms for Stage II reinforced concrete pour*

Fig. 9. Precast construction and on-site placement of full-depth overhang panels



c) *Plan view of completed full-depth overhang panel*



d) *Placement of full-depth overhang panel on concrete girders*

Fig. 9. (Continued)

2.3.3 Overview of full-depth overhang panel design

Fig. 10 shows two full-depth overhang panels placed adjacent to one another, **1**, and other key components of the system. Neither formwork nor falsework at the location of the exterior girder is required on-site. The overhang panels are cast off-site in two stages, as described in Section 2.3.2 of this thesis. One of the challenges of such a system is achieving a deck-to-girder interface shear connection, **2**. For this purpose, each 2.4 m wide precast panel includes three composite pockets, which measure 250 mm wide by 180 mm long, **3**. These are equally spaced over the panel length and allow for a connection to be made with either threaded rods or bolts extending from the prestressed concrete girder or welded studs if a steel plate girder is used.

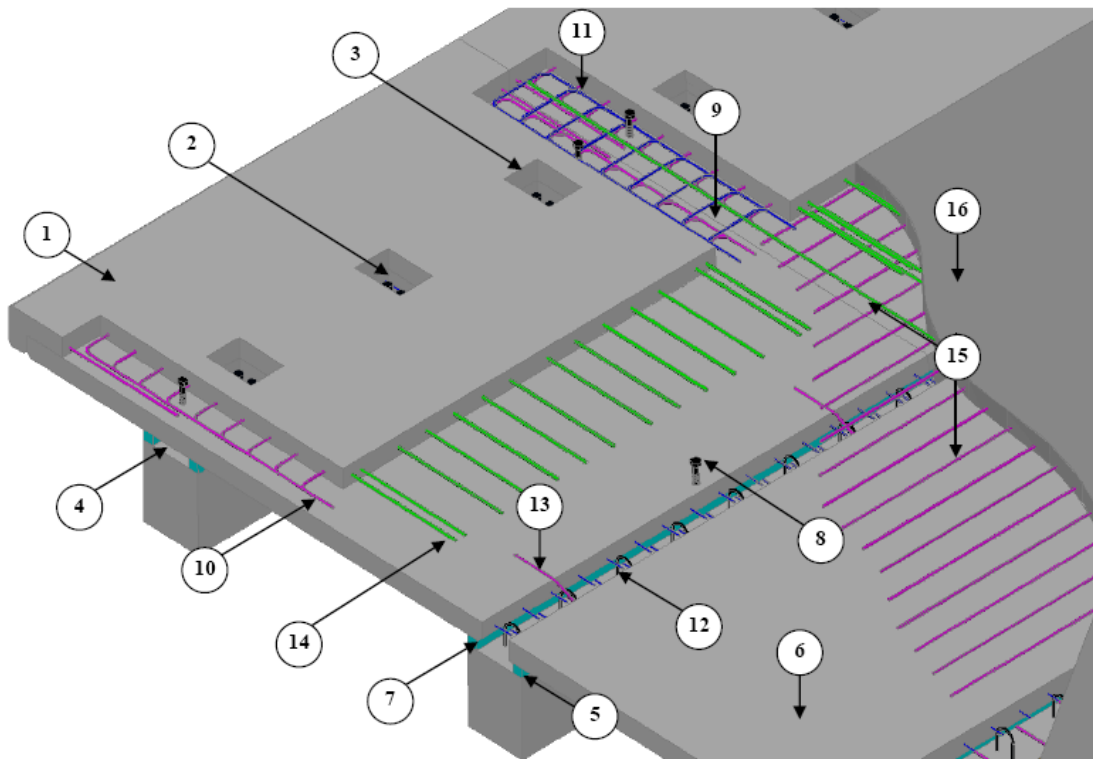


Fig. 10. Isometric view of two adjacent precast overhang panels (Mander et al., 2009)

A haunch, or gap, **4**, between the soffit of the precast panel and the girder occurs when grading of the bridge to the appropriate level is required. Typically the haunch height may range from 12 mm to 100 mm. This haunch variation accommodates the variable (unknown) camber in the prestressed girders, with the larger haunch heights typically near span ends. The haunch must be filled through the composite pockets requiring a free flowing grout material to be used. Due to the fluid nature of the grout, and potential high pressure head from the placing operation, the customary incompressible foam, **5**, used for the SIP panels, **6**, is no longer adequate. A low-density packing foam, **7**, is attached to the girder and deck with adhesive to prevent leakage of the grout from the haunch. But the use of such low-density foam requires leveling bolts, **8**, to adjust the grading of the deck and support the self-weight of the panel prior to placing the grout. Coil inserts are cast in the precast panels for housing of the leveling bolts, which can be raised or lowered using a wrench. Two leveling bolts on the exterior girder and one leveling bolt on the adjacent interior girder are used to adjust the panel height accordingly.

Another section of importance is the transverse seam, **9**, between adjacent precast panels. The panels are reduced to 100 mm thickness along the transverse edges of the panel, with the exception of a full-depth 200 mm thickness that extends 300 mm from the overhang end of the panels. This permits concrete to be placed into the transverse seam without requiring formwork on the overhang. Hooked steel from the top layer of reinforcement, **10**, extends from the precast panels to the transverse seam, where a C-shaped steel reinforcing bar, **11**, is tied to the extending bars. The transverse seam is filled with concrete when the interior deck is cast. In other areas of the bridge (not including the overhangs), conventional methods of placing and grading the deck, as well as R-bar shear connections, **12**, are used.

For safety, to prevent overturning of the overhang panels, two reinforcing bars (Z-bars), **13**, extending above the surface of the precast panel are welded to the interior girder R-bars. The top transverse layer of reinforcing steel, **14**, extends from the full-depth precast panels into the interior partial-depth panels to provide adequate lap-splices

of steel for load transfer between exterior and interior overhangs. Longitudinal and transverse steel is then placed on the remainder of the deck at a designated spacing, **15**. A final 100 mm concrete placement, **16**, ties the system together, after which the haunch and grout pockets are poured. A thin wearing surface can be placed on the exterior bay, concealing the pockets, in the shoulder area of the bridge. Key construction and design issues for the full-depth overhang panel system are discussed in the next section of this chapter.

2.3.4 Key construction and design issues

Relevant constructability and design issues that were discussed for SIP panels and full-depth panels in Section 2.2 of this thesis are addressed for the full-depth precast overhang panels developed for this research. Namely, shear connections, panel-to-panel connections, leveling and haunch forming, and over-turning of panels is addressed.

2.3.4.1 Shear connection

Rectangular block-outs measuring 250 mm wide (transverse to the bridge deck) by 180 mm long are spaced at 810 mm intervals over the girder. This allows for discrete shear connections to be made between the girder and full-depth overhang panel. The full-depth overhang panels in this work were designed to be used on precast prestressed concrete girders. As shown in Fig. 11(a), the conventional shear connection using reinforcing stirrup R-bars extending above the girder top flange is used for interior spans. Shear connections at the fascia girder for the full-depth overhang panels were explored by Henley (2009) under the same TxDOT contract (61008) as the research in this thesis.

After conducting shear push-off tests on a number of connections, the recommended connection from Henley (2009) was two high-strength steel threaded rod connectors with nuts on either end. As shown in Fig. 11(b) the threaded rods are cast into the precast prestressed concrete girder. Couplers can be used so that the girder top flange is finished flush and the threaded rods are installed on-site.

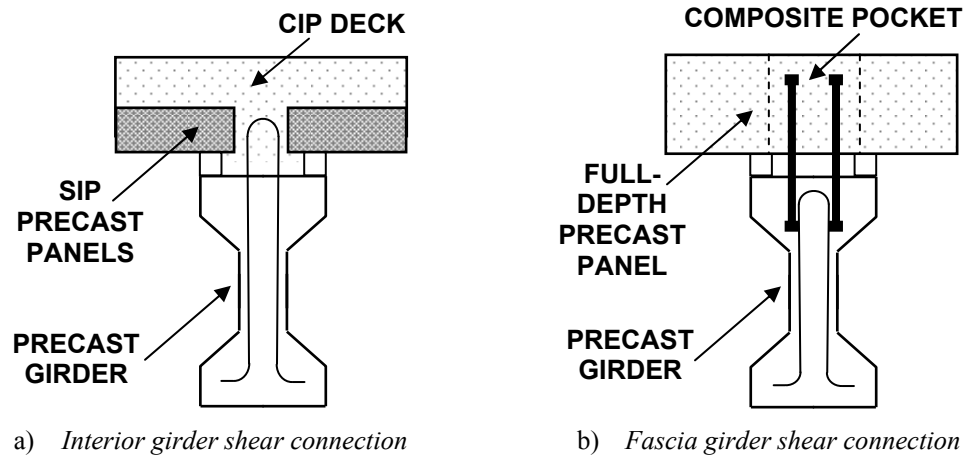


Fig. 11. Shear connections used for full-depth overhang panel bridge deck

A key finding in the work by Henley (2009) was that the force capacity provided by the steel R-bars must exceed the tensile capacity of the shear connectors. The stirrups that contribute to the capacity are found to over a width that is twice embedded depth of the shear connector into the girder. Thus a large number of R-bars are required in areas of high shear demand in the bridge deck where large diameter threaded rods are used. To prevent noticeable deck cracks around composite pockets an overlay can be applied to the overhang. A thin 50 mm overlay of asphalt, latex modified concrete, or micro-silica modified concrete (Hieber et al., 2005) can be used for this purpose.

2.3.4.2 Panel-to-panel connection

As with SIP panel deck construction, continuity is achieved at interior transverse panel-to-panel seams through a reinforced concrete CIP deck pour. The full-depth overhang panels are designed so that the same design principal can be used at the overhang region. The full-depth panels utilize a partial-depth seam as shown in Fig. 12. The top longitudinal reinforcement of the Stage II precast overhang panel pour has standard bent hooks. C-shaped bent reinforcing bars are tied to these standard end hooks on adjacent panels to provide a panel-to-panel connection. The final CIP deck pour ties the system together, with continuity provided at all panel-to-panel seams.



Fig. 12. Full-depth overhang panel-to-panel seam

2.3.4.3 Leveling bolts and haunch forming

A challenge with SIP-CIP bridge decks is grading the deck correctly in both the transverse and longitudinal directions. As shown in Fig. 13, the exterior girders have only 25% of the final weight on them after placing SIP panels. As a result, the exterior girders deflect less than interior girder. Because of this differential deflection, challenges can occur during construction in obtaining the correct cover, deck grade, and deck thickness. Developing a full-depth, precast overhang system will result in near full short-term deflection of the fascia girders, thus improving constructability of the bridge deck system.

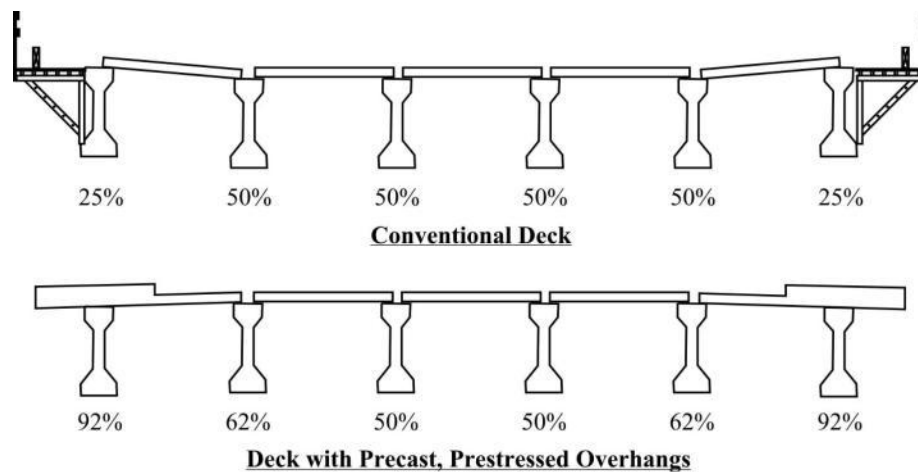


Fig. 13. Percentage of final deflections during construction (Merrill, 2002)

Longitudinal grading of a bridge deck with precast prestressed concrete girders is more complex than with steel girders due to the variable camber of the girder. The haunch, which is the space between the girder and the bridge deck soffit, has a large variation in height to ensure that the correct profile and bridge deck thickness is achieved. Thus it is necessary for the full-depth precast panels to have the ability to be easily adjustable to meet construction and grading tolerances. As discussed in Chapter II, Section 2.2.2.3 of this thesis, previous field implementation of full-depth panels required workers to form the haunch from beneath the deck after the panels were in place and graded to the correct height. The efficiency of forming the haunch is improved through the use of an alternative forming system.

An effective haunch system will be easily adjusted to the correct level with sufficient stiffness to resist the lateral pressures from a fluid grout. The full-depth precast overhang system developed for this work uses leveling bolts to grade the deck to the correct height. Three coil inserts, one for the seating at the interior girder and two at the fascia girder, are cast into the Stage I precast concrete pour to house the leveling bolts. The bolts are simply adjusted on-site with either a crescent or impact wrench. The haunch is formed with a low-density packing foam that is attached to the girder flange and panel soffit. The foam is attached with a two part plastic adhesive (3M Scotch-Grip

4693). As shown in Fig. 14, the foam compresses under the panel weight, requiring the leveling bolt to keep the panel at the correct grade. A variety of foams and adhesives were investigated by Trejo et al. (2008) and the capacity to lateral pressure, direct tension, and a combination of tension and lateral pressure determined experimentally. The maximum test lateral pressure and combined tension and lateral pressure was 6.5 psi. The foam was able to resist this pressure, making it suitable for pumping grout with a pressure head of 2 meters. The maximum elongation before the adhesive bond broke was 23 mm.



Fig. 14. Leveling bolt and haunch forming for full-depth precast overhang

The recommended construction method for haunch forming is as follows:

- The low-density foam should be cut approximately 25 mm taller than the desired haunch.
- Both the foam and precast concrete girder must be covered with adhesive separately. This is applied on one horizontal face of the foam (that will be in contact with the girder) and over a 50 mm wide strip on the top flange of the precast beam.
- Once the adhesive on the foam and beam have become “tacky” the foam should be placed on the girder surface and held in place for 2 minutes.
- The leveling bolts in the precast overhang panels should be adjusted so that they extend beyond the panel soffit 5 mm less than the height of the foam.
- Just prior to the placement of the precast overhang panels the top surface of the foam should be covered with 3M Scotch-Grip 4693 adhesive.
- The precast overhang panel should be placed and allow the adhesive to cure one day before grading the deck. After this time the panel can be lowered to the correct height. In no case should it be raised more than 5 mm from the placement position.

2.3.4.4 Grouting haunch

To provide a connection between the girder and full-depth overhang panel, the haunch must be grouted once it has been formed and correctly leveled. In the field, grouting will occur after the CIP portion of the deck has been cast so that the girders reach their final dead load deflection. A proprietary grout, SikaGrout™ 212, is recommended to fill the haunch. SikaGrout™ 212 is a non-shrink, cementitious grout that is recommended for structural applications and is versatile for high flow applications. It contains a special blend of shrinkage-reducing and plasticizing/water-reducing agents that compensate for shrinkage in both the plastic and hardened states.

A water-to-powder ratio (w/p) of 0.19 provides a highly fluid mixture that fills the haunch with ease. Shown in Fig. 15(a) a 500 rpm mechanical drill mixer was used with a circular paddle mixer. The consistency of the grout was characterized with a flow cone test, Fig. 15(b), modified from ASTM C230/C 230M-98, *Flow Table for Use in*

Tests of Hydraulic Cement as the use of a flow table is not practical in the field. Consistency is also measured through efflux time, ASTM C939-02, *Flow of Grout for Preplaced-Aggregate Concrete* as in Fig. 15(c). Recommended consistency values for a high-flowing SikaGrout™ 212 mix are provided in Table 1.

Table 1. Consistency values for SikaGrout™ 212

Test Method	Recommended Range
Flow Cone Test	215 to 280 mm
Efflux Cone Test	8 – 14 sec

Grout is poured or pumped into a single pocket and inspected at adjacent pockets to ensure that it has flowed through. Flow tests conducted on this mix are provided in Chapter III, Section 3.4 of this thesis. Grout is poured to approximately 50 mm above the deck soffit in each composite pocket to ensure the haunch is completely filled. Once the grout has reached initial set, the same concrete that is used for the CIP deck is poured into each pocket. The procedure outlined in Trejo et al. (2008) for placing the haunch grout is provided in Table 2.



(a) Mixing of grout



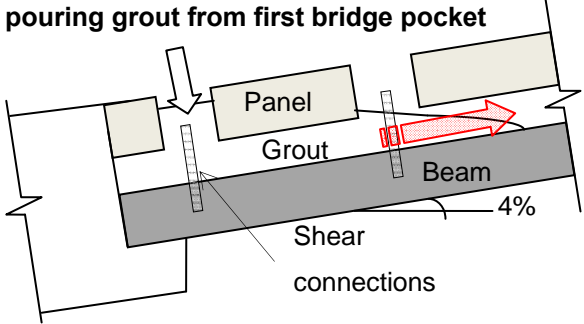
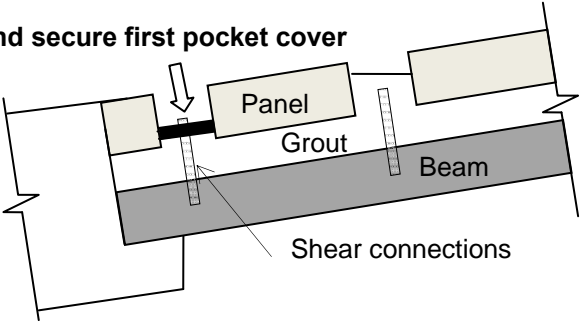
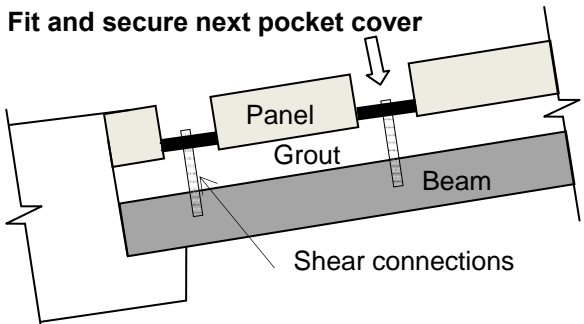
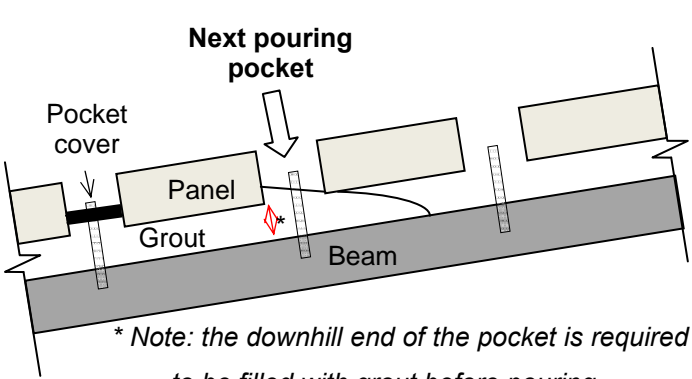
(b) Flow cone test



(c) Efflux Cone Test

Fig. 15. Test apparatus for grout mixtures

Table 2. Method for placing haunch grout for full-depth overhang panels (adapted from Trejo et al., 2008)

<p>Step 1: Begin placing from the lowest pocket and continue filling until the pocket is full.</p>	<p>Begin pouring grout from first bridge pocket</p> 
<p>Step 2: Use a pocket cover to force grout down until the grout is at the correct level. The pocket cover will need to be built to prevent leakage of grout, as well as to have a method of securing it to the shear connectors.</p>	<p>Fit and secure first pocket cover</p> 
<p>Step 3: Continue working up the bridge by blocking off pockets that are full by using pocket covers.</p>	<p>Fit and secure next pocket cover</p> 
<p>Step 4: The last pocket that has a full haunch now becomes the next pocket to pour into in order to continue filling the haunch. This ensures that no grout is able to flow downhill, as this creates entrapped air under the panel.</p>	<p>Next pouring pocket</p>  <p><i>* Note: the downhill end of the pocket is required to be filled with grout before pouring</i></p>
<p>Step 5: Repeat steps 1 through 4 until the entire haunch has been filled.</p>	

2.3.4.5 Overturning of full-depth overhang panels

One of the safety concerns with the use of full-depth overhang panels is the possibility of overturning while workers stand on the overhang prior to the CIP deck pour. This is mitigated in the proposed design through casting two reinforcing “Z-bars” into the Stage I precast pour. As shown in Fig. 16, the Z-bar is bent and site welded onto a shear stirrup (R-bar) at the interior girder. The bars are sufficiently long to allow them to be horizontally bent, by hand or pry bar, on-site to the closest R-bar.

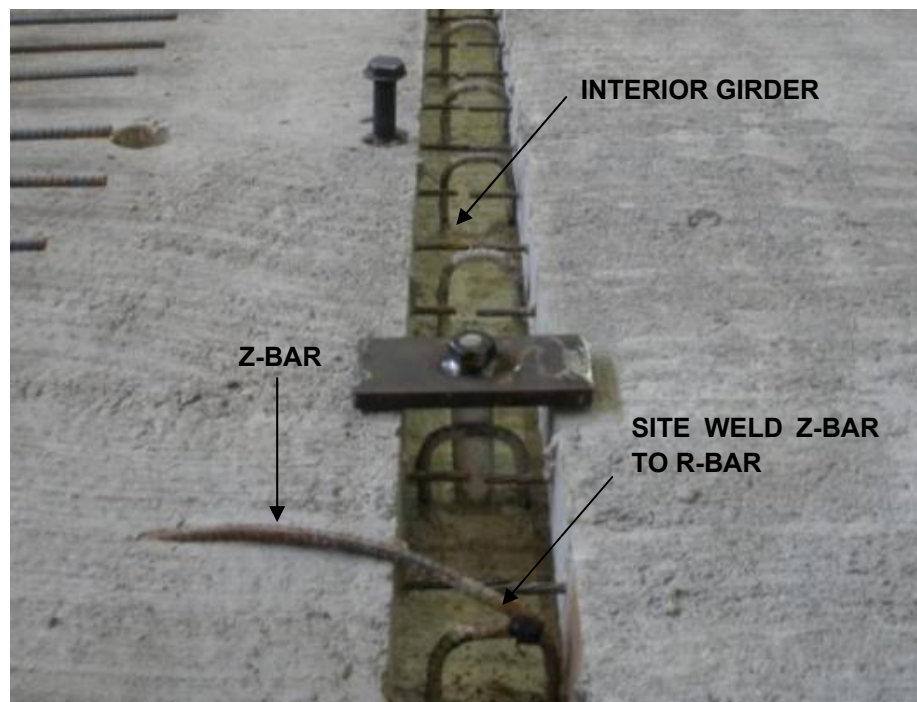


Fig. 16. Z-bars cast into Stage I to prevent overturning of full-depth overhang panels

2.3.5 Alternative construction: lab-cast panels

An alternative design to the full-depth precast prestressed concrete panels was proposed and constructed for this research. Using a SIP precast panel a second stage layer of concrete was cast on a portion of the panel along with a full-depth pour to create an overhang. This was done for three reasons; (1) to provide an alternative construction

solution to contractors, (2) to determine the effect that the continuous prestressing of the full-depth precast prestressed panels has on stiffness and strength and (3) to determine the effect the panel-to-panel seam has on the system behavior.

Unlike the conventional CIP overhang the concrete pour was done on a continuous flat surface. This eliminates the need for external formwork and only vertical walls are required, as shown in Fig. 17(a). Also seen in Fig. 17(a), are the composite pockets which begin at the edge of the SIP panels. These pockets are reduced to 150 mm squares, allowing for uniform spacing of reinforcement around the pocket. The same bottom reinforcement used in CIP overhang construction is implemented into the lab-cast design. Transverse #4 (12.5 mm) mild steel bars are spaced at 150 mm centers and welded onto the strand extensions of the SIP panels. This is done to provide positive moment capacity at the SIP panel to full-depth overhang seam for lifting purposes.

To achieve the objectives of determining the effects of continuous prestressing and the panel-to-panel seam on the system panel dimensions were kept the same as the full-depth precast prestressed overhang panels. Reinforcing details were also the same, with the exception of the bottom transverse reinforcing being mild steel instead of continuous prestressing. Also the bottom longitudinal steel replicated that of the conventional overhang, consisting of three #5 (16 mm) mild steel reinforcing bars. Fig. 17(c) shows the extension of the transverse bars beyond the top formwork to allow for a lap splice between the lab-cast overhang panel steel and transverse steel for the interior bay. Fig. 17(d) was taken following the placement of the concrete for the lab-cast panels. It can be seen in Fig. 17 and should be noted that only one transverse of the lab-cast panels were constructed with a partial depth seam for the panel-to-panel connection. As further discussed in Chapter IV, the experimental specimens consisted of two adjacent panels, only requiring one panel-to-panel seam to be formed.



a) *Side elevation showing 150 mm square block-outs*



b) *Bottom transverse steel welded to strand extensions*

Fig. 17. Lab-cast panel construction



c) *Transverse bars extending beyond notched forms for lap splices*



d) *Completed lab-cast panels following concrete pour*

Fig. 17. (Continued)

CHAPTER III

EXPERIMENTAL INVESTIGATION

3.1 Introduction

One of the main research objectives of this thesis was to experimentally evaluate the proposed of a bridge deck constructed with full-depth overhang precast panels. Single panels were not tested alone, as the panel-to-panel seam influences the system performance. Thus two full-scale, double-panel specimens, representative of Texas Department of Transportation (TxDOT) precast concrete bridge decks, were constructed. The rationale of the experimental design along with full-scale specimen details is firstly provided in this chapter. Following this, the experimental testing plan is discussed, with particular emphasis on locations of applied loads and instrumentation used to measure displacements and strains. Finally, a section is provided on an experimental grout track constructed to measure the flowability of the grout used in the fascia girder haunch through variable haunch heights at a 4% incline.

3.2 Experimental Design

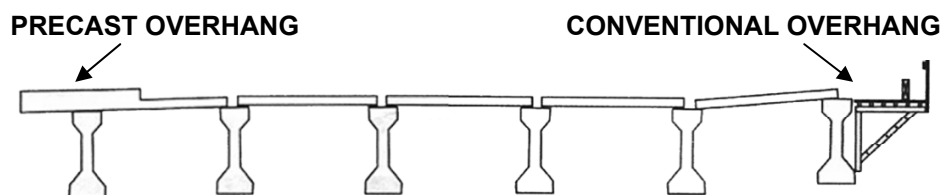
This section focuses on the basis of the experimental design for the double-panel specimens. Particular emphasis was placed on comparing performance of the proposed precast overhang to the conventional CIP overhang system. Material properties and dimensions for Specimen 1 and Specimen 2 are presented, along with the testing equipment used for loading the specimens.

3.2.1 Basis of design for double-panel specimens

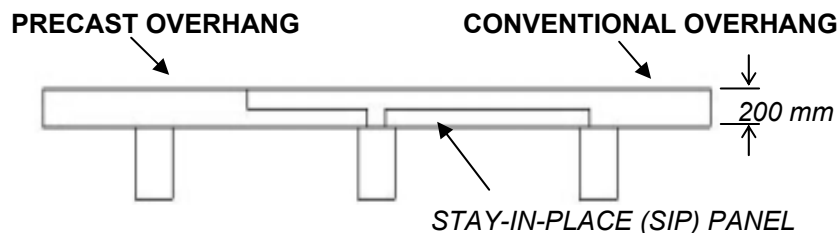
It is imperative to have experimental specimens that accurately represent bridge deck field conditions to characterize the behavior of the proposed full-depth precast overhang system. Fig. 18(a) presents a cross section of the prototype bridge system with the proposed precast, prestressed overhang on the left hand side of the bridge along with a standard conventional CIP overhang on the right hand side. Full-scale panels were constructed so that constructability issues could be addressed and ultimate strengths

could be characterized without involving scaling issues as the panels had not been previously tested. Thus a prototypical bridge deck that consists of several girders was narrowed for the experimental specimens to reduce construction costs. As shown in Fig. 18(b), the experimental setup consisted of three girders. This is suitable for testing as the proposed full-depth overhang system only influences the overhang and first interior bay.

Each of the two specimens had a footprint that measured 4.78 m along the longitudinal bridge axis and 5.49 m in the transverse direction. The setup consisted of two precast panels, 2.44 m long by 2.67 m wide, cast adjacent to one another and placed on reinforced concrete beams that were supported continuously on the laboratory floor. In this research, flexural bending of the deck was uncoupled from the deck panel-girder interface shear that exists in all bridge systems. This was achieved by seating the concrete beams that support the deck panels directly on the laboratory strong floor so they exhibit no longitudinal bending. Thus comparisons of failure modes and capacities of the new *deck overhang* system with the conventional CIP *overhang deck* system were simplified.



(a) *Prototype precast bridge deck construction showing precast overhang (left) and conventional overhang (right)*



(b) *Full-scale experimental set-up*

Fig. 18. Basis of experimental setup

The concrete beams were rectangular, 300 mm wide, representative of an AASHTO Type I girder top flange width. The beams were 400 mm deep, sufficient to place internal reinforcement and shear connectors while providing adequate space to place instrumentation on the deck soffit. Conventional precast panels spanned the central beam and an external beam for the conventional overhang system. Details of each of the two specimens, Specimen 1 and Specimen 2, are provided in the following sections.

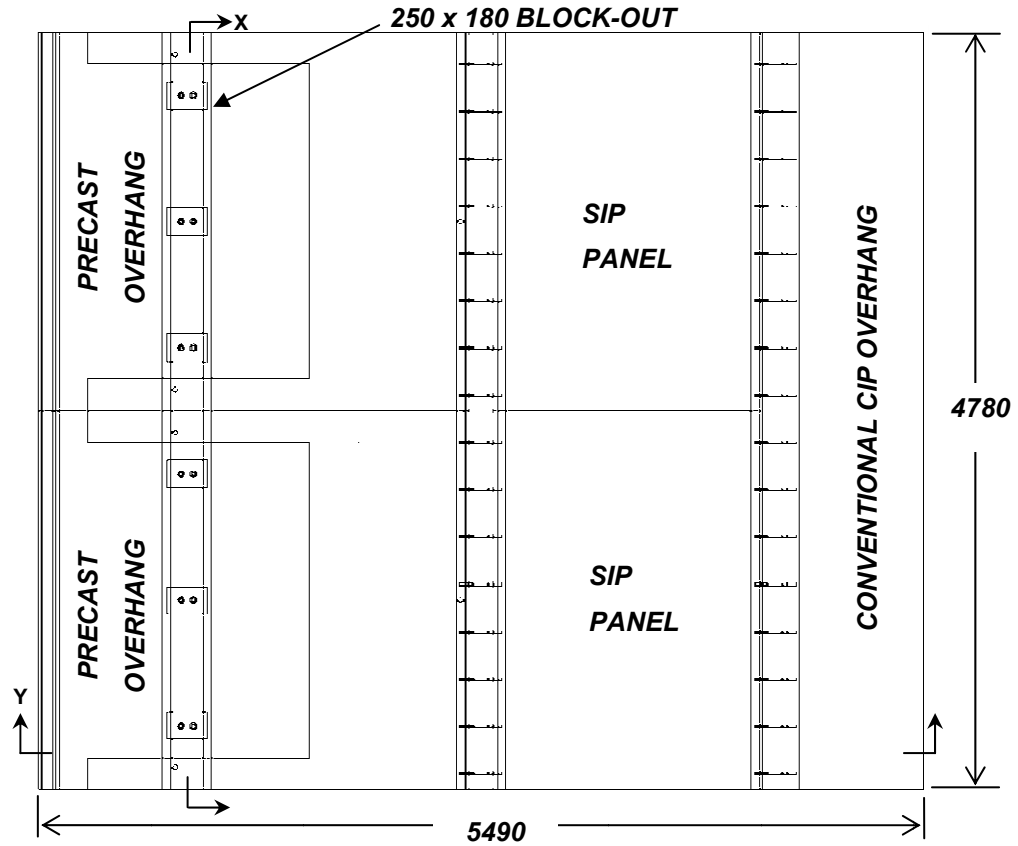
3.2.2 Details of Specimen 1

The first constructed specimen, Specimen 1, consisted of a conventional CIP overhang on one side and a double-panel full-depth precast overhang on the other overhang. Specimen 1 was designed to provide a comparison between the performance of the precast overhang and the conventional CIP overhang system. The full-depth overhang panels and SIP panels were constructed by Austin Prestressed Co. in Austin, Texas. SIP precast panels were used at the interior bay of the conventional overhang. The full-depth CIP overhang was formed in the High-Bay Structural and Materials Testing Laboratory (HBSMTL) at Texas A&M University. The layout and dimensions of Specimen 1 are provided in Fig. 19.

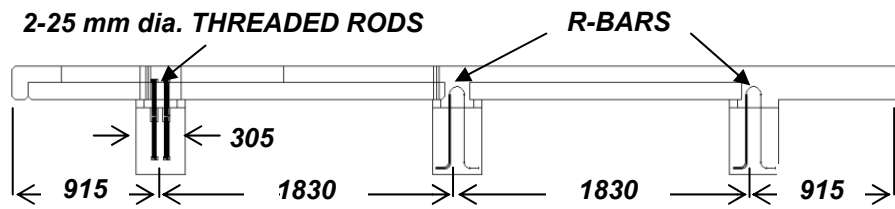
The main differences between the precast and conventional overhangs were the panel-to-panel seam between full-depth overhang panels and the bottom transverse reinforcement at the overhang. The CIP overhang was constructed to be continuous, with no lap-splices in the either transverse or longitudinal reinforcement. Conversely, adjacent full-depth panels had a standard partial depth seam which was made connected by C-shaped reinforcing bars tied to the top layer of longitudinal steel from the Stage II pour. Bottom reinforcing details differed in the overhangs. At the CIP overhang the bottom transverse steel was discontinuous due to the presence of the SIP panel bearing on the fascia girder. A layer of transverse #4 (12.5 mm) mild steel bars with 45 mm clear cover were spaced at 150 mm centers for the conventional overhang. Three #5 (16 mm) longitudinal bars were placed closest to the free edge over a width 500 mm. Full-depth overhang panels had continuous bottom prestress from the first interior girder to the

overhang in the full-depth precast panel. The bottom transverse reinforcing was a welded wire mesh providing 465 mm^2 of steel per meter.

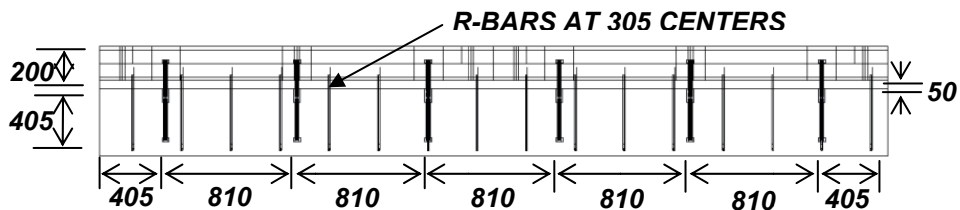
Composite action was provided between the girder and precast overhang panel through the grout in the haunch and threaded rod connectors at each pocket. A 50 mm tall haunch was used, filled with SikaGrout™ 212 having a water-to-powder (w/p) ratio of 0.19. With this grout the pockets were filled 50 mm above the deck soffit, to ensure adequate filling of the haunch. Once initial set was reached, the pockets were individually filled with SikaGrout™ 212 having a w/p = 0.16. Two 25 mm diameter high-strength B7 threaded rod connectors were embedded in each pocket. Threaded rods were cast 300 mm into the beam with a coupler cast flush to the beam top surface and a high-strength B5 nut on the other end. The threaded rods entering the composite pocket extended 200 mm above the top beam surface, and were attached to the embedded coupler with a crescent wrench. The conventional overhang and interior beam had the customary #4 (12.5 mm) R-bar stirrups at 300 mm centers extending above the beam surface by 130 mm.



PLAN VIEW



SECTION Y-Y: END ELEVATION



SECTION X-X: SIDE ELEVATION

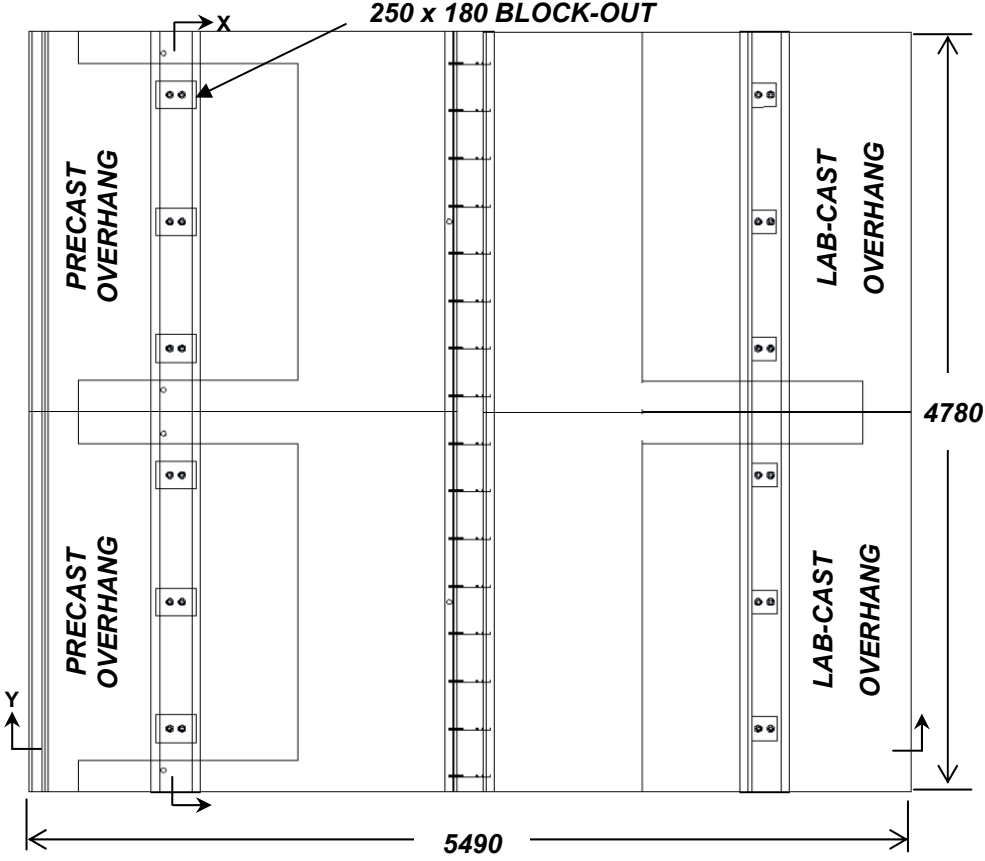
Fig. 19. Specimen 1 dimensions (mm)

3.2.3 Details of Specimen 2

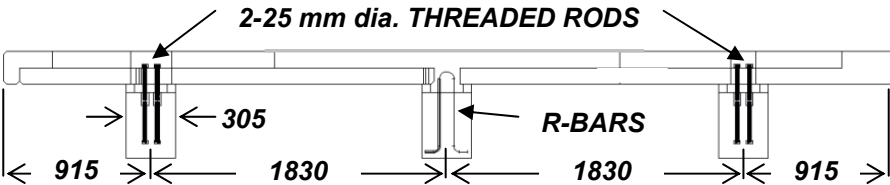
Specimen 2 was designed with the dual objective: (1) to confirm the findings of the precast overhang system tested on Specimen 1; and (2) to investigate an alternative approach for constructing full-depth overhang panels. The latter objective was achieved by constructing a conventional panel system, referred to as “lab-cast” panels herein. This consisted of a second stage concrete placement on top of a standard precast, prestressed SIP panel to achieve a full-depth overhang panel. The reinforcement details for this system were similar to the precast overhang system, with the exception that the bottom layer of prestressing strands were replaced with conventional reinforcement. As with the conventional overhang system, #4 (12.5 mm) deformed reinforcing bars were placed at 150 mm centers. These bars were welded onto the strand extensions from the SIP panels to provide positive moment capacity for lifting the panels. Complete detail is provided in Section 2.3.5 of this thesis.

The shear connections for this system were similar to the Specimen 1 connectors with the exception of the pockets, which were reduced from 250 x 175 mm to 150 mm square pockets. Smaller composite pockets allowed for the main top steel over the cantilever portion to be consistently spaced at the 150 mm uniform spacing. It was anticipated that by evaluating the lab-cast panels, information could be obtained on the effect of the prestress in the bottom layer. Moreover, as the reinforcement details were also the same as the conventional overhang, this enabled the effects of the transverse seam to be investigated.

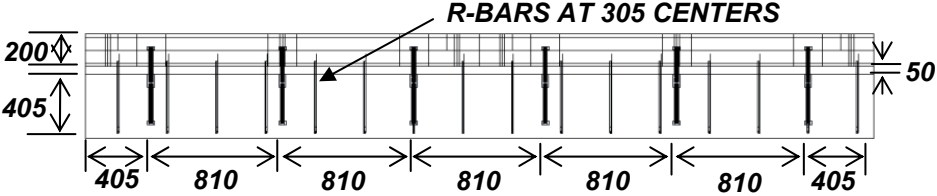
As in Specimen 1, a 50 mm haunch was used, filled with SikaGrout™ 212 having a water-to-powder (w/p) ratio of 0.19. Two 25 mm diameter high-strength B7 threaded rod connectors were embedded in each pocket in the same way as Specimen 1. Subsidence cracks were observed around the composite pockets of Specimen 1. For this reason, the same concrete used to construct the deck was used to fill up the remaining 150 mm height in the composite pockets. The interior beam had the customary #4 (12.5 mm) R-bar stirrups at 300 mm centers extending above the beam surface by 130 mm. The layout and dimensions of Specimen 1 are provided in Fig. 20.



PLAN VIEW



SECTION Y-Y: END ELEVATION



SECTION X-X: SIDE ELEVATION

Fig. 20. Specimen 2 dimensions (mm)

3.2.4 Material properties

All precast panels for the research program were fabricated at a precast plant, using the long-line pretensioning methods, while all other specimen components were constructed in the High Bay Structural and Materials Testing Laboratory (HBSMTL) at Texas A&M University. The precast panels and laboratory beams were constructed with TxDOT Class H concrete with a specified 28-day compressive strength of 34 MPa. A TxDOT Type S concrete, with a target strength of 28 MPa, was used for the deck. Both concrete types have a maximum water-to-cement ratio of 0.45 as per Texas Department of Transportation (2004). A slump of 100 mm was specified for all concrete mixtures. Cylinders were cast from each concrete batch in accordance with standard practice (see ASTM C192 Standard). Compression tests (according to ASTM C39) were conducted at 3, 7, and 28 days after casting and at the time of testing of the test specimens. Splitting tensile tests were also conducted on the day of testing in accordance with ASTM C496.

Table 1 shows the compressive strengths of the different concretes used in the research at 3, 7, and 28 days after casting, and also the measured compressive strength on the day of each experiment. Splitting tensile strengths at the time of specimen testing are also given in Table 3. Tensile tests were also conducted to characterize the mild steel used in the panels and CIP decks. Tensile tests were also conducted on the threaded rods that were used for shear connectors on the precast overhang. All steel met the 414 MPa yield requirements of ASTM A615, Standard Specification for Deformed and Plain Carbon-Steel Bars for Concrete Reinforcement. Fig. 21 plots the results from stress-strain curves with key values from the tension tests given in Table 4.

Specimens 1 and 2 had 50 mm high haunches filled with SikaGrout™ 212 having w/p ratio = 0.19. The strength of the haunch grout at the time of the experiments was recorded as 41.8 MPa and 40.2 MPa for Specimens 1 and 2, respectively. The pockets of Specimen 1 were filled with the same high performance grout except the w/p ratio was 0.16, with a compressive strength of 45 MPa at the time of the experiments. After less than 12 hours after the grout placement subsidence cracks were observed around the pocket perimeter of Specimen 1. As a result of this, TxDOT Class S concrete

was used in the pockets for Specimen 2. No visible cracks were observed when concrete was placed in the pockets in Specimen 2.

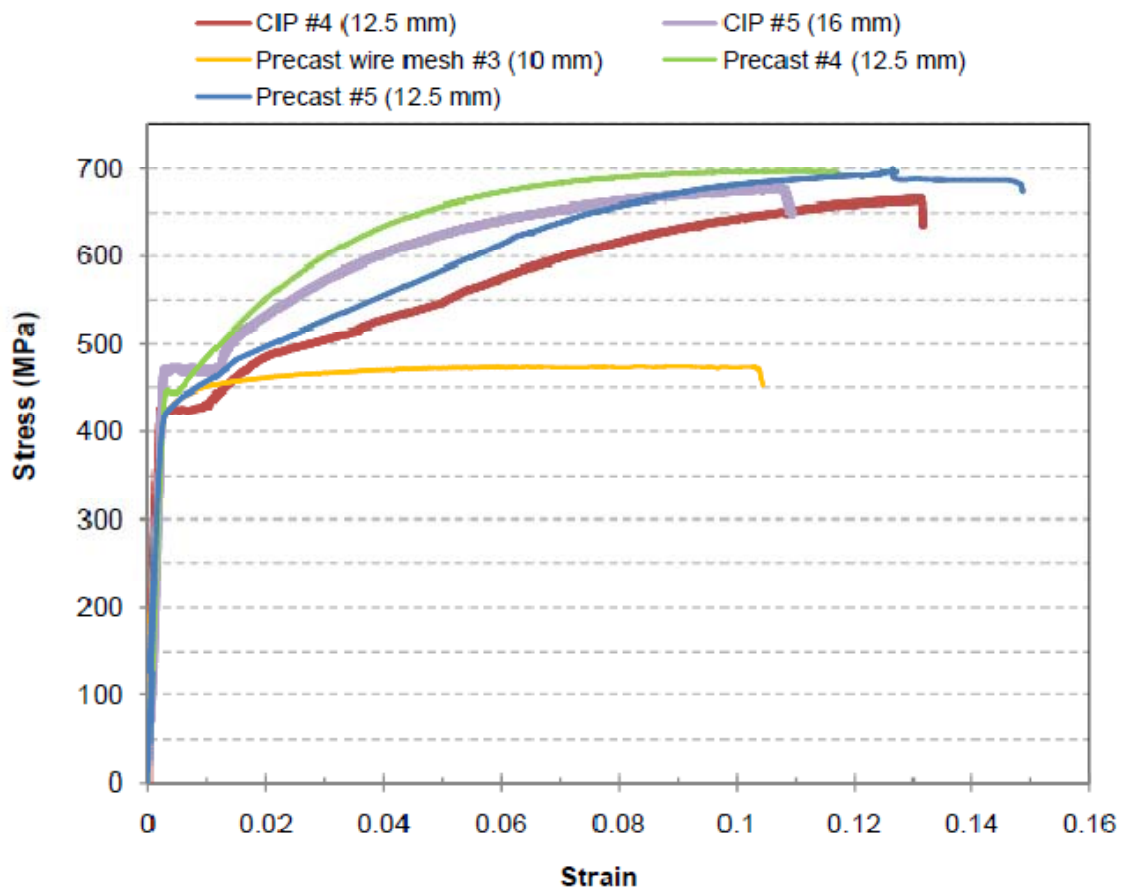
Table 3. Compressive and tensile strengths of cementitious materials

Specimen No.	Component	TxDOT Concrete Type	Cast Date	Compressive Strength, MPa				Tensile Strength MPa
				3-day	7-day	28-day	At Testing	At Testing
1	Stage I	H	2/5/08	29	41	55	58	6.0
1	Stage II	H	2/8/08	41	50	53	62	5.5
1	SIP Panel	H	2/12/08	30	45	53	62	6.1
1	Deck closure/CIP overhang	S	3/28/08	26	45	58	59	5.5
2	Stage I	H	1/31/08	37	47	60	66	5.6
2	Stage II	H	2/5/08	29	41	47	52	5.2
2	SIP Panel	H	2/11/08	34	45	48	52	6.0
2	Lab-cast overhang	H	4/14/08	32	45	55	58	4.7
2	Deck closure	S	5/19/08	20	24	33	31	3.2

Notes: Stage I is first stage pour of precast overhang panels; Stage II is second stage pour of precast overhang panels; SIP Panel = stay-in-place panel for interior bay.

Table 4. Stress-strain values for steel reinforcement

Specimen	Yield Stress MPa	Yield Strain	Strain at onset of strain-hardening
CIP #4 (12.5 mm)	434	0.00185	0.0095
CIP #5 (16 mm)	468	0.00241	0.0130
Precast wire mesh	434	0.00215	0.0025
Precast #4 (12.5 mm)	455	0.00250	0.0055
Precast #5 (16 mm)	434	0.00230	0.0025

**Fig. 21.** Steel stress-strain curves

Using the actual material properties and reinforcing layouts the moment capacities of the bridge deck sections were calculated per unit width. Ultimate moment capacities for the various deck sections are provided in Table 5. These values are used in the subsequent analysis. The sectional area of reinforcement per unit width is assumed to be constant across the slab, from which the moment capacity is calculated on a per meter basis. Note that the x -direction is taken as transverse to the direction of travel and the y -direction is the longitudinal direction of the bridge.

Table 5. Moment capacities (per unit width) for bridge deck sections using actual material properties

Section	M_x kNm/m	M_x' kNm/m	M_y kNm/m	M_y' kNm/m
Conventional/lab-cast overhang	32.3	85.6	72.5	56.4
Precast overhang	124.5	96.5	31.0	66.6
Interior (full depth)	106.97	100.26	53.02	58.85
Transverse seam	-	-	21.53	13.30
Interior stay-in-place (SIP) panel	26.95	29.85	8.41	13.79

3.2.5 Loading protocol

To characterize the stiffness and strength of Specimens 1 and 2 a 2670 kN capacity actuator was used to apply monotonic vertical loads that represented wheel loads from a truck. Fig. 22 shows the actuator top hung from the bottom flange of a steel header beam on a 75 mm thick steel plate that was attached to rollers. This versatility allowed ease in relocating the actuator to load at different longitudinal locations on the specimens. Detailed loading locations are provided in Section 3.3 of this thesis. The header beam was bolted to a steel reaction frame that was prestressed down to the 1.83 m thick concrete strong floor in the HBSMTL at Texas A&M using high strength tie-rods. Tie-down holes spaced at 915 mm centers throughout the HBSMTL allowed mobility of the frame in the transverse direction to test both overhangs and interior segments of Specimens 1 and 2. The flexibility of changing the loading position was an important aspect in the experimental design. As a result, the bridge deck did not require to be moved for any portion of the experiments, which may have caused undue surface cracks and a reduction in stiffness.

Magnitudes of the applied loads were measured via an in-series load cell with a 9000 kN capacity. The loads were applied via steel load plates, 75 mm thick, seated on a 12.5 mm thick neoprene pad (Shore 70, similar in hardness to a tire tread). A rectangular tire footprint measuring 250 mm long by 500 mm wide was used as per AASHTO LRFD (2007) Section 3.6.1.2.5. A W14x109 spreader beam was used to apply the load to two load plates when a tandem axle (wheel) load or axle loads were investigated.

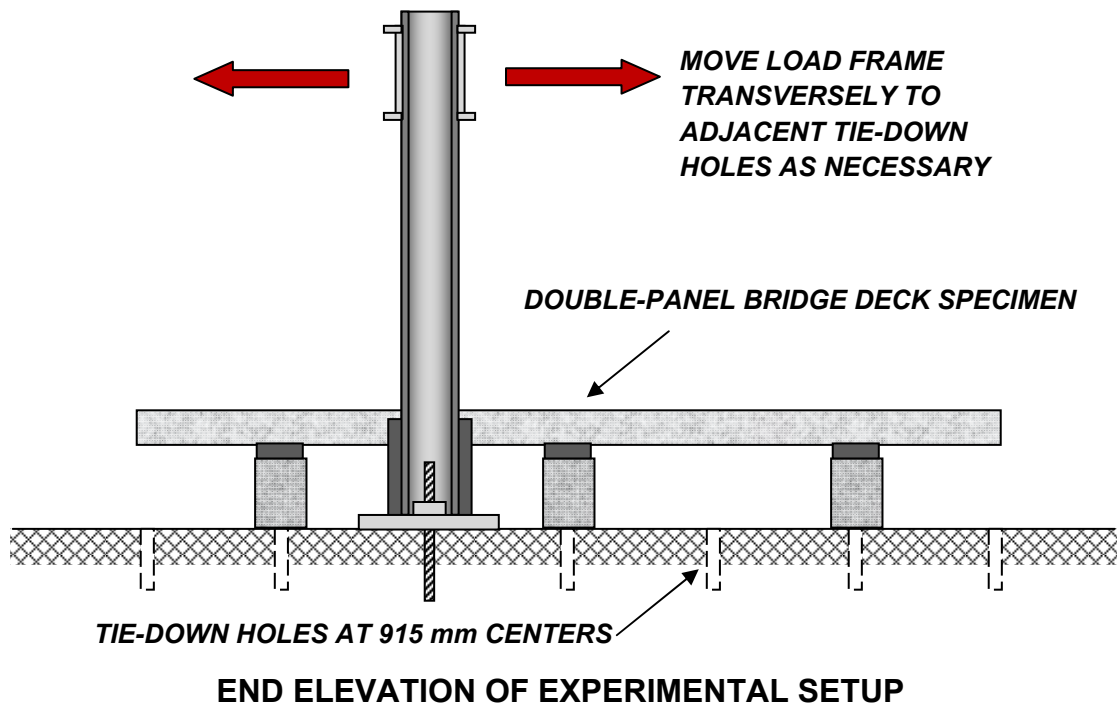
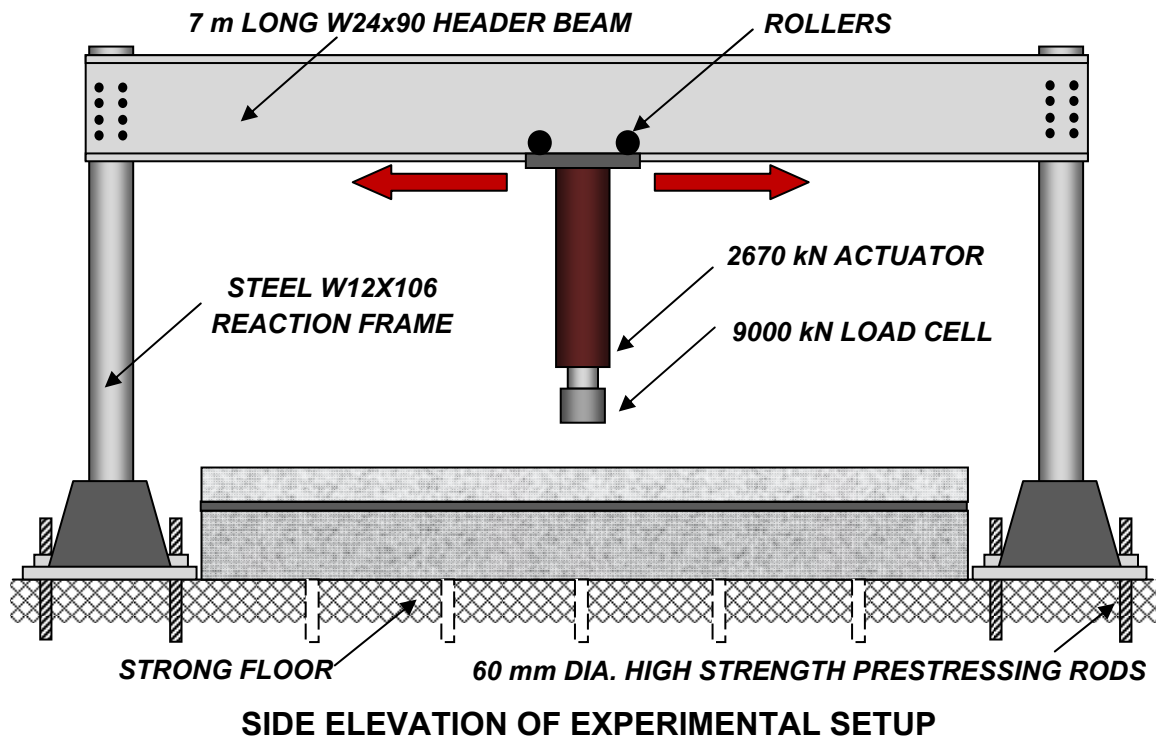


Fig. 22. Schematic of experimental testing equipment

3.3 Experimental Testing Plan

The experimental testing plan was designed to achieve two objectives; (1) to validate the strength required per AASHTO LRFD Bridge Design Specification (2007) loads, and (2) determine failure loads by loading at critical locations. Concrete is prone to cracking as it is weak in tension but strong in compression. Thus to map cracks efficiently and determine the stiffness of the bridge deck system accurately, the loading plan was important. For this reason, AASHTO factored loads were applied at two locations on either overhang, and only loaded to the maximum factored load. As a result the overhang was able to be loaded at a critical location. Single loads and tandem axle (wheel) loads per AASHTO LRFD (2007) were applied to chosen locations on the deck.

3.3.1 AASHTO LRFD loading

One of the main objectives of this research was to determine the behavior of the newly proposed full-depth precast prestressed overhang when loaded to AASHTO LRFD Bridge Design Specification (2007) loads. Fig. 23 presents the HL-93 Design Truck and HL-93 Design Tandem loads per axle along with prescribed wheel spacing as per Sections 3.6.1.2.2 and 3.6.1.2.3. The experimental specimens were loaded to the maximum factored loads based on the AASHTO LRFD (2007) load factors given in Table 6. As discussed in Section 3.2.5 of this thesis, this load is applied over a 500 mm wide by 250 mm long footprint.

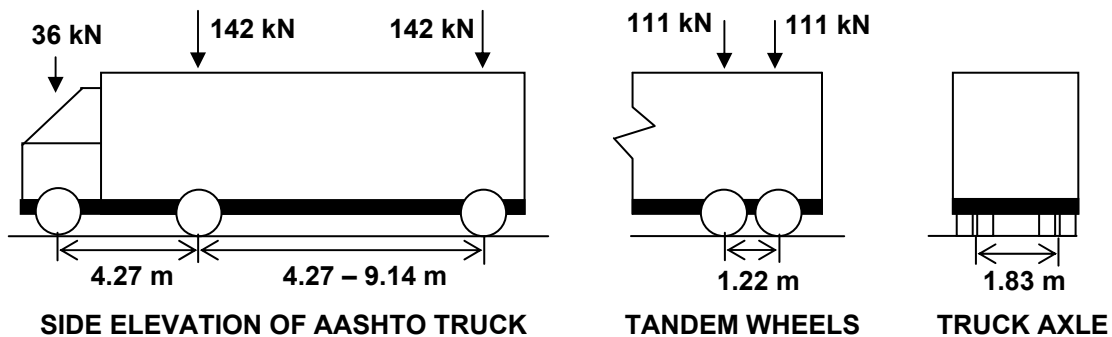


Fig. 23. HL-93 design truck and design tandem loads per axle

The most adverse load factors, based on AASHTO LRFD Bridge Design Specifications (2007) values, were used. A multiple presence factor of 1.2 is used assuming one loaded lane given by Table 3.6.1.1.2-1 in AASHTO LRFD (2007). A live load factor of 1.75 was used for all load cases based on the limit state of Strength I per Table 3.4.1-1 of AASHTO LRFD (2007). The dynamic allowance factor (*IM*) varied depending on the location of the load plate as in Table 3.6.2.1-1 of AASHTO LRFD (2007). An *IM* of 1.75 was used as some of the experiments were loaded at the transverse panel-to-panel seam. On the conventional overhang and when loading midway on a precast panel, an *IM* of 1.33 was used.

Table 6. AASHTO LRFD (2007) load factors and maximum factored loads

Location	Wheel load (kN)	Multiple Presence Factor	Live Load Factor	Dynamic Allowance Factor	Maximum Factored Load (kN)
Truck wheel	71	1.2	1.75	1.33	200
				1.75 for joints	267
Tandem wheel	55	1.2	1.75	1.33	155
				1.75 for joints	200
AASHTO LRFD Specification (2007)	3.6.1.2.2 and 3.6.1.2.3	3.6.1.1.2	3.4.1 (Strength I)	3.6.2.1	(Strength I)

At the overhang the factored load was applied per Section 3.6.1.3 of the AASHTO LRFD Bridge Design Specifications (2007). This states that the center of the load plate should be applied 305 mm from the inside face of the guard rail. It was assumed that the guard rail would be 305 mm wide at the base, as this is the width of the full-depth seam between panels. As shown in Fig. 24, this positioned the center of the load plate 150 mm from the beam face, resulting in 50 mm of the load plate bearing over

the haunch. As a result the experimental displacements are expected to be small, as the beams are seated on the concrete strong floor preventing any longitudinal bending. For typical bridge spans ranging from 27 to 43 m, Type V or Type VI AASHTO girders are used. Both have a top flange width of 1.07 m, thus under Section 3.6.1.3 of AASHTO LRFD the entire load plate would be bearing directly over the top flange. Thus it can be inferred that in field conditions the girder stiffness would primarily govern the vertical deflection of the bridge deck.

On each overhang, two AASHTO LRFD load cases were applied for loads increasing up to 260 kN. As illustrated in Fig. 25, the first load was on the panel-to-panel seam (or longitudinal mid-point for the conventional overhang) and the other at the longitudinal mid-point of a precast panel (or quarter-point for conventional overhang). The loads are referred to as Load Cases 1.1, 1.2, 1.4, 1.5, 2.1, 2.2, 2.5 and 2.6. The first integer denotes which specimen (Specimen 1 or 2) the experiment was performed on, and the second the order in which they were conducted.

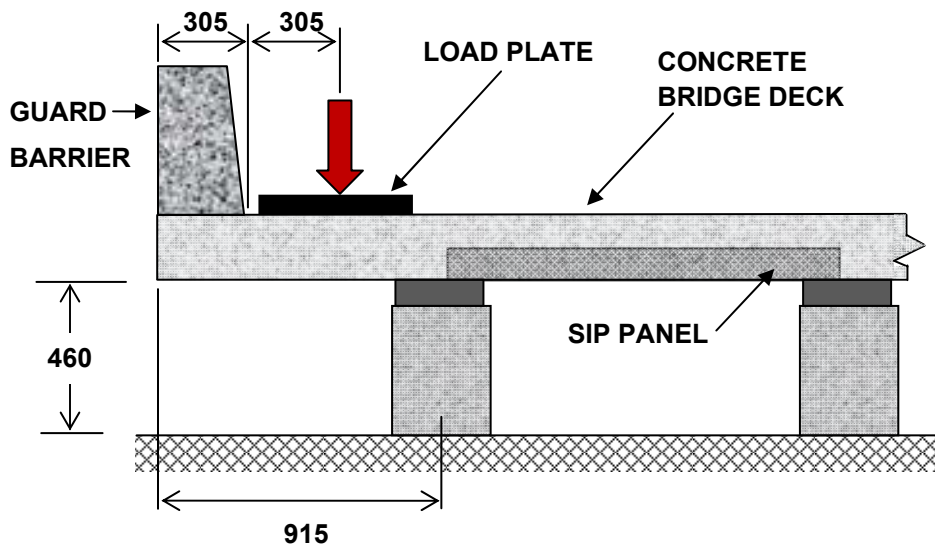


Fig. 24. AASHTO LRFD (2007) overhang loading position (dimensions in mm)

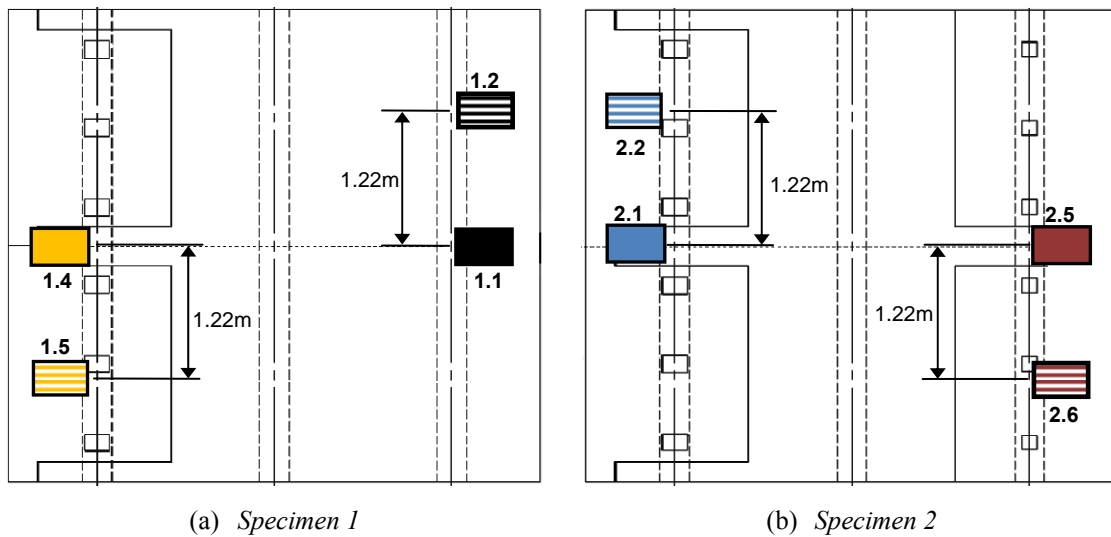


Fig. 25. Load plate positions for AASHTO LRFD (2007) overhang loads

3.3.2 Overhang failure load

It is important to characterize the failure load and failure mechanism of the overhangs to determine their ultimate carrying capacity. Fig. 26 illustrates the critical overhang failure load with the load plate on the edge of the overhang. This may be representative of a crash load, with an increased moment due to the overturning force from the barrier resistance. The shear force is the same as the AASHTO LRFD (2007) required load; however, a greater moment at the beam face makes it critical. Only one critical load was applied per overhang due to expected plastic and irreversible damage to the panels when loading to the ultimate load. As shown in Fig. 27, Load Case 1.3 was applied at the longitudinal mid-point for the conventional CIP overhang. Load Case 1.6, on the precast prestressed full-depth overhang, was loaded at the edge of the transverse panel-to-panel seam. This tested the direct strength of the seam and the ability of a loaded panel to distribute load to an adjacent panel. Load Case 2.7 was also applied at the edge of the transverse panel-to-panel seam on the lab-cast panel overhang. A tandem axle (wheel) load was used for Load Case 2.3 on the full-depth precast prestressed overhang. The first wheel load was applied at the transverse panel-to-panel seam with the tandem axle

(wheel) spaced 1.22 m apart as per AASHTO LRFD Bridge Design Specifications (2007).

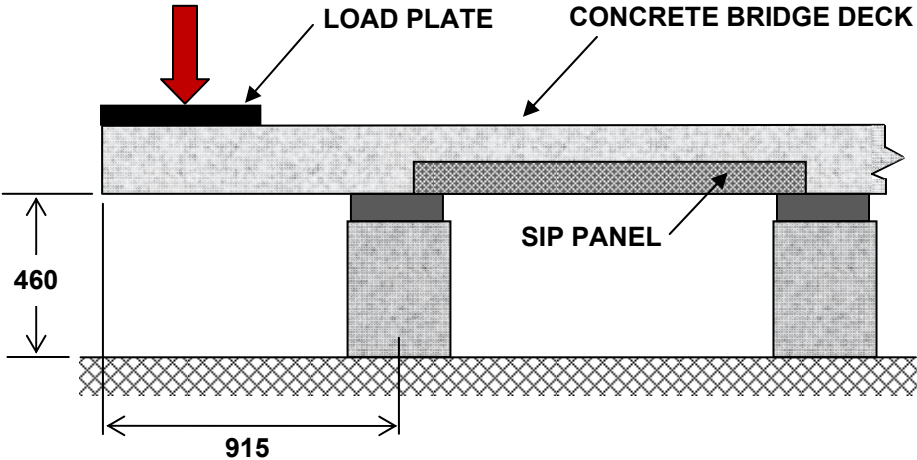
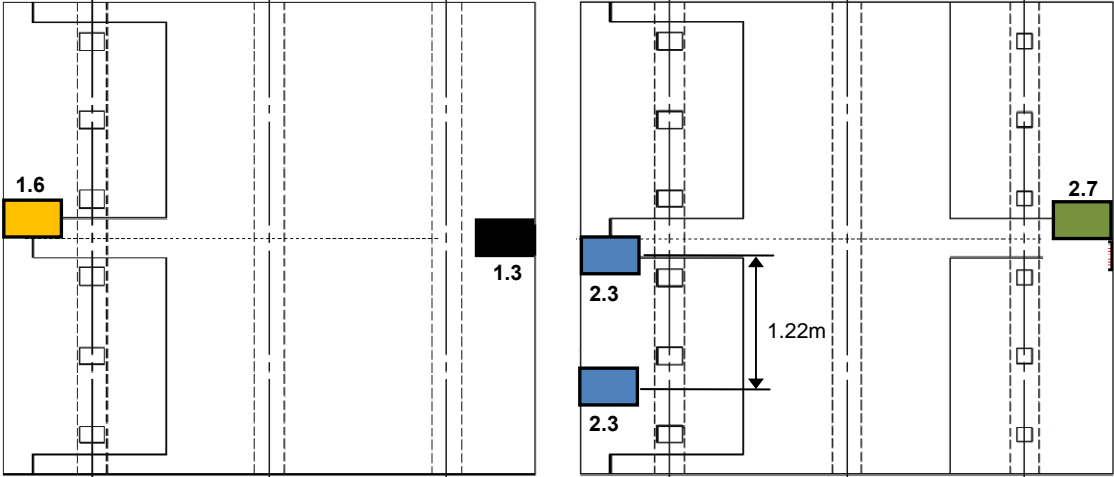


Fig. 26. Overhang failure loads (dimensions in mm)



(a) Specimen 1 (b) Specimen 2

Fig. 27. Load plate positions for overhang failure loads

3.3.3 Interior loads

Although overhang analysis cases allow direct comparison between the conventional overhang and precast overhangs, it is instructive to determine if the construction methods influence the first interior bay. For this reason the interior bays of Specimen 1 and Specimen 2 were loaded to failure. The stiffness of a precast prestressed overhang panel and conventional SIP panel were characterized in Load Case 1.7. As illustrated in Fig. 28(a), an axle load with standard wheel spacing of 1.83 m was applied to the mid-point of each panel. Load Case 2.8 was similar, but the axle load applied at the edge of the panel-to-panel seam and loaded to failure.

Loading for Specimen 2 is shown in Fig. 28(b). Load Case 2.4 was a tandem axle (wheel) load on the interior panel of the precast prestressed overhang side. Both wheel loads were on a single panel with the leading wheel on the edge of the panel-to-panel seam. Load Case 2.8 was similar but loaded on the lab-cast side; one wheel load was on the adjacent panel, at the edge of the seam of Specimen 2. Wheel loads represented tandem axles spaced at 1.22 m, whereas in Specimen 1, Load Cases 1.7 and 1.8 represented a total axle load with the two wheel loads spaced 1.83 m apart.

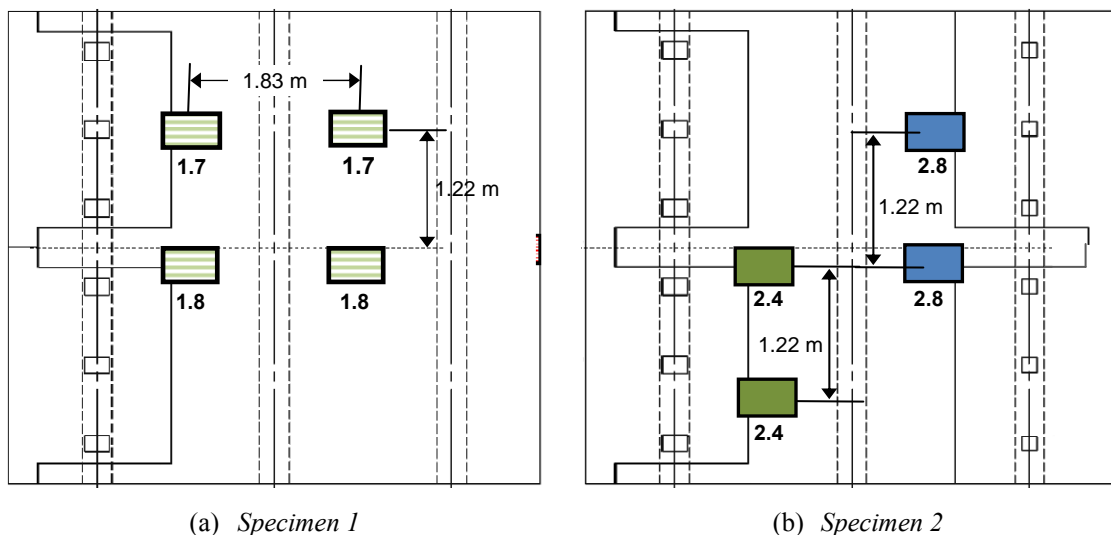


Fig. 28. Load plate positions for interior bays

3.3.4 Instrumentation

An adequate instrumentation plan was important to ensure sufficient data was obtained to assess the performance of the specimens. Loads were measured with a load cell, and displacements and strains were monitored and recorded with an electronic data acquisition system programmed to scan and record all channels at 3-second intervals. Of highest importance was the placement of displacement transducers to characterize the force-deflection relationship for each load case.

A total of 24 displacement transducers were used to measure vertical displacement profiles of Specimen 1. A line of nine displacement transducers were placed along the longitudinal axis of the wheel load. Five were spaced at 380 mm centers closest to the load plate and the remaining four spaced 760 mm either side. Nine displacement transducers were placed longitudinally in the same fashion at the center of the adjacent bay. Three displacement transducers were placed along the face of an exterior and interior beam to measure the “bedding in” of the beam to the strong floor. Fig. 29 illustrates a typical layout of displacement transducers for an overhang failure load of Specimen 1. The displacement transducers were individually clamped to W4x13 beams that sat on the strong floor, measuring the displacements at the deck soffit.

The instrumentation plan was altered for Specimen 2 to include six additional displacement transducers. The number of string pots increased from nine to fourteen along the longitudinal direction beneath the wheel load. This allowed equal spacing of displacement transducers, which assisted in inferring curvatures from the recorded data. Displacement transducers were spaced at 380 mm centers, with one either side of panel-to-panel seam. After reducing the data from Specimen 1 it was decided to remove the longitudinal line of displacement transducers in the bay adjacent to the wheel load. Due to the stiff nature of the bridge deck negligible displacement occurred at the adjacent bay, making the displacement transducers located there redundant. This allowed displacement transducers to be spaced at 380 mm centers in the transverse plane of the wheel load. As Load Cases 2.3, 2.4 and 2.8 were tandem axle (wheel) loads, transverse

profiles were measured in the axis of both wheels. A typical displacement transducer layout is shown in Fig. 30 for an overhang failure load of Specimen 2.

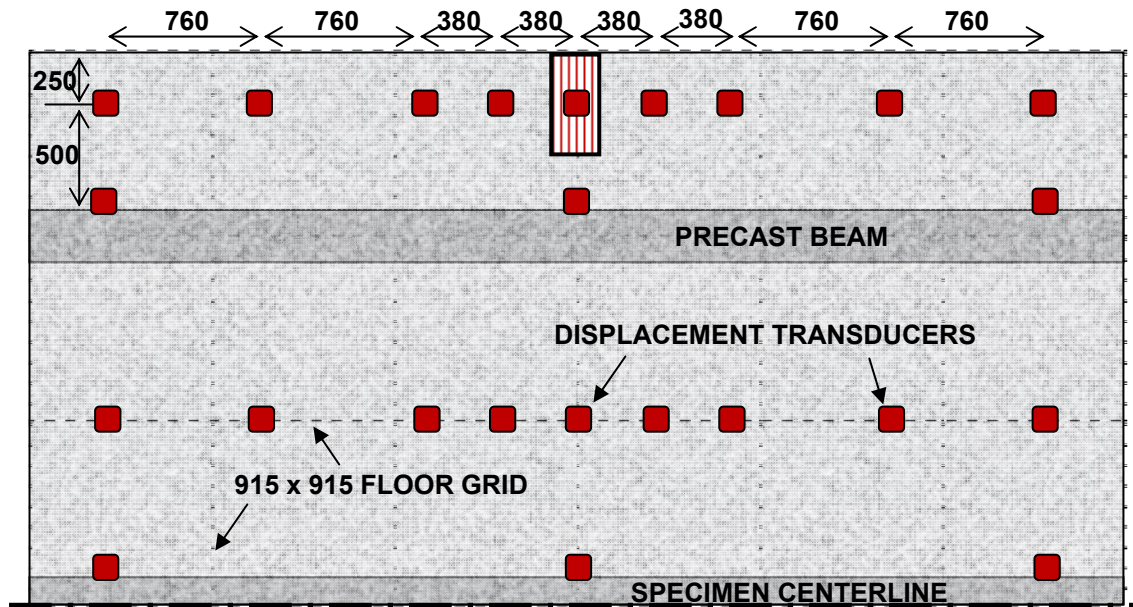


Fig. 29. Plan view of Specimen 1 instrumentation for overhang failure load (dimensions in mm)

In the precast prestressed overhang panels there were no strain gauges on the reinforcement as the panels were not instrumented when cast off-site. In Specimen 2 there were six strain gauges placed on the #5 (16 mm) transverse bars closest to the seam edge. These were spaced such that they were at the beam centerline and interior face for the exterior beams and both beam faces on the interior beam. An additional four gauges were placed on the middle longitudinal bar, at 100 and 600 mm on both sides of the seam.

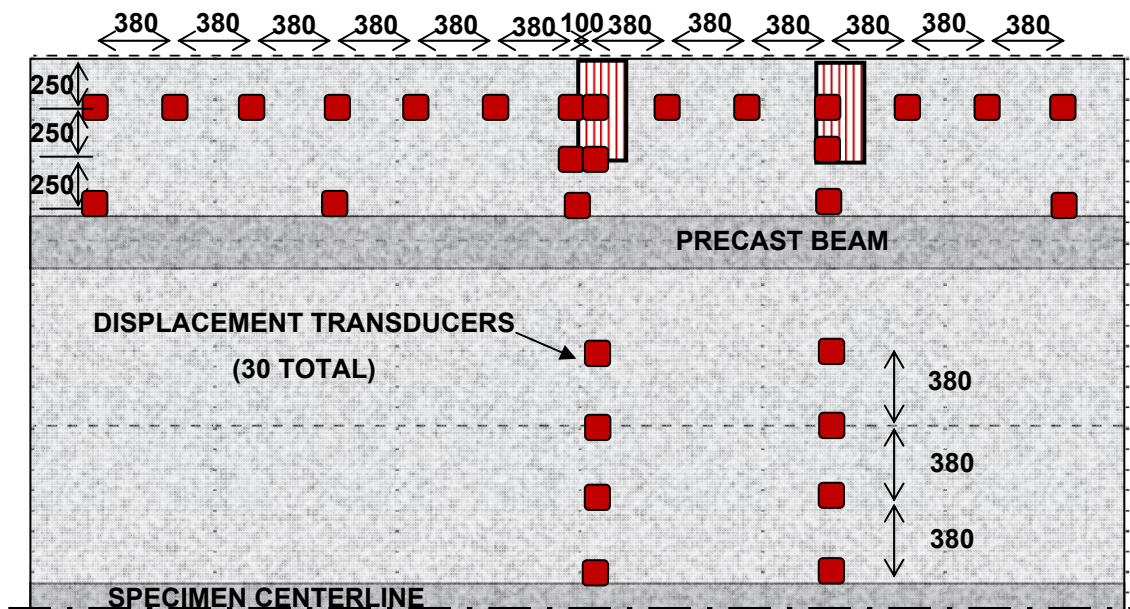
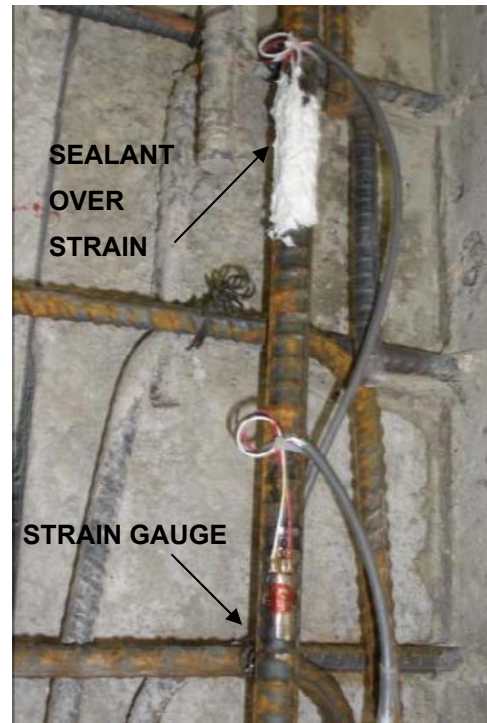
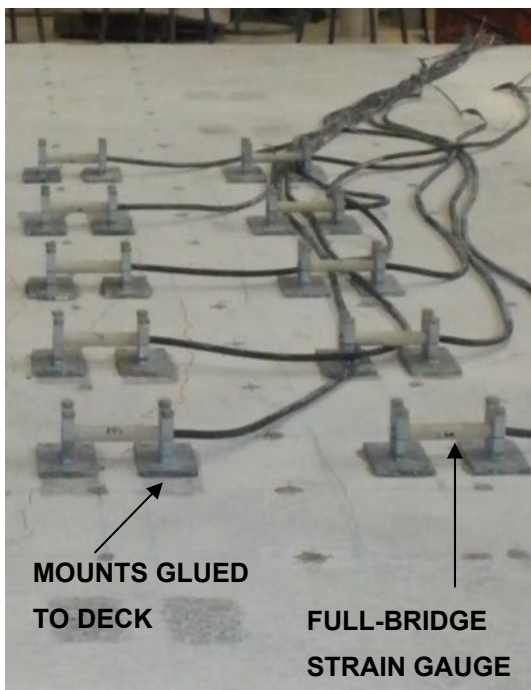


Fig. 30. Plan view of Specimen 2 instrumentation for overhang failure load (dimensions in mm)

In addition to the instrumentation, surface strains were measured with externally mounted (glued) full-bridge strain gauges on the top deck surface. Ten surface gauges were used, measuring transverse strains over the beam. Surface cracks, when present, were mapped at various load levels. Two shear connectors were instrumented with quarter-bridge strain gauges. These were on the connectors either side of the panel-to-panel seam. This allowed the measurement of the axial force acting on the shear connector while loading the overhang. Photographs taken of instrumentation used are shown Fig. 31.

(a) *Displacement transducers*(b) *Reinforcing strain gauges*(c) *Surface strain gauges*(d) *Shear connector gauges***Fig. 31.** Instrumentation used on bridge deck specimens

3.4 Experimental Grout Track

The complete filling of the haunch with grout between the full-depth overhang panels and girders is imperative on the bridge deck system performance. Voids and air bubbles will reduce the ability to provide uniform composite action on the exterior girders. For this reason, it was deemed necessary to perform a grout flow test on the SikaGrout™ 212 that was recommended for use in the haunch. A grout track measuring 400 mm wide by 4.88 m long, shown in Fig. 32, was formed from timber for this experiment. Reinforced concrete, with a wood float finish, was cast in the formwork to simulate the top flange of an AASHTO Type I concrete girder. The grout track was elevated on a timber frame that was angled to provide a 4% slope.



Fig. 32. Experimental grout track on 4% slope

Acceptable field haunch heights range from 12.5 mm and 75 mm. The experiment focused on testing both extremes, the first being the upper bound of 75 mm. Low-density foam (25 mm wide) was cut to 100 mm in height for the first test. The foam was attached to the girder via adhesive, as outlined in Chapter II, to provide a clear haunch width of 300 mm. This resulted in a 25 mm clear space between the foam and formwork to confirm the findings of the lateral resistance of the foam (Chapter III, Section 3.3.3). As seen in Fig. 32, a plexiglas cover was made to simulate the precast

concrete deck panel soffit. This provided a clear view of the grout flowability, along with identifying any voids or lateral failure of the haunch foam. The plexiglas frame was clamped and screwed to the grout track formwork, compressing the foam by 25 mm and creating the 75 mm haunch. The composite pockets were evenly spaced at 810 mm centers as in the precast overhang panel construction. In each of the pockets there were two 12.5 mm diameter threaded rods embedded into the concrete grout bed.

A SikaGrout™ 212 mix with a water-to-powder (w/p) ratio of 0.185 was mixed for the experiments. Grout was poured in the first composite pocket (having the lowest elevation) as shown in Fig. 33(a). The fluid nature of the grout allowed unpressurized flow to the next three composite pockets. Fig. 33(b) captures the grout level in the first three pockets under continued pouring in the first pocket. Once the grout level was 25 mm from the top of the first composite pocket a cover was placed in the pocket as demonstrated in Fig. 33(c). The cover was pushed down 50 mm above the bottom of the pocket, causing the grout to flow further. As illustrated in Fig. 33(d) this process continued at the next pocket until all pockets were sufficiently full. From the experiments conducted the grout was able to flow the full 4.87 m length of the grout track up a 4% slope for both a 75 mm and 12.5 mm haunch height.



a) *Pouring grout in first pocket*



b) *Continued pouring in first pocket*



c) *Placing grout cover on first pocket*



d) *Placing grout cover on second pocket*

Fig. 33. Placement of grout in experimental grout track

CHAPTER IV

EXPERIMENTAL RESULTS

4.1 Introduction

For all sixteen loading conditions, force-displacement data was obtained based on the wheel load and the vertical displacement below the center of the load plate. Displacement transducers were placed along the beam face to obtain the true panel deflection by allowing for compression and “bedding in” of the beam to the strong floor. This chapter presents the force-displacement results from the experiments conducted on Specimen 1 and Specimen 2. Longitudinal and transverse displacement profiles are plotted in Chapters V and VI, respectively, for overhangs and interior bays. Crack mapping is also presented in Chapters V and VI as it directly relates to the analyses performed. A summary of the results are provided in Table 7. Failure loads are highlighted in bold. All other load cases were loaded to the maximum factored loads as specified in AASHTO LRFD (2007) and presented in Chapter III of this thesis.

4.2 AASHTO Overhang Seam Load

Both precast overhang panel setups and lab-cast panels behaved in a similar fashion for Load Cases 1.1, 1.4, 2.1 and 2.5. For the precast overhang some hairline cracks were only observed at loads of 267 kN at the seam above the exterior beam face. The conventional overhang had three cracks on the underside of the deck propagating from the beam face. The cracks were continuous to the overhang free edge. Top surface cracks were observed above the beam face and along the beam centerline.

Fig. 34 presents the results for the AASHTO overhang wheel load at the longitudinal midpoint of the bridge deck (the transverse seam between precast panels). Vertical displacements obtained were small, with the largest displacement being approximately 0.3 mm, corresponding to a slab transverse rotation of 0.002 radians at the beam face.

Table 7. Load cases for tested double-panel bridge deck specimens

Load Case	Description	Peak Wheel Load (kN)
<i>Specimen 1</i>		
1.1	Conventional mid-specimen AASHTO load*	267
1.2	Conventional quarter-specimen AASHTO load*	267
1.3	Conventional mid-specimen edge load	476
1.4	Precast overhang mid-specimen AASHTO load*	267
1.5	Precast overhang mid-panel AASHTO load*	267
1.6	Precast overhang seam edge load	374
1.7	Axle load at panel quarter-point	535
1.8	Axle load at panel-to-panel seam	859
<i>Specimen 2</i>		
2.1	Precast overhang mid-specimen AASHTO load*	267
2.2	Precast overhang mid-panel AASHTO load*	267
2.3	Precast overhang tandem axle (wheel) load	360
2.4	Precast interior tandem axle (wheel) single panel	565
2.5	Lab-cast overhang mid-specimen AASHTO load*	267
2.6	Lab-cast overhang mid-panel AASHTO load*	267
2.7	Lab-cast overhang seam edge load	302
2.8	Lab-cast interior tandem axle (wheel) straddling seam	667

Bold signifies failure load

* AASHTO load = 267 kN (*Wheel Load + Multiple Presence Factor + Live Load + 75% IM for joints*)

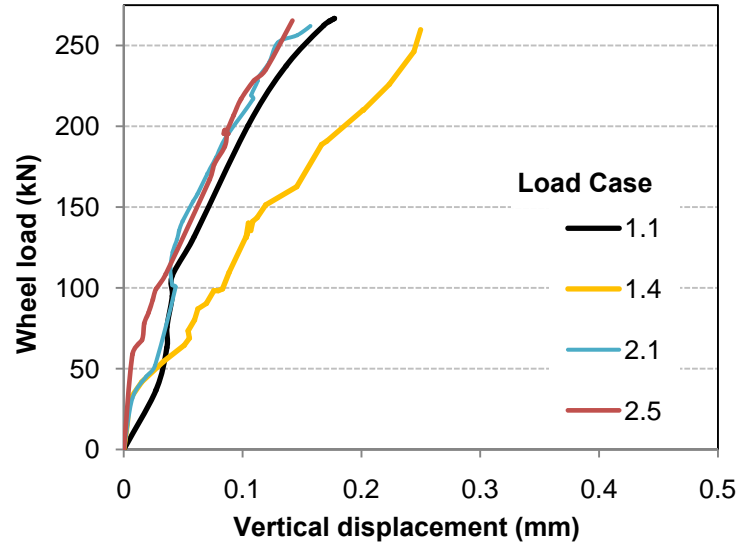


Fig. 34. Force-displacement for AASHTO load at overhang midspan

4.3 AASHTO Overhang Mid-panel (Quarter-point) Loads

The design AASHTO loading was applied at the longitudinal quarter point of both specimens. For the precast overhang, this corresponded to the longitudinal midpoint of a precast panel. No cracks were apparent in the surface of the precast panels. The conventional overhang had two hairline cracks on the underside of the deck in line with the load plate.

Force-displacement curves for these tests are presented in Fig. 35. In Specimen 1, the stiffness of the precast deck was similar to the stiffness of the conventional overhang, of approximately 1000 kN/mm. The stiffness values of the precast overhang and lab-cast sections of Specimen 2 were greater than that of Specimen 1. These tests on both specimens displayed neither cracks nor any residual displacements.

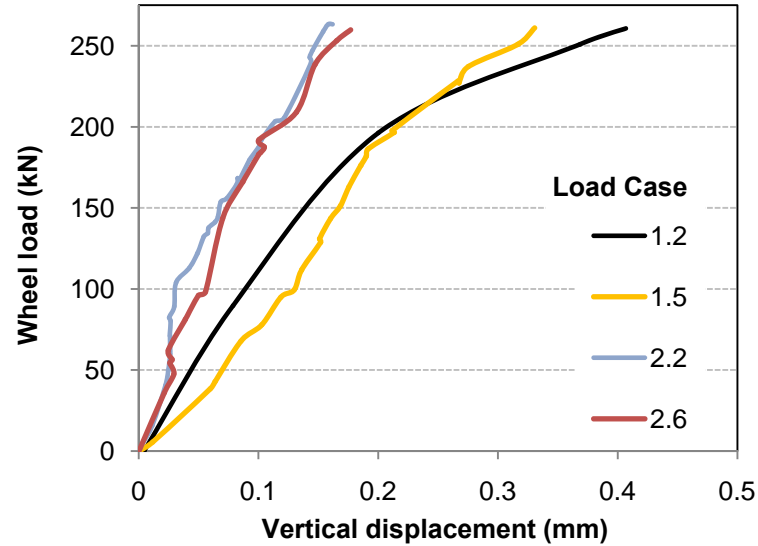


Fig. 35. Force-displacement for AASHTO load at overhang mid-panel

4.4 Overhang Failure Loads

A flexural failure mechanism in the overhang was achieved by moving the loading footprint to the edge of the deck. In Specimen 1, a single wheel load was placed on the edge of the seam for the precast overhang (Load Case 1.4). The lab-cast overhang in Specimen 2 was loaded the same way (Load Case 2.7). This provides an indication of the C-bar strength connecting adjacent panels in comparison to the continuous reinforcement in the conventional panel failure load (Load Case 1.3). From this the ability to transfer moment and shear forces between adjacent panels when loaded at a panel-to-panel seam can be experimentally validated. Specimen 2 used a tandem axle (wheel) load applied over the same precast overhang panel (Load Case 2.3).

Cracks were mapped at selected loads based on the force-displacement data obtained during the experiment. The conventional overhang failure was almost symmetric about the load plate. For the precast loads, cracks were observed in the panel adjacent to the panel loaded. The force-displacement curves for Load Cases 1.3, 1.6, 2.3, and 2.7 are shown in Fig. 36. The curves indicate that the initial stiffness was similar for the precast panels and CIP overhang with a single applied load up to approximately 133

kN. Up to approximately 200 kN the force-displacement behavior is similar for the precast and conventional overhangs loaded at the seam. For Specimen 1, the ultimate load capacities were 476 kN and 374 kN for the CIP and precast overhangs, respectively. The 21 percent reduction in load carrying capacity in the full-depth precast system is attributed in part to the presence of the seam in the precast system.

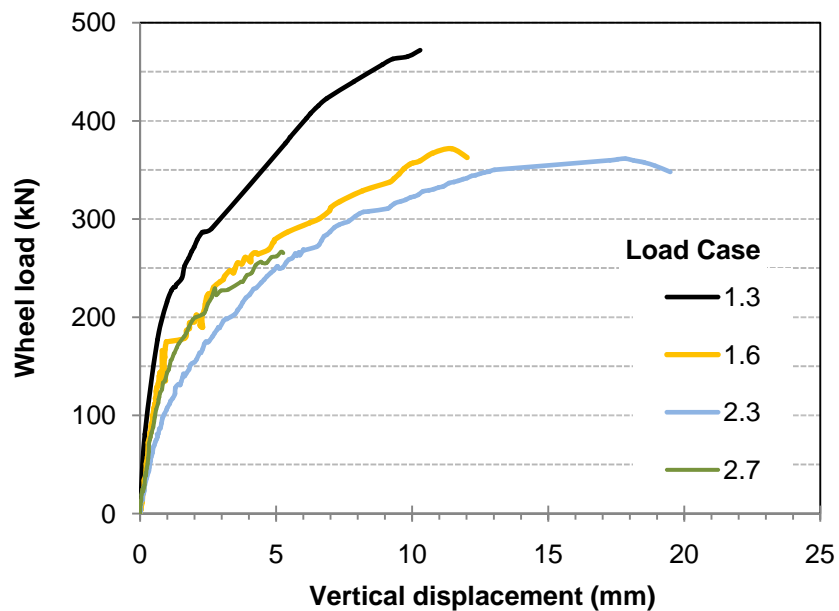
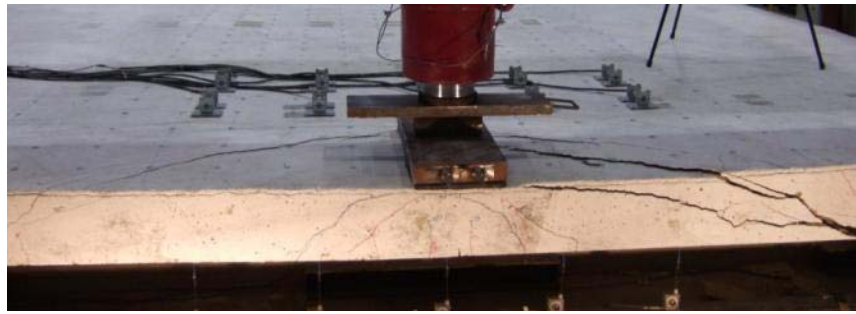


Fig. 36. Force-displacement for overhang failure loads

Photographs were taken after failure for the four overhang failure load cases. Fig. 37 presents observed failures for Load Cases 1.3, 1.6, 2.3 and 2.7. The precast prestressed overhangs had a rake finish on the deck surface, restricting the visibility of cracks. For this reason Figs. 37(b) and 37(c) only capture the largest visible failure crack that is representative of the failure mechanism.



(a) *Load Case 1.3: Conventional overhang*



(b) *Load Case 1.6: Precast prestressed overhang loaded at panel-to-panel seam*



(c) *Load Case 2.3: Precast prestressed overhang with tandem axle (wheel) load*



(d) *Load Case 2.7: Lab-cast overhang loaded at panel-to-panel seam*

Fig. 37. Observed failure modes for Specimens 1 and 2 overhangs

4.5 Interior Loads

Load Cases 1.7 and 1.8 consisted of two simultaneously applied wheel loads via a spreader beam that represented a truck single axle. One wheel pad was placed in each of the two interior bays of Specimen 1. In Specimen 2, Load Cases 2.4 and 2.8 also consisted of two simultaneously applied wheel loads, 1.22 m apart, to represent tandem wheel loads. These were applied along a midspan line parallel to the longitudinal axis of the bridge. In this way, the AASHTO LRFD tandem axle condition for one bay (between beams) was represented. In Load Case 2.4 the two loads were placed within one panel adjacent to the seam. In Load Case 2.8 the tandem loads were placed with one near the center of the panel and the other straddling the adjacent panel. The purpose of the comparison was to highlight the possibility of any difference in the imposition of bending and the possibility of shear stresses across the seam.

Specimen 1 had a few surface cracks for both load cases, all of which were confined on the beam faces. Flexural-punching shear failure occurred on the interior beam of the precast side at 850 kN. Fig. 38 provides the results of all interior failure loads (Load Case 1.8, 2.4, and 2.8) as well as quarter-point loads (Load Case 1.7). It is evident that Load Case 2.4 is the critical case in the tandem axle (wheel) load over a single panel. However, the initial stiffness in all load cases is comparable up to approximately 311 kN for loading near the seam. Note that this is well in excess of the maximum factored AASHTO load (~200 kN). Behavior beyond 311 kN is still satisfactory, with a moderate degree of ductility (failure warning) exhibited.

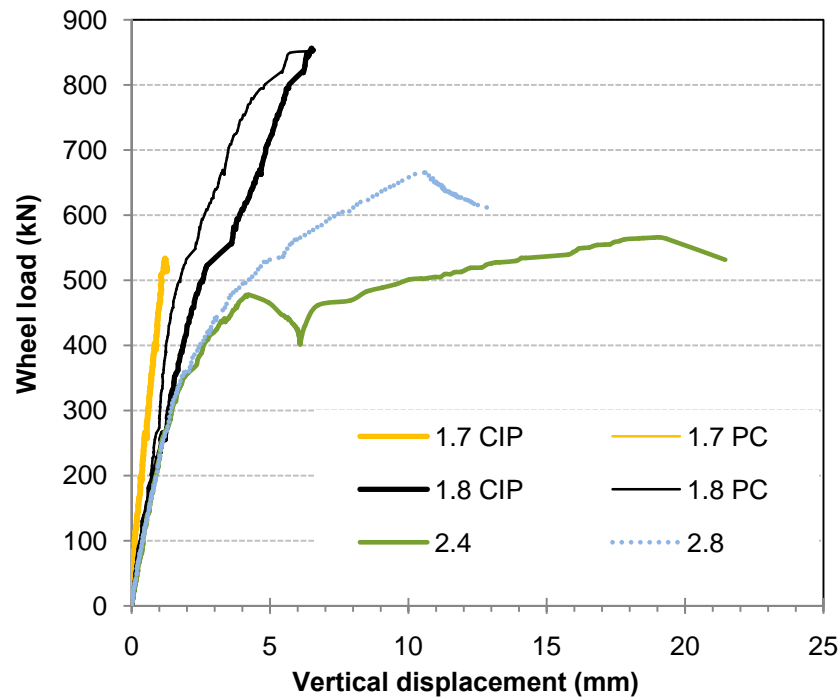


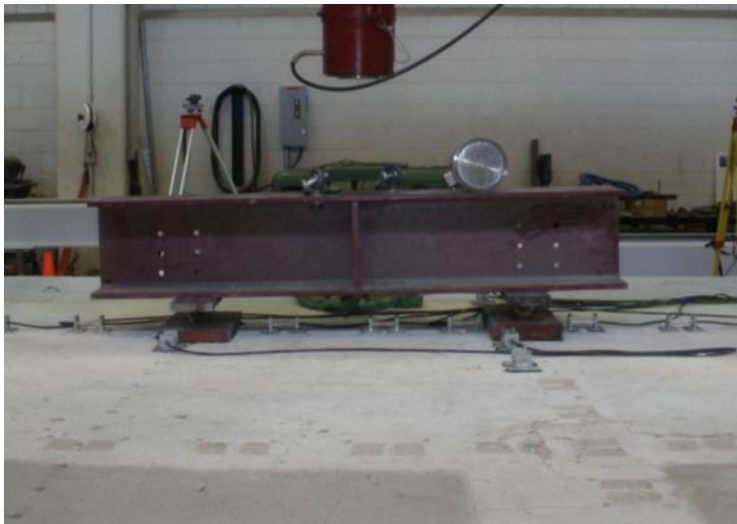
Fig. 38. Force-displacement for interior failure cases

Note: PC = precast deck, CIP = cast-in-place deck

Fig. 39 provides photographs after failure for Load Cases 1.8 and 2.8. Load Case 2.4 (tandem axle straddling seam) was omitted as it was similar to Load Case 2.8 (tandem axle on single panel at seam). Interior failure photographs are not truly representative of the failure mechanism observed. The panel soffit exhibited excessive cracking and delamination. This could not be captured by photographs due to limited space under the bridge deck.



(a) *Load Case 1.8: Axle wheel load (taken on precast panel)*



(b) *Load Case 2.8: Tandem axle load straddling seam*

Fig. 39. Observed failure modes for Specimen 1 and 2 interior bays

4.6 Additional Measured Strains

In the pocket closest to the seam, for both precast overhang panels, strains in one shear connector were recorded. The maximum tensile stress recorded was 44 MPa, a minimal value for a rod with yield stress of 724 MPa. Top mounted surface strain gauges provided little useful information as the gauge slipped when cracking occurred through the glued mounting plate. The half-bridge strain gauges attached to the steel reinforcing of Specimen 2 provided an indication of when the steel yielded. Fig. 40 shows the normalized strain observed on the #4 (12.5 mm) top transverse reinforcement. Hence, at the 267 kN load, the bars remained elastic (~55 percent of yield) over the beam centerline. The ultimate load yielded the bar from the beam centerline to approximately 380 mm beyond the interior beam face. Based on an evaluation of the strains and load deformation behavior, it is apparent that a full failure mechanism did not form until the load reached approximately 347 kN.

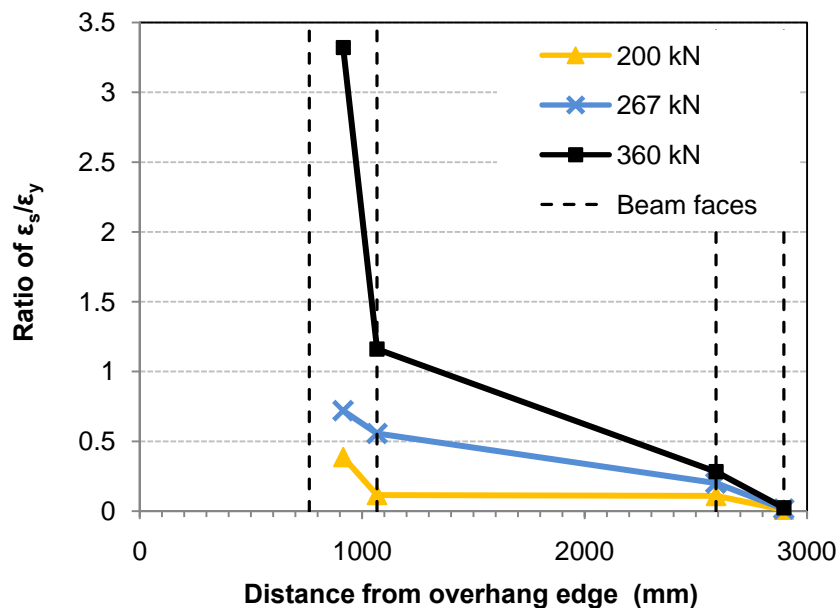


Fig. 40. Transverse bar strains in precast prestressed overhang of Specimen 2

4.7 Discussion

Results from the overhang tests indicate that the precast overhang system exhibits sufficient capacity for a 915 mm overhang. Table 8 lists the observed load factors (factors of safety) obtained from ultimate failure loads. Note that these are only for the capacity of the precast overhang system, not the bridge as a whole. The 21 percent decrease in carrying capacity in the precast overhang panel compared to the conventional overhang cannot be solely attributed to the seam. Firstly, it should be noted that although constructed to be similar, the properties of the materials used in the two overhangs were different. The yield stress of the #5 (16 mm) top transverse reinforcing steel bars was 468 MPa for the CIP overhang compared to 434 MPa in the precast overhang. Second, the precast system had a considerably smaller positive moment in the longitudinal direction at the seam ($M_y = 31.0$ kNm/m for precast and $M_y = 72.5$ kNm/m for CIP). This was due to the conventional overhang using bottom longitudinal #5 (16 mm) steel reinforcement while the precast side used a welded wire mesh of #3 (9.5 mm) rounded bars providing 465 mm^2 of steel per meter.

Table 8. Peak loads and factors of safety for ultimate failure load cases

Load Case	Peak Wheel Load, kN	Reserve capacity factor (ultimate/load factor)
Exterior		
1.3	476	2.38
1.6	374	1.40
2.3	360	1.35
2.7	302	1.13
Interior		
1.8	859	3.30
2.4	565	2.83
2.8	667	3.34

Note: 200 kN design load = Wheel Load + Multiple Presence Factor + Live Load + IM 33%

267 kN design load = Wheel Load + Multiple Presence Factor + Live Load + IM 75% for joints

Tandem wheel: 200 kN design load = Wheel Load + Multiple Presence Factor + Live Load + IM 75%

A further reduction in ultimate capacity was observed when loading the lab-cast overhang when compared with the precast prestressed overhang. The effect of transverse

prestressing in the lower half of the precast overhang is small in the negative moment overhang region. The main contribution in strength is from the top transverse #5 (16 mm) steel in this region. Reduction in the ultimate capacity in the lab-cast specimen was likely due to the bottom reinforcement layout. The #5 (16 mm) steel reinforcing bars were designed and placed to mimic the conventional section and not the steel mesh used in the precast prestressed overhang panels. The development length of the reinforcing thus increases at the transverse seam where the steel is terminated in each panel. Strength is compromised as the #5 (16 mm) bars are not developed within the failure plane of the lab-cast panels. Due to the increase in development length there is effectively no positive reinforcement in the longitudinal direction ($M_y = 0$ kNm/m) at the point of failure. An increase in strength would be expected had the #5 (16 mm) reinforcing bars had standard hook length, or a mesh been used in the lab-cast panels.

Greater ductility was observed in the precast overhang panel when compared to the conventional panel and lab-cast systems. In terms of total loads on a panel, Load Case 2.3, which represented tandem axles on a single panel, does not appear to adversely affect the ultimate capacity. Although the ultimate failure load is within 4.5 kN of the single wheel seam load, the stiffness was reduced for this load case. A folding mechanism along the beam face was observed, resulting in larger ultimate vertical displacements of 20 mm compared to 12 mm for the singular seam load.

4.8 Experimental Conclusions

Based on the results from the two full-scale double-panel specimens, the following conclusions can be drawn:

1. The concept of using conventional SIP panels and a precast overhang panel to construct a concrete deck system was verified. Current AASHTO-based designs have substantial reserve strength over the required AASHTO design factored loads. In spite of minor (21 percent) weakening being introduced via the transverse panel-to-panel seam, the full-depth, precast prestressed panels also showed sufficient strength in both interior and exterior bays.

2. Overhang failure loads were made critical by loading at the edge of the panel and seam joint. It is evident that the introduction of the seam decreases the overall strength, but only the bottom longitudinal steel is discontinuous. Nevertheless, some positive (and negative) moment strength is still provided due to the CIP panel-to-panel joint that has a single layer of C-bars. Although this is weaker than the full-depth overhang, the overall reduction of load carrying capacity is only some 21 percent, and based on this research is considered safe for general implementation.
3. Under normal service loads (including overloads), the stiffness of the full-depth precast-prestressed panels was comparable to the conventional CIP decks. Under normal service loads deck cracking should not be expected.

CHAPTER V

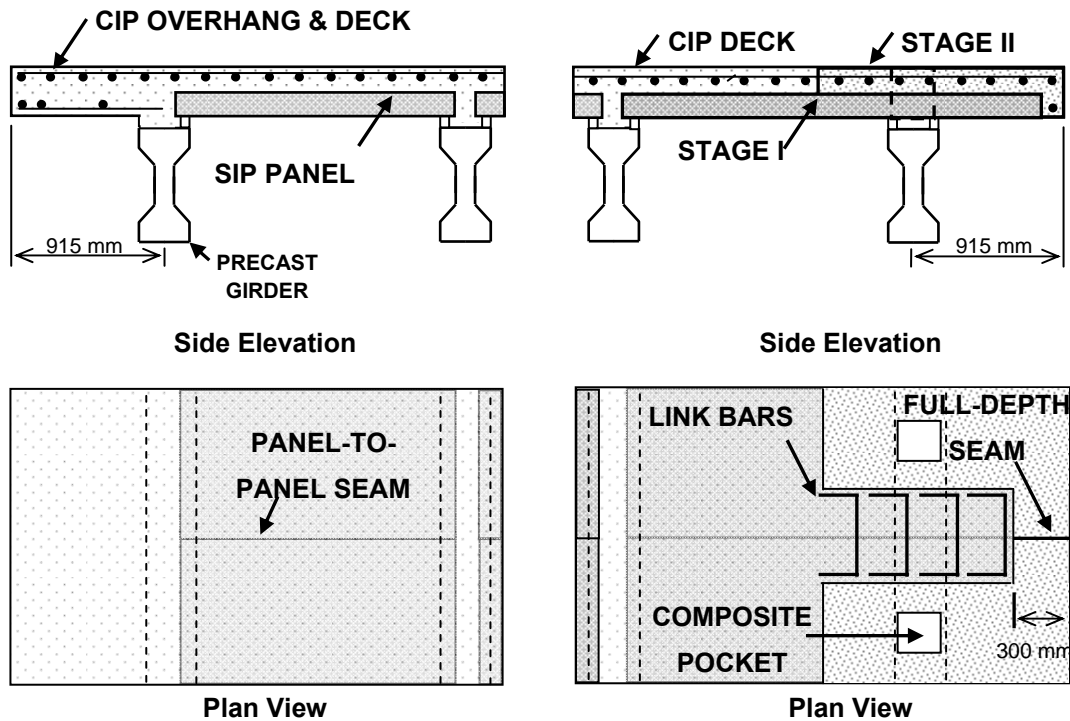
ANALYTICAL INVESTIGATION: EXTERIOR

5.1 Introduction

One common form of concrete slab on girder construction of bridge decks is to use half-depth stay-in-place (SIP) precast prestressed panels that span between interior girders. The panels are prestressed transversely to the direction of traffic and are nominally 100 mm thick. A second stage reinforced cast-in-place (CIP) concrete pour provides composite action across the deck. SIP panels have been used since the 1950s and their performance is well documented (Jones and Furr (1970), Buth et al. (1972) and Tsui et al. (1986)) for use on bridges with either precast concrete girders or steel girders. However, to provide composite action between the bridge deck and girder, half-depth SIP panels cannot be used in the deck overhang that extends beyond the fascia girder. Thus, as shown in Fig. 41(a), a full-depth CIP concrete overhang is cast at the same time as the second stage closure pour. Unlike the SIP precast prestressed panels the performance of the overhang has been widely overlooked. Conventional construction, based largely on empirical design, extends the top reinforcement from the interior portion of the deck to the overhang. Bottom mild steel reinforcement in the overhang is minimal to meet temperature and shrinkage requirements.

Fig. 41(b) illustrates the newly proposed full-depth overhang system. The overhang panels are cast in two stages. Stage I is cast in the same long-line prestressing bed as the regular SIP panels. The panels are cast sufficiently long to provide a 915 mm overhang (from the fascia girder centerline), and extend to be seated on the first interior girder. For Stage II, a reinforced concrete pour is cast once the strands have been released making a full-depth system. The panels are placed adjacent to one another along the bridge length with no shear connection between panels. Continuity only exists between the panels over the top 100 mm CIP closure pour to complete the bridge deck. Continuous steel is placed across the seam at the interior bays and C-shaped reinforcing

bars connect hooked bars that extend from the Stage II pour. As shown in Fig. 41(b) there is no continuity between adjacent panels over a 300 mm width at the edge of the overhang.



(a) Conventional concrete bridge deck construction (b) Newly developed full-depth precast overhang

Fig. 41. Comparison of two overhang systems

Limited work has been done on the strength of conventional exterior overhangs, let alone full-depth precast overhangs that include joint effects. Full-depth panels have been experimentally validated for strength by Issa et al. (1995), Yamane et al. (1998), and Fallaha et al. (2004). Research has not been directed on analyzing these systems thus optimizing reinforcing details, rather validating systems with typical as-built steel layouts. This is also the current practice with CIP bridge decks that use empirical design as per American Association of State Highway and Transportation Officials (AASHTO)

Load and Resistance Factor Design (LRFD) Bridge Design Specifications (2007). The ductility of such bridge decks is typically low due to high steel ratios. Experiments conducted on such decks by Taylor and Hayes (1965), Beal (1982), Fang et al. (1994), and Graddy et al. (2002), found that brittle bending compression failures occurred and were attributed to punching shear failures. These loads were much higher than the predicted loads using the punching shear formulas of either AASHTO LRFD Bridge Design Specifications (2007) or ACI Committee 318 (2008). Analytical work by Hewitt and Batchelor (1975), Csagoly and Lybas (1989) and Mufti and Newhook (1998), modified the punching-shear theory by accounting for boundary restraints. However, due to reduced boundary constraint at the bridge overhang a punching-shear failure is less likely to occur than when loading at an interior bay.

Both flexural and shear failure modes at the overhang must be investigated to determine which of the two modes govern. Flexure has not been particularly well researched for concrete bridge deck slabs as they are typically thick, and often thought to be governed by shear. However, shear alone rarely occurs in practice; a measure of flexure is also present.

For flexure, load capacities for two-way slabs can be assessed using either yield line theory or lower bound strip methods (Park and Gamble, 2000). The former method lends itself to analysis and copes well with point (wheel) load effects, whereas the latter is commonly used for design and is implicit in present AASHTO LRFD Bridge Design Specifications (2007) by virtue of specifying an equivalent width. Flexural analysis of slab overhangs using yield line theory is investigated in this chapter and compared to experimental findings. These experiments loaded bridge deck slabs at the overhang edge, and at a panel-to-panel seam for full-depth overhang panels. A modified yield line theory is proposed to account for debonding of bars at the free edge of the slab. On the precast overhangs an interaction between flexure a loaded panel and shear at the panel to panel seam is investigated. Yield lines are supported by crack maps and longitudinal and transverse displacement profiles from which curvatures are inferred.

5.2 Failure Load Analysis

To understand the failure mode and collapse capacity of concrete bridge deck overhangs it is appropriate to investigate the use of different analysis techniques. First, code based predictions such as limit analysis approach for flexure and punching-shear are used to determine the predicted failure load. Yield line theory is used to analyze the flexural failure load of critical overhang sections. Based on these results the yield line theory is adapted to allow for partially bonded reinforcing bars. Combined shear-flexure mechanisms are then derived for the precast overhangs. The internal work equation is modified to allow for a flexural failure of the loaded panel with a simultaneous shear failure along the seam between the overhang panels.

5.2.1 Yield line theory

Yield line theory is an upper bound limit analysis method used for determining the collapse load capacity of two-way slab systems based on prescribed boundary conditions. Sufficient shear strength is assumed so a flexural failure governs alone. In yield line theory, it is also implicitly assumed that sufficient ductility is available to allow plastic rotation to occur along the yield lines to enable a full collapse mechanism to form. For analysis, external work done (EWD) is equated with the internal work done (IWD) for a specified admissible mechanism. Many admissible mechanisms may exist, however it is the mechanism that leads to the *lowest* collapse load via the least amount of work done is the correct mechanism. Full details of the approach are found in Park and Gamble (2000).

Due to second-order geometric effects, compression membrane behavior can lead to higher post-mechanism slab resistance as seen in Graddy et al. (2002). For membrane action to work, substantial displacements are needed. As the experiments in this study produced relatively small displacements, and compression membrane effects were not observed, it is disregarded herein from further consideration.

Yield line theory, in its traditional (unmodified) form has been applied to the experimental test conditions for the different sub-tests investigated in this research.

Conventional yield line theory generally showed results that were somewhat higher than the experimental observations. It is tempting to dismiss these differences and ascribe them to the fact that yield line theory is an upper bound solution method. However, as the form of the predicted mechanism was in agreement with experimental observations it became evident that the yield line method of analysis, in its current form, was not strictly appropriate and was thus modified.

5.2.2 Modified yield line theory

The conventional yield line theory is adapted herein to account for partially bonded bars. For a cantilever slab, such as shown in Fig. 42, traditional yield line theory assumes all bars along the plastic hinge line have yielded out to the edge of a slab. Clearly, this implicit assumption is not strictly valid; each reinforcing bar transverse to the slab edge requires a development length in order to form its full yield stress.

The overall moment on a given yield line needs to be reduced accordingly. Specifically, that contribution near the slab boundaries in the development zone needs to be removed from the internal work contributions. The basic tension development length is given in AASHTO LRFD Bridge Design Specifications (2007) for deformed bars and deformed wire in tension. For the experiments conducted, the basic development length is equal to the tension development length with each modification factor taken as unity. For deformed bars smaller than 36 mm, the tensile development length, l_d , is

$$l_d = 0.105A_b f_y / \sqrt{f'_c} \geq 0.058d_b f_y \geq 300 \text{ mm} \quad (1)$$

in which A_b = area of individual reinforcing bar (mm^2), f_y = measured yield strength of reinforcing bar (MPa), f'_c = measured compressive strength of concrete at time of experiment (MPa), d_b = nominal diameter of reinforcing bar (mm).

5.2.3 Yield line analysis

Consider the case of a conventional overhang, with the assumed yield line shape, as shown in Fig. 42. Note that positive moments (compression on top surface, or tensile cracks on the soffit) are drawn in jagged solid lines while negative moments (tension cracks on top surface) are drawn in dashed lines. It is therefore shown that the principle of virtual work requires the following:

$$\text{EWD} = P_u \delta + w_d \left(l_x l_y \frac{\delta}{3} + b_1 l_x \frac{\delta}{2} \right) \quad (2)$$

$$\text{IWD} = \sum M_x \alpha_x l_y + \sum M_y \alpha_y l_x \quad (3)$$

For the displacement profiles of Fig. 42(a) and (b) this results in the following outcome.

$$\text{IWD} = \frac{2M'_x}{l_x - 0.5b_2} (l_y + 0.5b_1) \delta + 2(M_y + M'_y) \frac{l_x^2}{l_y(l_x - 0.5b_2)} \delta \quad (4)$$

where x and y denote transverse and longitudinal directions respectively, thus M_x , and M_y = positive moment capacities in the transverse and longitudinal directions, M'_x and M'_y = negative moment capacities in the transverse and longitudinal directions, l_x and l_y = length of the yield lines in the transverse and longitudinal directions, α_x and α_y = rotation of slab about yield line about transverse and longitudinal axes, P_u = failure load, w_d = self-weight of slab, b_1 = short side of reaction area, b_2 = long side of reaction area and δ = arbitrary vertical displacement at the location that P_u is applied.

By equating (2) and (4) the failure load P_u is determined based on the calculated moment capacities. The method of virtual work is modified to accommodate the partially bonded region of each rebar. This distance is given in Fig. 41a) based on the same geometry shown. The external work done remains the same as before in (2), however the internal work equation is modified as follows:

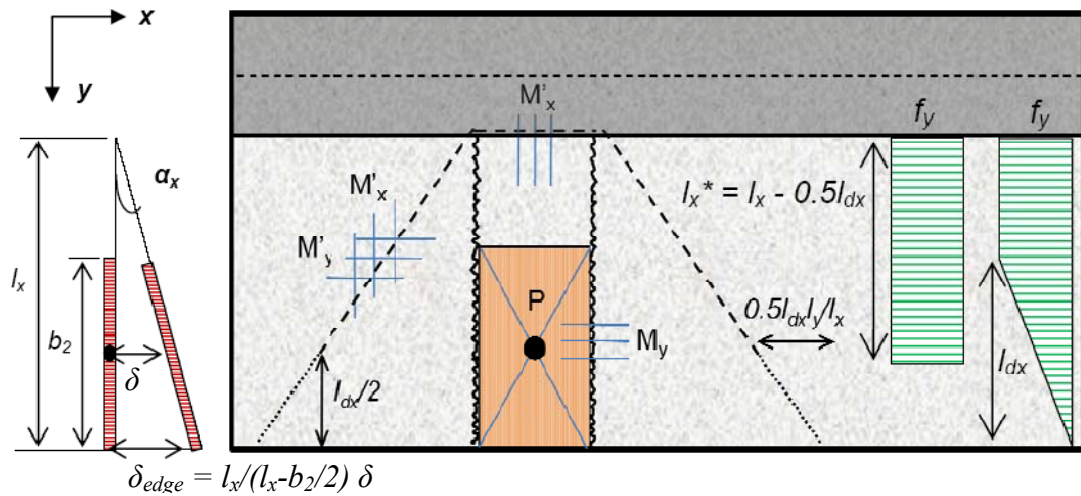
$$\text{IWD} = \sum M_x \alpha_x l_y^* + \sum M_y \alpha_y l_x^* \quad (5)$$

where l_x^* and l_y^* are the modified lengths taking into account the partially bonded bars.

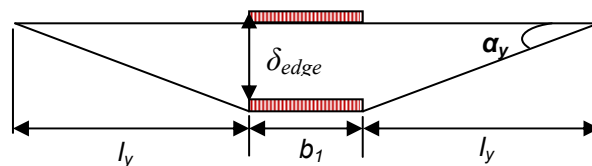
For the example shown in Fig. 42, the IWD equation reduces to:

$$\text{IWD} = \frac{2M'_x}{l_x - 0.5b_2} \left(l_y \left(1 - \frac{l_{dx}}{2l_x} \right) + 0.5b_1 \right) \delta + 2(M_y + M'_y) \frac{l_x^2}{l_y(l_x - 0.5b_2)} \delta \quad (6)$$

where l_{dx} is bond length of the transverse reinforcement determined by (1). Clearly the effect of partially bonded rebars results in a decrease in the internal work done and hence the failure load. For an overhang slab system this reduction can become substantial as the ratio of development length to cantilever length increases.



(a) Plan view of yield line theory subjected to load P , with assumed and actual transverse bar stress shown



(b) Front elevation: assumed displacement profile

Fig. 42. Assumed yield line mechanism for conventional overhang loaded to failure

5.2.4 Mixed shear-yield line mechanism at the seam

In experiments a mixed failure mode appeared to occur when the wheel load was placed immediately adjacent to the seam. In the reduced depth 100 mm instead of the normal full slab 200 mm region that constituted the panel-to-panel seam, high shear developed and led to partial shear failure along the seam line. The remainder of the mechanism was of the conventional (modified) yield line type.

5.3 Experimental Displacement Profiles and Inferred Curvature Results

Slab behavior is difficult to predict due to complex two-way interaction. It is therefore instructive to first examine the experimental deformation patterns observed during testing. This sub-section provides experimental results for the four exterior load cases (Load Cases 1.3, 1.6, 2.3 and 2.7). Displacement profiles are plotted at various loads up to those measured just prior to failure. From the displacement profiles corresponding curvatures were calculated based on finite difference solutions found in Appendix II. Curvature plots include the yield curvatures which were calculated analytically through moment-curvature relationships of the deck sections. Table 9 provides the theoretical longitudinal yield curvatures and subsequent yield load based on inferred curvatures. Due to insufficient displacement transducers in Specimen 1, the transverse direction curvatures could not be accurately predicted using finite difference theory.

Table 9. Summary of yield loads and failure curvatures for longitudinal profiles

LOAD CASE	Experimental failure load, kN	Longitudinal yield load, kN	Dimensionless curvature (milliradians)		Curvature ductility at incipient failure (Φ_f/Φ_y)
			Theoretical yield, $\Phi_y H$	Experimental failure, $\Phi_f H$	
1.3	476	387	4.64	7.04	1.52
1.6	374	303	4.00	6.56	1.64
2.3	360*	245	4.00	9.12	2.28
2.7	302	302	4.64	4.16	0.90

*Load applied per "wheel" footprint.

5.3.1 Load Case 1.3

Fig. 43 presents the results for longitudinal and transverse displacement profiles and longitudinal curvatures for Load Case 1.3. Fig. 43(a) provides the longitudinal displacement profile at the selected load increments. From these total deflections finite differences were applied to obtain the curvature distribution as presented in Fig. 43(b). Included in this figure are the cracking curvatures and first yield for negative and positive yield curvatures of the top and bottom reinforcement respectively. Back-analysis of the test results showed that first yield of the bottom longitudinal steel occurred at a load of 387 kN. At incipient failure, the observed curvature reached $1.52\Phi_y$. Fig. 43(b) indicates that yielding spread some 190 mm either side of the centerline 65 mm wider than the load plate either side. The cracking load was difficult to determine due to the low magnitude of curvature at which this occurred. However, it is conclusive that at 200 kN there was some cracking on the bottom of the slab, over a 762 mm width, with some cracks starting to propagate on the top surface. This is supported by the cracks that were observed and mapped during the experiment.

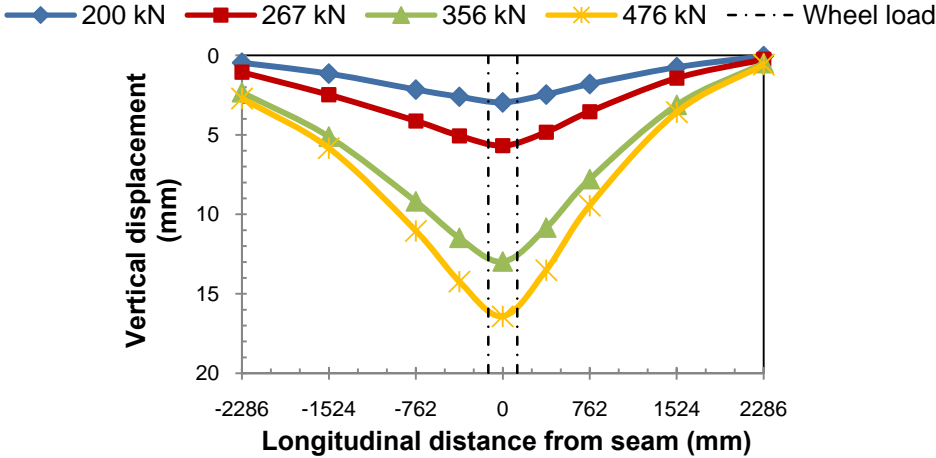
The transverse displacement profile for Load Case 1.3 is presented in Fig. 43(c). Due to an unlevel laboratory floor surface the beam displaced downwards with the application of the vertical load. An inadequate number of displacement transducers prevented curvatures from being calculated at the beam face, but it is evident from Fig.

43(c) that the rotation at the beam face increased greatly from the 267 kN load to the 356 kN load, implying non-linear behavior of the overhang due to yielding of the reinforcement transverse to the support beams.

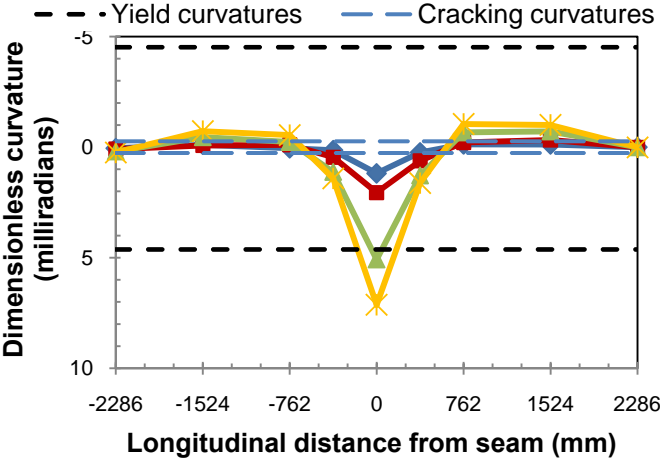
5.3.2 Load Case 1.6

Fig. 44 presents the results for Load Case 1.6 (precast-prestressed overhang failure) at intermediate loads and ultimate failure load. The differential displacement is shown in Fig. 44(a) at the seam of the panels due to the load plate being positioned on the edge of a panel. This resulted in the most adverse load case, as the seam was required to transfer load to the adjacent panel. The loaded panel reached the longitudinal yield load at approximately 303 kN based on Fig. 44(b). The dimensionless curvature at failure of the loaded panel was 6.56 milliradians, a factor of $1.64\Phi_y$. The adjacent panel was subjected to a hogging moment, with tensile curvatures on the top deck surface just exceeding the cracking curvature capacity. This agreed with the cracking patterns observed with cracks only occurring on the top slab surface.

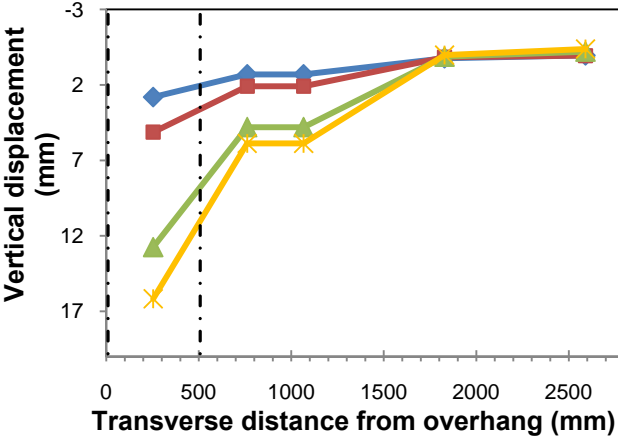
Fig. 44(c) presents the transverse displacement profile for Load Case 1.6. The displacement of the interior section is negligible at the first measured location, and remains null for all load increments. Similar to Load Case 1.3, insufficient data points were recorded to calculate curvatures at the beam face. It is observed that the vertical displacement increased substantially when loaded from 267 kN to 356 kN, due to plastic rotation.



(a) Longitudinal displacement profile

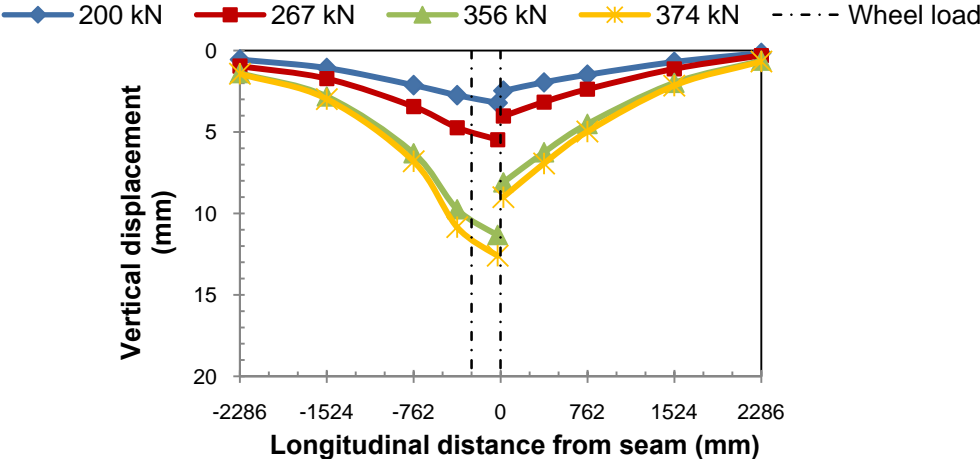


(b) Longitudinal curvature profile

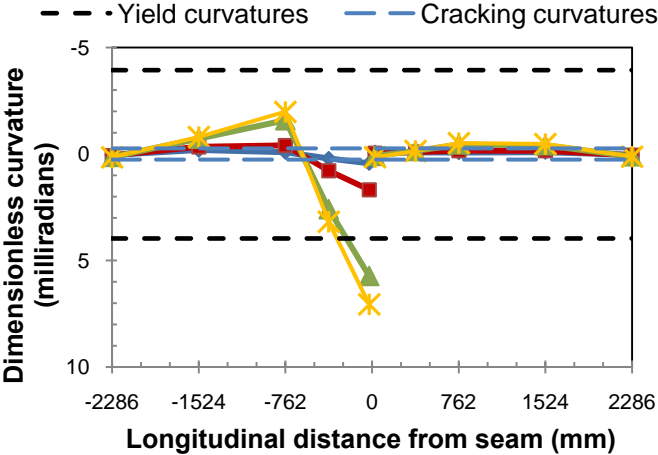


(c) Transverse displacement profile

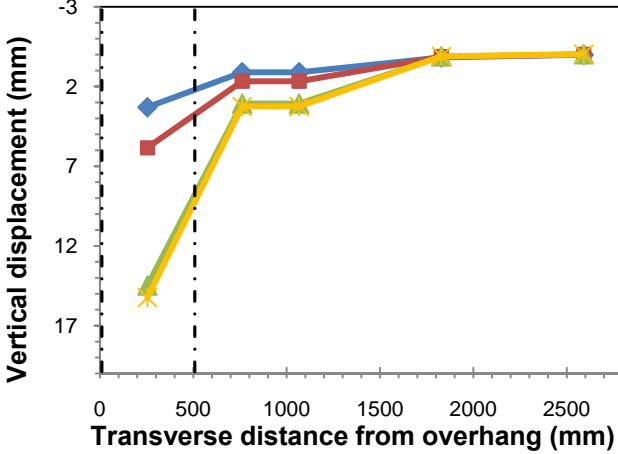
Fig. 43. Load Case 1.3 – conventional overhang loaded to failure at 476 kN



(a) Longitudinal displacement profile



(b) Longitudinal curvature profile



(c) Transverse displacement profile

Fig. 44. Load Case 1.6 – precast prestressed overhang loaded to failure at 374 kN

5.3.3 Load Case 2.7

Fig. 45 presents results for Load Case 2.7, the lab-cast overhang loaded with a central edge load to failure. The longitudinal displacement profile in Fig. 45(a) shows a load of 267 kN with a displacement of 7 mm compared to 5 mm for the precast-prestressed panel. This difference may be attributed to the stiffening effect of the prestress (Stage I pour of precast overhang panel) in contrast to mild steel as bottom reinforcing in the lab-cast panels. This transverse bottom steel in the lab-cast panels was discontinuous through the beam, in effect making a negligible contribution to the transverse (M_x and M'_x) moment capacity.

It can also be observed that there was a large increase in displacement between 267 kN and at failure, 303 kN, of the lab-cast panel. The failure displacement of 11 mm was similar in magnitude to the 356 kN load for the precast-prestressed panel. Furthermore, the relative displacement between the two panels at this similar displacement was both around 4 mm, suggesting that the seam behaved in a similar fashion in both experiments. This supports the argument to be made on the effect of having panels continuously prestressed (or reinforced) across the support beam on the ultimate capacity of the slab.

From Fig. 45(b) it is seen that the curvature at failure at the seam was $0.90\Phi_y$. This supports the observation that at the seam a shear rather than a flexural failure occurred. Nevertheless, it is possible that yield was reached at failure, but was not captured due to the sudden failure of the slab. This was seen in the electronic displacements recorded, with the yield curvature succeeded after the panel failed. A similar argument can be made for the formation of the negative moment capacity measured -762 mm from the seam. The failure mechanism cracks propagated through this location suggesting that yielding of the top steel did in fact occur at this location.

Fig. 45(c) plots the transverse displacement profile for the lab-cast overhang failure load. From the plot it is evident that nonlinear response took place when the load was increase to 298 kN to 267 kN. At this point the calculated dimensionless curvature was $\Phi H = 3.76$ milliradians, or $\Phi = 0.75\Phi_y$. This is comparable with the measured

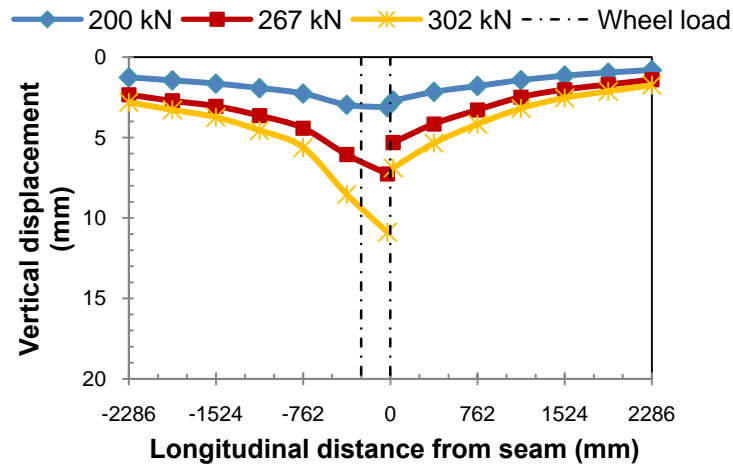
internal strains on the transverse reinforcement, which showed a maximum strain of $0.86\varepsilon_y$ was achieved. However, using central difference analysis the inferred curvature at the edge of the load plate was $\Phi H = 14.16$ milliradians, or $\Phi = 2.80\Phi_y$. This agrees with the assumed failure mechanism where yielding and hence plastic rotation occur at the load plate face.

5.3.4 Load Case 2.3

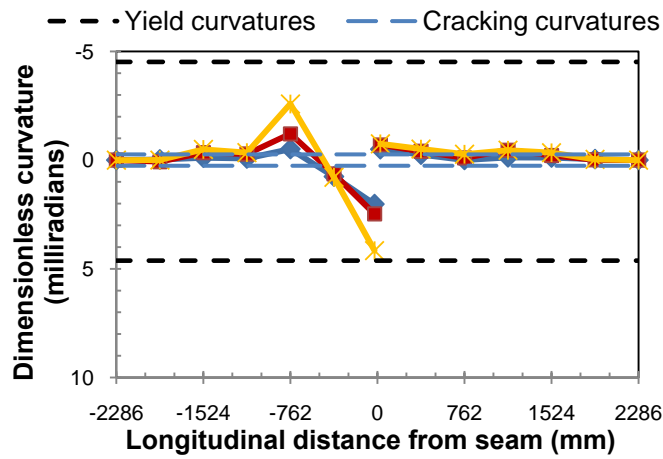
Fig. 46 presents the results for Load Case 2.3, that is for tandem (wheel) axle loads applied 1.22 m apart on a single panel overhang. The resultant displacement profile is given in Fig. 46(a). Failure occurred at 360 kN, hence the result for 356 kN is omitted from the plot for the sake of clarity. The tandem wheel load increased the free end displacement in contrast to Load Cases 1.3, 1.6 and 2.7 where the single wheel load had a small effect on the free end displacement (approximately 2.5 mm). The seam displacements are almost twice that observed for Load Case 1.6, which suggests the steel strain was much greater than yield, as a full flexural failure formed.

Fig. 46(b) supports the concept of a full flexural failure mechanism. Nearby the seam a curvature of magnitude of $2.28\Phi_y$ occurred. There were two other points of interest along the slab at failure. First, the displacement transducer located at -762 mm from the seam had an inferred curvature of $1.14\Phi_y$. Hence the top steel reached yield, as supported by the failure crack pattern. Second, at +1524 mm, near the applied tandem axle (wheel) load, the inferred curvature at incipient failure was approximately $0.9\Phi_y$. Cracks on the soffit of the slab were observed at this point. The calculated failure mechanism, fully supported by the observed crack pattern and the curvatures indicated in Fig. 46(b) are presented later.

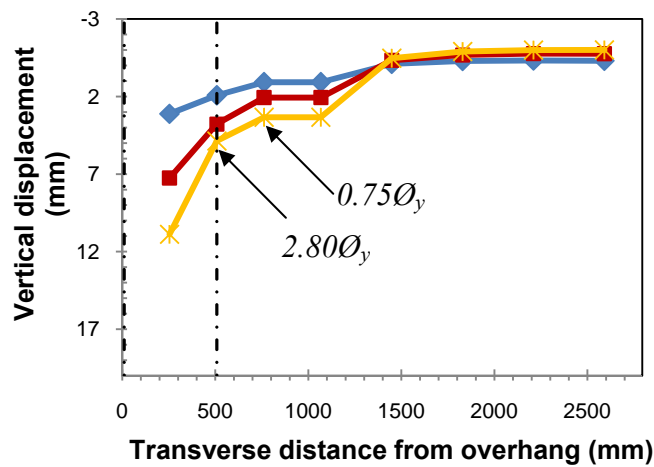
The transverse displacement profile for Load Case 2.3 is plotted in Fig. 46(c). Using finite differences, the inferred curvature at the beam face was $\Phi H = 20.4$ milliradians, or $\Phi = 4.30\Phi_y$. Near failure, the transverse rotation about the beam face appears to be linear along the overhang, supporting the assumed plastic deformed (yield line) shape presented later.



(a) Longitudinal displacement profile

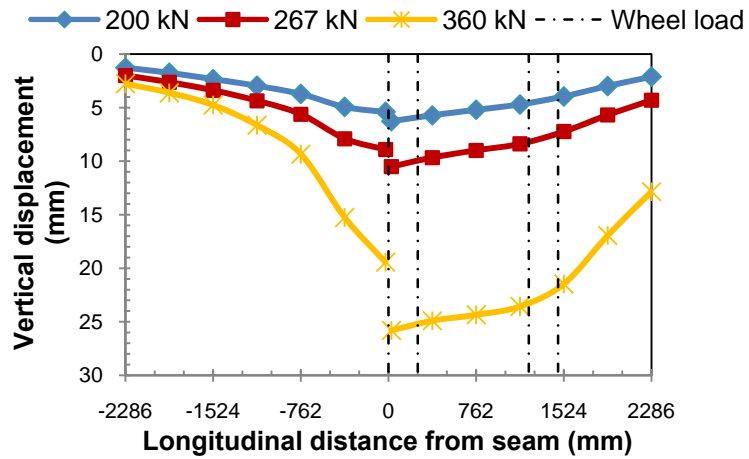


(b) Longitudinal curvature profile

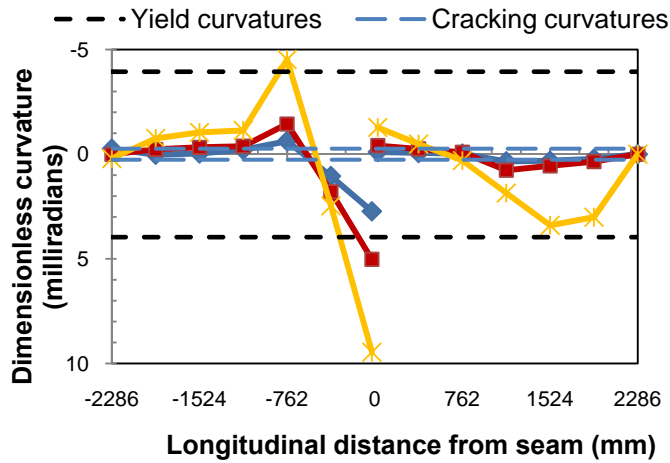


(c) Transverse displacement profile

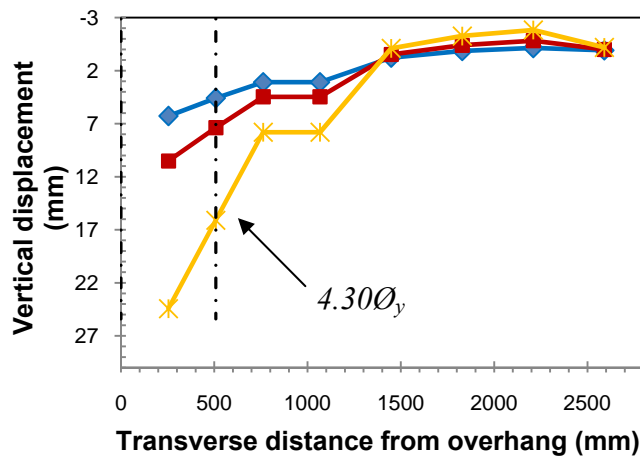
Fig. 45. Load Case 2.7 – lab-cast overhang loaded to failure at 298 kN



(a) Longitudinal displacement profile



(b) Longitudinal curvature profile



(c) Transverse displacement profile

Fig. 46. Load Case 2.3 –precast prestressed overhang, tandem axle load loaded to failure at 360 kN

5.4 Analytical Results

Ultimate moment capacities based on measured material properties for the various deck sections were provided in Table 5 of Section 3.2.4 of this thesis. These values are used in the subsequent analysis. The sectional area of reinforcement per unit width is assumed to be constant across the slab, from which the moment capacity is calculated on a unit width basis. However, this is not the case at the conventional overhang where there are only three #5 bars spaced over 430 mm from the edge of the slab. This steel was lumped over a 500 mm length so that beyond the load plate the positive moment capacity in the longitudinal direction is negligible. Note that the x -direction is taken as transverse to the direction of travel and the y -direction is the longitudinal direction of the bridge.

Using actual material properties, the development length of (1) equates to 435 mm and 390 mm for the #5 (16 mm) reinforcement in the conventional/lab-cast and prestressed-precast overhangs respectively. The development length of deformed wire is governed by the minimum required development length of 305 mm. Based on the comparative analysis techniques discussed and derived for this work, analyses using all of these methods were conducted for failure load cases. Results of this work are provided in Table 10 with the initial cases highlighted by bold font. Collapse loads are given in Table 10 with accuracy ratios (closest theoretical/experimental value) for each analysis method listed in parentheses.

With the exception of the conventional panel that seems inexplicably weak, the analytical models that have been modified herein to more accurately reflect observed behavior, and provide quite satisfactory estimates of the collapse load. Discussions on the analytical methods for each load case are provided in the remainder of this section.

Table 10. Exterior experimental and theoretical failure loads in kN (and experimental/theoretical load ratios)

LOAD CASE	Experimental failure load	Yield line theory	Modified yield line theory	AASHTO punching shear, $\theta = 45^\circ$	Punching shear, $\theta = 38^\circ$	Modified flexural-shear failure
1.3	476	630 (1.33)	526 (1.10)	668 (1.40)	903 (1.90)	-
1.6	374	610 (1.63)	472 (1.26)	396 (1.06)	534 (1.43)	378 (1.01)
2.3	360*	356 (0.99)	338 (0.94)	396 (1.10)	534 (1.48)	481 (1.33)
2.7	302	605 (2.00)	396 (1.31)	396 (1.31)	534 (1.77)	320 (1.06)

*Load applied per "wheel" footprint.

5.4.1 Load Case 1.3

Fig. 47 schematically presents the surface cracks and critical mechanism for Load Case 1.3. Both flexural and punching-shear cases were considered, by which a flexural case was found to be critical. The crack pattern on the bottom of the slab and top surface support the calculated yield lines positions needed to provide the minimum collapse loads. The critical failure load predicted using the modified yield line theory was 556 kN, shown in Fig. 47(b). The ratio of the theoretical capacity to the experimental capacity was 1.10. Negative curvatures (tension on top surface) are small at failure, suggesting that a full plastic hinge line did not fully form in the top steel, as assumed in the yield line theory.

Failure cracks occurred spontaneously where cracks were not previously visible. The moment-curvature analysis supports this brittle failure, where there is a sudden drop off in load carrying capacity once the positive moment is reached. Hence there is an instantaneous redistribution in moments to the negative moment region that cannot be supported causing a sudden failure.

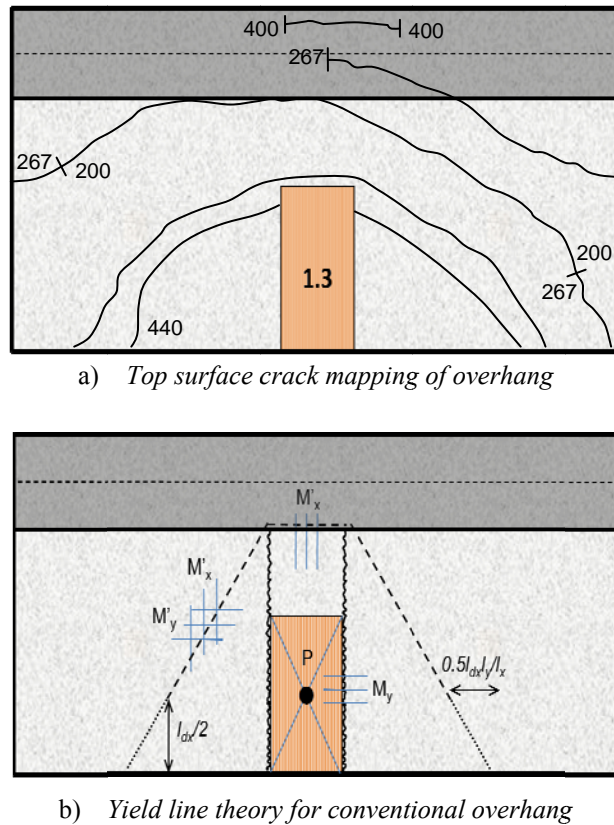


Fig. 47. Load Case 1.3; surface cracks and critical failure mode for conventional overhang

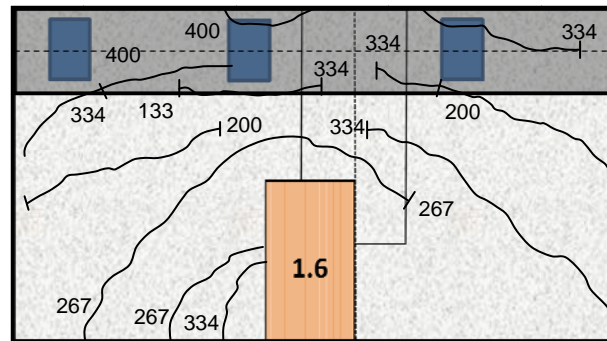
5.4.2 Load Cases 1.6 and 2.7

This subsection deals with the two overhang cases for the precast prestressed panels (Specimen 1, Load Case 1.6), and lab-cast panels (Specimen 2, Load Case 2.7). Fig. 48(a) presents the observed crack pattern for Load Case 1.6 and failure load (374 kN); along with Fig. 48(c) to (d) showing two theoretical load cases considered. The critical theoretical load is a mixed failure mode of shear adjacent to the seam along with flexure (modified for partial bond) elsewhere, as shown in Fig. 48(d). The nature of the failure mode for this solution concurs with the experimental observation. Moreover, good agreement between the theoretical and observed failure capacities should be noted.

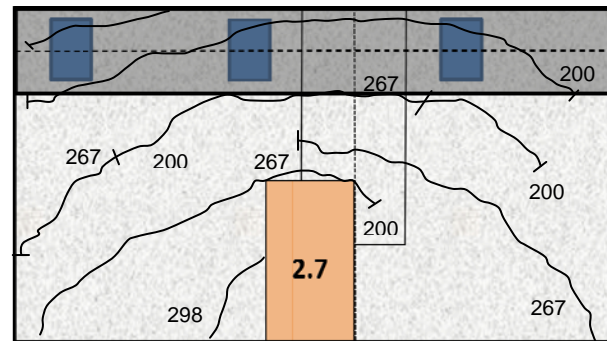
Fig. 48(b) presents the crack patterns for the lab-cast overhang, along with two of the analysis cases considered in Figs. 48(c) and 48(d). Note that the theoretical collapse loads are similar to Load Case 1.6, the difference between the predictions result from the

different steel details and concrete strengths in Specimen 1 and 2. Again, the theoretical results predict a critical mixed flexural-shear failure, as shown in Fig. 48(d). With the predicted failure load being 320 kN compared to the observed failure load of 302 kN.

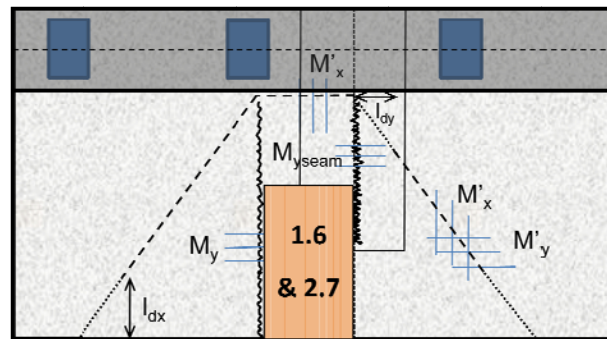
While the lab-cast failure load (302 kN) is some 72 kN lower than the prestressed-precast overhang failure load (374 kN), the reduction of strength cannot solely be attributed to the presence of continuous prestress across the beam to the interior section. One notable difference between the two systems is the positive longitudinal moment capacity, M_y . The prestressed-precast panels in Specimen 1 utilized a welded wire mesh in the longitudinal direction as bottom reinforcement, whereas the lab-cast panels of Specimen 2 had #5 reinforcing (16 mm) running longitudinally as bottom reinforcing. Due to the large development length of the #5 (16 mm) bars in the lab-cast panels (435 mm), and allowing for end cover, the contribution of these bars in the calculation of M_y is neglected. Hence the moment capacity is reduced from 78.5 kNm/m to 20.2 kNm/m. This is the principal contributing factor in the significantly lower failure load. Therefore, the reduced failure load in the lab-cast panels compared to the precast prestressed overhang panels cannot be attributed to the presence of continuous prestress alone. It is considered it would be advisable to use isotropic reinforcement with bars with standard hook lengths at the ends when constructing precast reinforced (non-prestressed) panels to increase the ultimate load capacity.



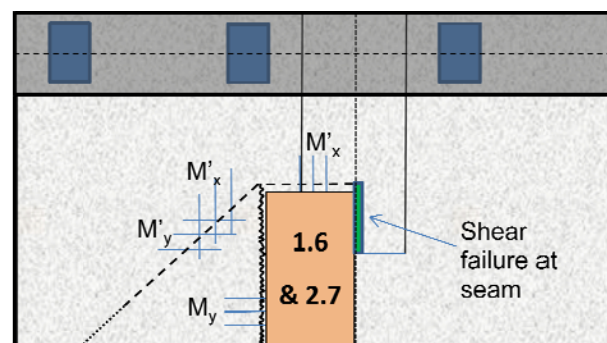
a) *Surface cracks on precast prestressed overhang*



b) *Surface cracks on lab-cast overhang*



c) *Modified yield-line failure mechanism*



d) *Shear-flexure interaction failure mode*

Fig. 48. Surface cracks and credible failure mechanisms for Load Case 1.6 and Load Case 2.7; the precast prestressed overhang and lab-cast overhang, respectively

5.4.3 Load Case 2.3

The surface crack patterns and critical failure mechanism for Load Case 2.3 are presented in Fig. 49. This case was for the tandem axle loads for the precast prestressed overhang in Specimen 2. The observed surface crack patterns are shown in Fig. 49(a) while Fig. 49(b) presents the critical flexural failure mechanism. In contrast to Load Case 1.6, where the prestressed-precast panel was loaded at the seam, the tandem axle (wheel) load caused failure cracks to propagate to the adjacent panel. This suggests that a flexural yield line mechanism was the failure mode, under which moments were redistributed from the loaded panel to the adjacent panel. Further support for a flexural mechanism is based on Fig. 46(b), where curvatures exceed the yield curvature at the seam and also on the adjacent panel.

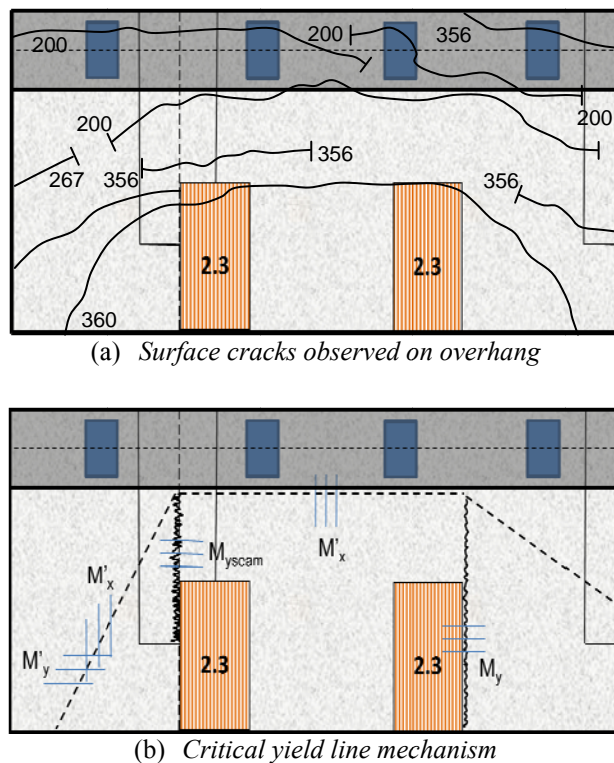


Fig. 49. Load Case 2.3; surface cracks and critical failure mode for precast prestressed overhang with tandem axle load

5.5 Discussion

Analytical predictions supported by observed crack patterns and inferred curvatures imply that the governing mode of failure in concrete bridge deck overhangs is from flexure. Although it is common to assume that bridge decks are shear critical due to their thickness (200 mm), it has been shown for the present study that this is not the case. A tandem axle (wheel) increases the likelihood of a flexural failure due to reduction in concentrated pressures observed with single wheel loads. The yield line analysis on Load Case 2.3 provided good comparison, a 0.99 ratio of theoretical/experimental load. Single patch loads were not as accurate. Accuracy ratios were 1.45, 1.64 and 2.00 of theoretical/experimental load for Load Cases 1.3, 1.6 and 2.7 respectively. However when the yield line theory was modified to account for debonding of bars in the transverse overhang and at the panel-to-panel seam the accuracy ratios improved to 1.16, 1.27 and 1.32 for Load Cases 1.3, 1.6 and 2.7 respectively.

The AASHTO punching shear formula provided a greater accuracy than traditional yield line theory with accuracy ratios of 1.41, 1.06, 1.10 and 1.32 for Load Cases 1.3, 1.6, 2.3 and 2.7 respectively. Although this correlation may be acceptably accurate for Load Cases 1.6 and 2.3, it was evident from the experiments that a shear failure was not the governing mode of failure. The convenience of the results is fortunate, as the punching shear formula does not consider the reduced boundary restraint for overhang slabs, nor the steel ratio in the slab. Beam restraint reduces the ability for the slab to rotate, thus making a shear failure more likely than flexure. The AASHTO punching-shear equation was modified in this research to account for the reduced shear area although it is likely that the restraint would affect the ultimate capacity. Research by Acevedo et al. (2009) and Mufti and Newhook (1998) have shown that clamping stresses and restraint significantly influence the shear capacity of a concrete slab. Also, it has been shown by Fang et al. (1994), Beal (1982), and ASCE-ACI Committee 426 (1974) that the steel ratio governs whether a shear failure or flexural failure will govern.

As per Sections 3.6.1.2.2 and 3.6.1.2.3 of AASHTO LRFD Bridge Design Specifications, the design axle load for an HL-93 Truck and HL-93 Tandem load is 142 kN and 111 kN respectively. Using the most adverse load factors, a HL-93 wheel load is 267 kN at a panel-to-panel joint and 200 kN elsewhere. Similarly, the maximum factored tandem wheel load is 200 kN at a joint and 155 kN on other portions of the deck. All load cases exceeded these demands, implying that the designs are sufficient. However, it is expected that the overhangs are unnecessarily over reinforced due to lack of thorough two-way design of concrete bridge decks. Further supporting this, the applied loads were applied on the edge of the overhang, whereas AASHTO only requires the center of load to be 300 mm from the barrier face. Assuming a barrier width of 300 mm, this positions 100 mm of the wheel load bearing over the girder flange for the smallest AASHTO girder (Type I). Thus the moment at the beam face would be reduced, requiring less reinforcement. Also, the performance of the overhang would be enhanced for both conventional and precast construction if standard hook lengths were used at the bar ends. This would enable full development of the bars, and use of traditional yield line theory, hence higher strength capacity as demonstrated in the analysis.

5.6 Conclusions

Based on the evaluation of the experimental results the following conclusions can be drawn:

1. There is a tendency to assume slab overhangs on bridges arise from cantilever action. This is not the case and a relatively complex two-way slab action results. When precast panels with partial-depth seams are used this complicates matters further, thus slabs should be analyzed and designed accordingly to accommodate these complexities.
2. Yield line theory is a useful way to analyze two-way slab overhangs. However, compared to its normal form it needs two modifications:
 - Reduction in moment capacity near slab edges to account for bond effects.

- Shear effects at panel-to-panel seam.
3. Experimental observations indicated a mixed flexure-shear failure for exterior overhang panels loaded on the seam edge between adjacent panels. Flexural failure using the modified yield line theory occurred on the loaded panel while a shear failure of the seam prevented plastic hinge lines forming on the adjacent panel. This gave accurate predictions of the theoretical failure mode, with accuracy ratios of 1.01 to 1.06 of the theoretical load/experimental value for the applicable cases.
 4. Longitudinal displacement profiles were plotted to show the relative displacement between panels when loading on the edge of the seam between precast panels. This provides a useful indication on the performance of the seam and whether it adequately transfers load to the adjacent panel. Although the relative displacements measured some 5.1 mm at loads of approximately 356 kN for a tandem axle (wheel) load on the overhang, the relative displacement between panels at loads of 200 kN was a mere 1.3 mm. Hence the seam provides sufficient strength transfer under normal loads. Full flexural failure in both the loaded and adjacent panel would need to develop to increase the failure load capacity. This would require an increased shear capacity of the seam, which can be achieved by increasing the depth of the seam to say 150 mm, or by providing a roughened surface or shear key.

CHAPTER VI

ANALYTICAL INVESTIGATION: INTERIOR

6.1 Introduction

Slab behavior is difficult to predict due to complex two-way interaction and simplified analysis techniques do not consider compound failure modes such as a simultaneous compound shear-flexure failure. A mixture between flexural and punching-shear failure was observed in experiments conducted by Graddy et al. (2002). The specimens they constructed did not replicate typical bridge decks; instead they consisted of heavy flexural reinforcement along with relatively large clear cover (65 mm) to the bottom bars to cause punching-shear failure in a 190 mm thick concrete deck. However, in static specimens they noted a punching-shear failure under monotonic loading while delamination occurred at the CIP and SIP panel interface under pulsating fatigue failure in other specimens. Failure loads were observed to be 50% higher than predicted by the punching-shear formulae, Eq. 8-58, from AASHTO LRFD Bridge Design Specifications (2007). In order to modify their predictions the punching shear inputs were changed based on experimental observations. Such an experimental approach cannot be used in routine design of bridge deck slabs; therefore a valid design theory is necessary and proposed herein.

This chapter investigates the failure mechanism of the interior portion of SIP-CIP bridge decks under a monotonic wheel load that is representative of tandem axle effects. Two load cases under consideration are: (1) Load Case 2.4, tandem axle (wheel) loads on a single precast prestressed panel, with one of those wheel loads placed near a panel-to-panel seam; and (2) Load Case 2.8, tandem axles (wheels) straddling two panels, again with one wheel load near a transverse seam. Herein analytical predictions are compared to the experimentally observed results using several different failure theories. The experimental observations, supported by the analytical predictions, suggest that an

interaction between flexure and shear is likely to occur as neither shear nor flexure separately can provide an accurate estimate of load carrying capacity.

The proposed limit failure load is based on a combined punching-shear in the top reinforced concrete CIP portion of the deck while a flexural (of the yield-line type) mode of failure was observed in the lower SIP prestressed panel. This visual observation was also supported from displacement transducer readings from which curvatures were inferred. To this end, a new theory is advanced herein that uses the virtual work approach to capture the effects of the mixed punching-shear and flexure failure modes. The model developed uses an additive approach of combining the punching-shear failure over the top CIP concrete deck with yield line moments over the SIP precast prestressed concrete panels.

6.2 Modes of Failure in Bridge Decks

The following subsections explain the analysis of shear and flexure failure modes for normal full-depth slabs that have been cast as a single monolithic unit. These modes will subsequently be adapted to enable composite SIP-CIP decks to be analyzed in the next main section.

6.2.1 Shear in CIP slabs

Shear is a potential, although not common, mode of failure for reinforced concrete slabs without transverse reinforcement. Shear failure may occur either in thick slabs or when highly concentrated point or patch loads are applied. After diagonal tension cracks have occurred, shear forces are carried through shear in the compression zone, aggregate interlock and dowel action (Park and Gamble, 2000). One-way shear occurs when there are distributed loads or loads close to support lines, where parallel forces in the slab develop. Two-way shear, commonly referred to as punching-shear, is associated with concentrated loads.

AASHTO LRFD Bridge Design Specifications (2007) currently provide guidelines on how to predict the punching-shear capacity associated with a rectangular

footprint in nonprestressed slabs and for slabs prestressed in one direction only. The basis of the general punching shear model derivation is shown in Fig. 50(a) showing the assumed failure planes acting at an angle of θ to the horizontal plane. General punching-shear equation capacity, derived from equilibrium of forces acting on the shear surface may be formed from

$$V_c = 2(b_1 + b_2 + 2d \cot \theta) d \cot \theta f_t \quad (7)$$

$$f_t = \frac{1}{6} \left(1 + \frac{2}{\beta_c} \right) \sqrt{f'_c} \leq \frac{1}{3} \sqrt{f'_c} \quad (8)$$

where V_c = punching-shear capacity in N, b_1 = short side of reaction area in mm, b_2 = long side of reaction area in mm, d = average effective depth of section in mm, θ = acute angle (in degrees) between horizontal and assumed failure plane, f_t = diagonal tensile strength of concrete in MPa, $\beta_c = b_2/b_1$ and f'_c = specified compressive strength of concrete in MPa.

The AASHTO LRFD Bridge Design Specifications (2007) conservatively assumes a crack angle of $\theta = 45^\circ$; thus (7) reduces to:

$$V_c = 2(b_1 + b_2 + 2d) d f_t \quad (9)$$

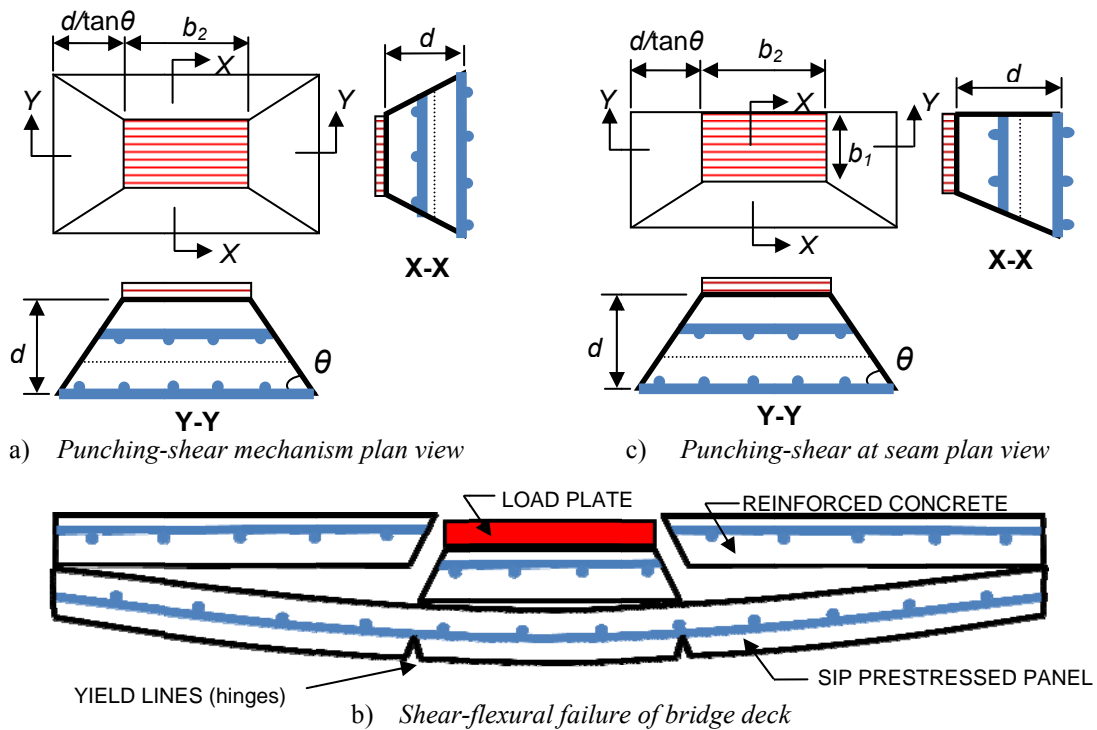


Fig. 50. Shear-flexural failure and punching-shear failure of CIP-SIP bridge deck specimen

6.2.2 Flexure in CIP slabs

Flexural failure is common in thin slabs. For such conditions, yield line theory gives an upper bound limit analysis solution for determining the collapse load capacity of two-way slab systems based on prescribed boundary conditions. Sufficient shear strength is assumed so that a flexural failure mechanism governs. In yield line theory, it is also implicitly assumed that sufficient ductility is available to allow plastic rotation to occur at sections while plastic hinging progressively initiates elsewhere until a complete collapse mechanism develops. In the yield line method of analysis, for a specified admissible yield line mechanism, equations of virtual work are written, unknown dimensions are determined (if any) by energy minimization and the collapse load is calculated. Many admissible mechanisms may exist; it is the mechanism that leads to the *lowest* collapse load via the least amount of work done, which yields is the correct mechanism. Full details of the approach may be found in Park and Gamble (2000). Yield

line theory has been applied to the experimental test conditions for the different sub-tests investigated in this research.

6.2.3 Membrane action

Compression membrane action is considered to be a common failure mode in thick slabs with rigid boundary conditions (Park and Gamble (2000), Graddy et al. (2002), Zheng et al. (2008)). Due to second-order geometric effects and boundary conditions in the slab, compression membrane behavior can lead to higher post-mechanism resistance. Thus compression membrane behavior leads to even higher ultimate failure loads of the slab. The inclusion of membrane forces in yield line theory requires additional force and moment boundary restraints to be included in the internal work equations. These forces depend on how well the slab is supported and bounded, requiring additional assumptions to be made. For the membrane solution to work, substantial displacements at failure are also needed.

6.3 Compound Shear-Flexure Failure Mode in SIP-CIP Decks

AASHTO LRFD Bridge Design Specifications (2007) do not provide specific design guidelines for SIP-CIP bridge decks. Empirical methods are not permitted for design purposes where SIP panels are used, requiring a new design methodology to be set forth. In light of experimentally observed failure modes of Load Case 2.4 and Load Case 2.8, a main focus of this research is to propose a compound shear-flexure failure theory to explain and predict failure loads of CIP-SIP composite bridge decks. Fig. 50(b) presents a transverse cross-section across a bridge deck between two support beams showing the combined mixed punching-shear plus flexure failure mode. Delamination is assumed in the model between the CIP and SIP panels, as was also observed in experiments at the longitudinal ends of the deck during loading. To analyze the collapse load, a simple additive series model combining punching-shear in the upper CIP reinforced concrete portion of the deck, plus the flexure capacity provided by the lower precast prestressed panel was derived.

$$P_u = V_c + P_f \quad (10)$$

where P_u = ultimate failure load; V_c = shear component in the upper CIP reinforced concrete; and P_f = flexural component of lower SIP prestressed concrete panels.

6.3.1 Shear at a panel-to-panel seam

Fig. 50(c) presents a mixed punching-shear failure mechanism at the joint (seam) of a bridge deck constructed from series of SIP precast panels topped with CIP reinforced concrete. The loaded panel fails in punching-shear over the full depth, but the adjacent panel only over the top 100 mm CIP deck. This is a consequence of discontinuous bottom longitudinal reinforcement between the SIP precast panels at the panel-to-panel seam. For two-way shear at the seam, it is necessary to modify the length over which the shear-area acts. Note that it is assumed that $d' = 100$ mm, the full depth of the CIP deck in following analyses:

$$V_c = (2b_1 + b_2 + 2d \cot \theta) d \cot \theta f_t + (b_2 + d' \cot \theta) d' \cot \theta f_t \quad (11)$$

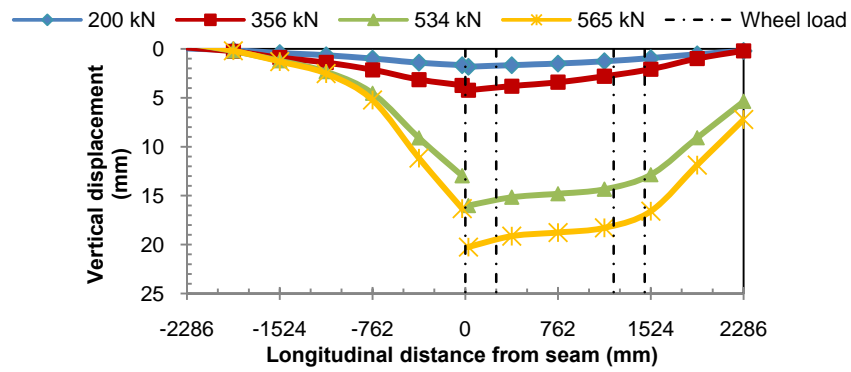
Based on a series of tests, a value of $\theta = 38^\circ$ was suggested by Graddy et al. (2002) for their calculated punching-shear capacities for SIP-CIP concrete bridge decks. This value was used in subsequent analysis when specified to determine the accuracy and validity of the assumption of a 38° crack angle proposed by Graddy et al. (2002).

6.4 Experimental Displacement Profiles and Inferred Curvatures

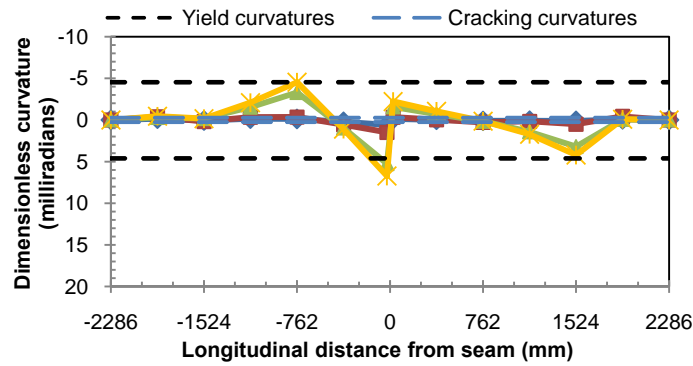
As the full nonlinear behavior of cracked reinforced or prestressed concrete slabs is difficult to predict due to complex two-way interaction, it is instructive to first examine the experimental deformation patterns observed during testing. This sub-section provides experimental results for two sub tests, where curvatures will be inferred: Load Case 2.4 and Load Case 2.8. Both load cases simulate a dual axle (wheel) load with load plates

spaced at 1.22 m. Load Case 2.4 has both wheels on a single SIP panel, with one wheel on the SIP panel-to-panel seam edge. Load Case 2.8 straddles the seam between SIP panels, again with one wheel on the SIP panel-to-panel seam edge.

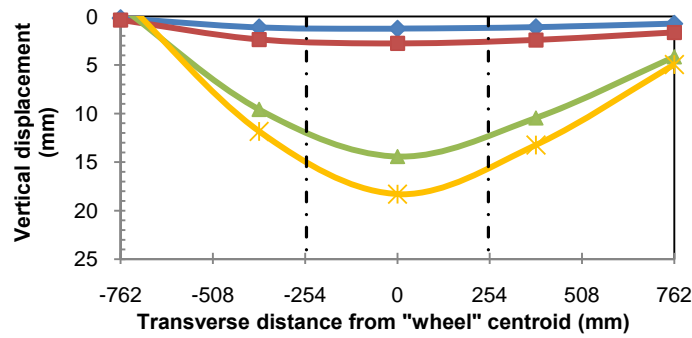
Based on measured deflection profiles, curvatures are inferred using a finite difference technique set forth in Appendix II. Figs. 51 and 52 show displacements and curvatures for Load Cases 2.4 and 2.8, respectively. Plotted in graphs (a) and (c) of those Figs., respectively, are longitudinal and transverse displacement profiles at loads measured prior to failure, which occurred at 565 kN and 667 kN respectively. From the displacement profiles, corresponding curvatures were calculated using the finite differences solutions given in the Appendix. Graphs (b) and (d) of Figs. 51 and 52 show the plots of the longitudinal and transverse profiles respectively. Calculated cracking and yield curvatures are also shown in these graphs. From the experiments conducted, it is desirable to have knowledge of the strains in the steel reinforcement at failure and the loads required to cause first yield. Examination of these results provides a better understanding of the performance of the seam between panels. Specifically, the effectiveness of redistributing load to the adjacent panel and observing the relative difference in vertical deflection between the two panels is of interest.



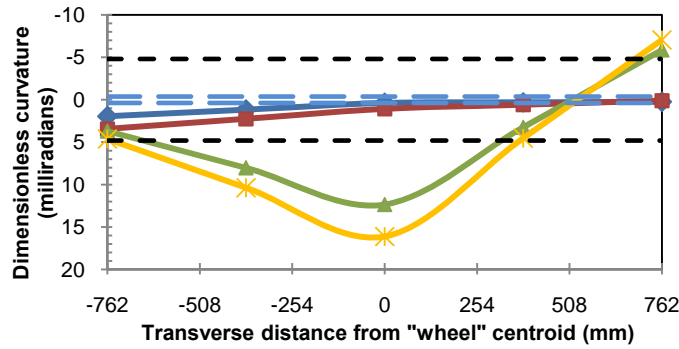
(a) Longitudinal displacement profile



(b) Longitudinal curvature profile

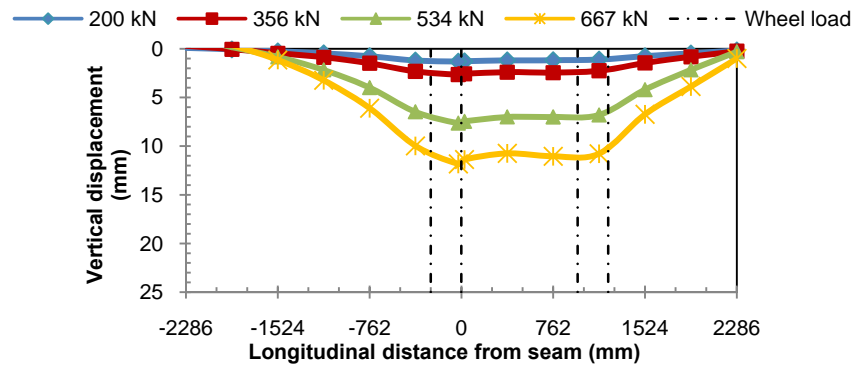


(c) Transverse displacement profile

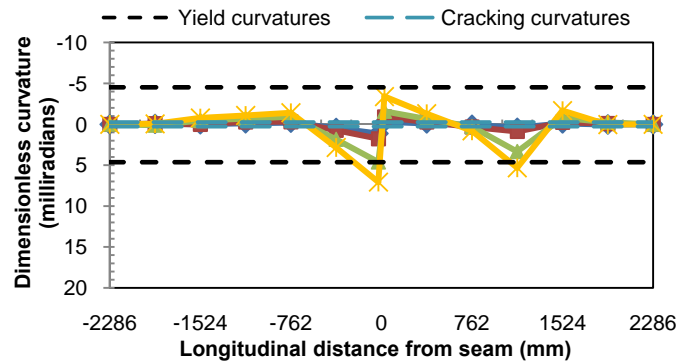


(d) Transverse curvature profile

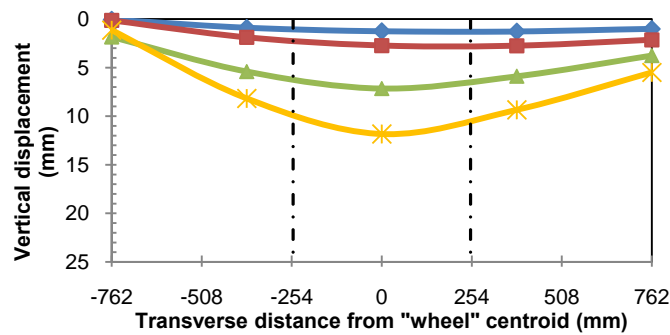
Fig. 51. Load Case 2.4 – tandem axle (wheel) load on single panel, loaded to failure at 565 kN



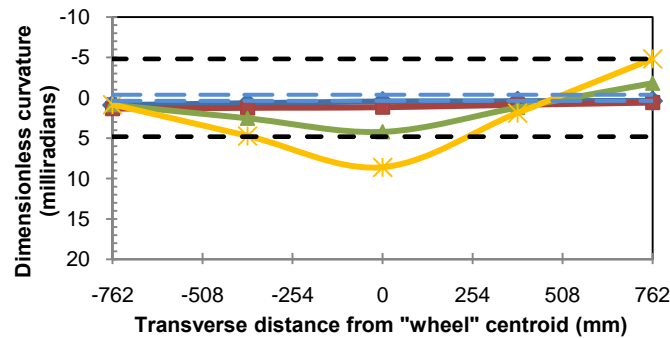
(a) Longitudinal displacement profile



(b) Longitudinal curvature profile



(c) Transverse displacement profile



(d) Transverse curvature profile

Fig. 52. Load Case 2.8 – tandem axle (wheel) load straddling seam, loaded to failure at 667 kN

6.4.1 Load Case 2.4

From the longitudinal results (Fig. 51(a) and 51(b)), it is evident that the slab remained essentially uncracked with a smooth transition over the deck joint for loads up to 356 kN. However, when the load exceeded the yield curvature at the panel seam at a load of 525 kN, substantial cracking propagated, with a marked reduction in stiffness. At a load of 534 kN (which is twice the maximum factored AASHTO LRFD (2007) design load), the displacement across the deck-joint seam indicated a 3 to 5 mm discontinuity. At a failure load of 565 kN the adjacent panel reached the negative yielding curvature capacity. Incipient failure occurred adjacent to the seam when the maximum inferred curvature was $1.40\Phi_y$, where Φ_y = calculated yield curvature.

Transverse displacement profiles for Load Case 2.4 are plotted in Fig. 51(c) with curvatures in Fig. 51(d). Although it appears in Fig. 51(c) that substantial bending in the load plate occurred at 565 kN, the difference in deflection between the edge and center of the plate is only some 2.5 mm. From the recorded data it was inferred that transverse yield occurred at 467 kN. This is lower than the yield force of 534 kN observed in the longitudinal bridge axis. Cracks were first observed on the bridge deck at a load of 476 kN, at which the transverse yield curvature capacity was exceeded.

6.4.2 Load Case 2.8

Fig. 52 presents the longitudinal and transverse displacement and curvature results for Load Case 2.8. At a load of 534 kN the seam displacement was approximately 7 mm, less than half of the 16 mm observed for Load Case 2.4. The relative displacement between the two panels was negligible, with vertical displacements similar at both load plates. First yield was achieved at 534 kN; a similar value is noted from Load Case 2.4 as shown in Fig. 52(b). The final failure curvature was $1.45\Phi_y$ at the seam and $1.2\Phi_y$ at the tandem axle (wheel) load.

Transverse displacement and curvature profiles are provided, respectively, in Fig. 52(c) and (d). Few transverse surface cracks were observed during the experiment. However, the most notable crack occurred at 667 kN across the beam face when the yield curvature was reached. Fig. 52(d) infers transverse reinforcement under the wheel

load reached yield at 534 kN. The maximum soffit curvature at the deck soffit was $1.80\Phi_y$, with yielding occurring at the edge of the load plate. This data is valuable in assessing the collapse load for which the proposed compound shear-flexure theory is utilized in the following section.

6.5 Results of Collapse Load Analysis

Based on a maximum concrete compressive strain along with measured concrete cylinder strengths and steel yield stresses, ultimate moment capacities for the various deck sections were calculated (Chapter IV). Note that the x -direction is taken as transverse to the bridge axis and the y -direction is the longitudinal direction (direction of traffic) of the axis of the bridge. Table 11 presents the experimentally observed failure loads along with the theoretical mechanism capacities.

Results from yield line theory alone generally show excessively high estimates of the collapse loads compared to the observed results. AASHTO LRFD (2007) punching-shear results are overly conservative, with the failure load being up to 1.5 times greater than the predicted load. For this research, no increase in diagonal tensile strength was considered due to the effects of prestressing. The critical failure mode (shear-flexure) results are highlighted in bold font of Table 11. The analytical collapse models that have been proposed herein evidently reflect observed behavior more accurately and provide quite satisfactory estimates of the collapse load. Discussions on the analytical methods for each load case follow.

Table 11. Interior experimental and theoretical failure loads in kN (and theoretical/experimental load ratios)

LOAD CASE	Experiment failure load	Full-depth yield line theory	AASHTO punching-shear ($\theta = 45^\circ$)	Punching-shear ($\theta = 38^\circ$)	V_c , CIP deck punching-shear ($\theta = 45^\circ$)	P_t , SIP panel yield line	Shear-flexural failure
2.4	565*	1233 (2.18)	445 (0.79)	605 (1.07)	365	213	578 (1.02)
2.8	667*	1451 (2.18)	445 (0.67)	605 (0.91)	365	289	654 (0.98)

*Load applied per "wheel" footprint.

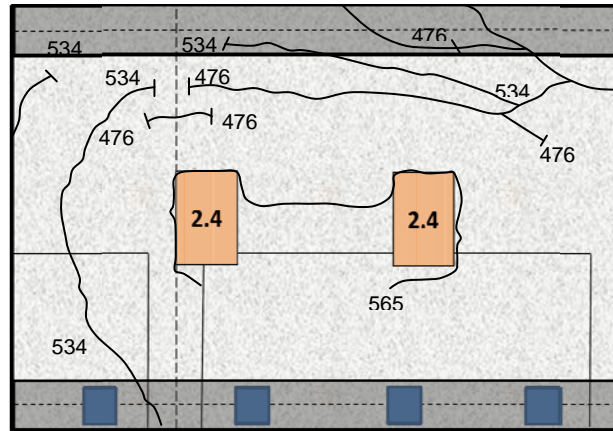
6.5.1 Load Case 2.4

Figs. 4(a) to (c) present the observed crack pattern and analyzed failure mechanisms for Load Case 2.4. The experimentally observed crack pattern is shown in Fig. 53(a) for which top surface cracks are mapped. The associated three-digit numbers presenting the load in kN show the extent of cracking at that load. These cracks are indicative of the negative moment yield lines. Safety requirements restricted access beneath the deck and careful mapping of the cracks. However, visual observations on top of the deck corroborated the predictive yield lines shown in Fig. 53(b).

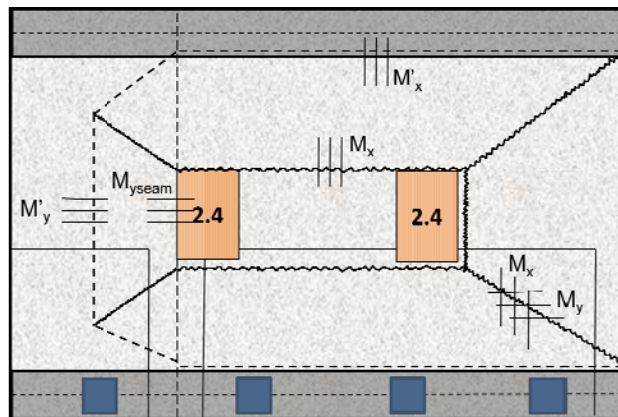
Traditional yield line analysis was first used to determine the failure mechanism. Fig. 53(b) shows the theoretical yield line for the lowest collapse load. Positive moments (compression on top surface, or tensile cracks on the soffit) are drawn in jagged solid lines while negative moments (tension cracks on top surface) are drawn in dashed lines. The mechanism drawn in Fig. 53(b) had the lowest failure load for yield line analysis. However, the experimental failure load of 565 kN is only 46 percent of the analytical failure load of 1233 kN. This excessive (unsafe) over-estimate of capacity is largely due to the unrealistically high pressures beneath the load plate which prevented a full flexure mechanism from forming. Also, the analysis assumed a full-depth negative moment was present throughout as shown. However, at the interior beam there was no negative moment resistance as the panels terminate at the seat and behave in a simply-supported fashion. This modification is made to the analysis when considering a mixed shear-flexural failure mechanism.

The critical (lowest) interior failure for Load Case 2.4 involved the additive analysis of the proposed shear-flexure mechanism, illustrated in Fig. 53(c). Due to delamination between the two layers, the Stage I section of the precast prestressed panels developed a flexural failure while the top CIP deck failed in punching-shear. Punching-shear occurred over the top 100 mm CIP deck with flexural failure of the bottom panels as illustrated in Fig. 53(c). The section moment capacities used are those for the SIP panels alone. The experimental failure load of 565 kN is 98 percent of the theoretical

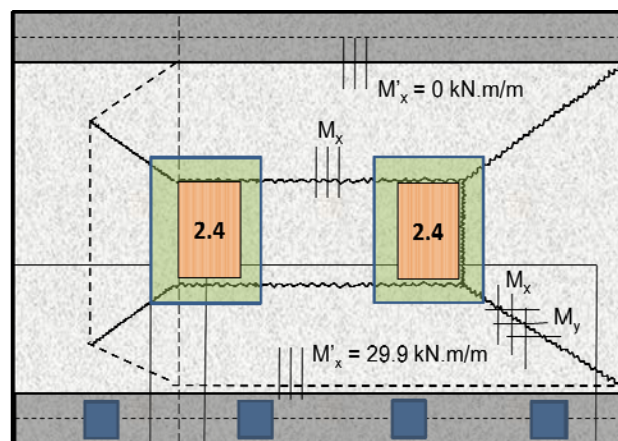
failure load using shear-flexural failure theory of 578 kN. The results of the proposed compound theory compares well with the experimentally observed failure mechanism.



(a) Surface cracks observed on prestressed-precaster interior, loaded to failure at 565 kN



(b) Yield line theory: 1233 kN



(c) Shear-flexure interaction: 578 kN

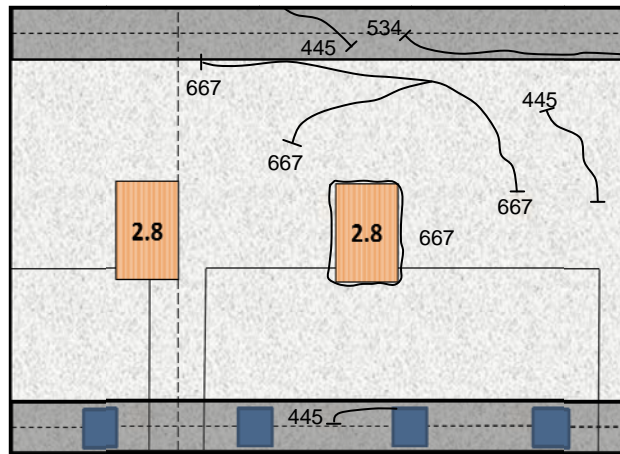
Fig. 53. Load Case 2.4; credible failure modes for tandem axle (wheel) load on single panel

6.5.2 Load Case 2.8

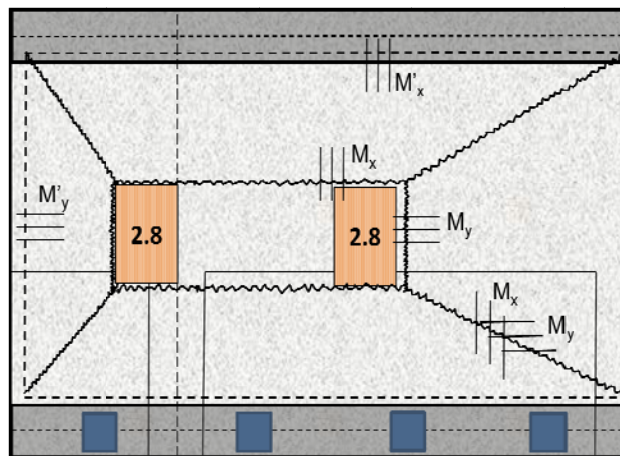
Figs. 54(a) to (c) presents the experimental observations and theoretical solutions for Load Case 2.8. Fig. 54(a) presents the observed experimental surface cracks. Similar to Fig. 53(a), surface cracks were mapped when they became apparent. Notable cracking did not appear around the load plate until the failure load of 667 kN occurred. This observed load is 50 percent greater than the computed AASHTO punching shear capacity of 445 kN, at which large cracks would be fully formed. The accurate mapping of soffit cracks was prevented due to safety precautions but the observed cracks following the experiment are related to those of Fig. 54(c).

Fig. 54(b) illustrates the critical yield line mechanism to allow for the load plate straddling the transverse seam. The experimental failure load of 667 kN is only 46 percent of the predicted capacity of 1451 kN by yield line theory. It is evident that Load Case 2.8, the tandem wheel straddling a seam, leads to higher capacity both theoretically (with yield line theory) and experimentally than when loading a single panel (Load Case 2.4). Table 11 shows that this is not the case for punching-shear analyses which provide the same results for both Load Case 2.4 and Load Case 2.8 as the local boundary conditions are the same. Similar to Load Case 2.4, a full flexural mechanism was unable to form due to the high pressures observed beneath the load plate, changing the failure mechanism in the CIP portion of the depth from flexure to shear.

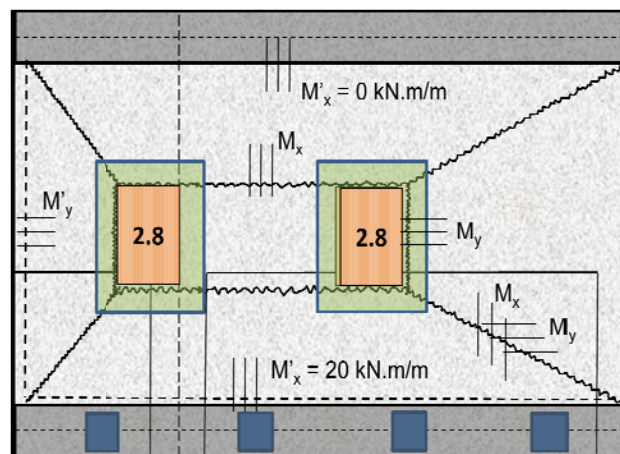
Punching-shear is assumed to occur over the CIP deck with the addition of positive flexure moments occurring in the SIP panel. The theoretical failure mode of 654 kN compares favorably to the experimental failure load of 667 kN per load plate. In contrast to the precast prestressed side, the negative moment on the SIP panel was not included as the panel was simply-supported between beams. However, mild steel was welded on to the tendon strand ends to provide some positive moment capacity for lifting purposes. Theoretical loads will increase if arching action is considered. However, the current analysis provides a conservative, yet suitably accurate prediction of the experimental failure load.



(a) Surface cracks observed on prestressed-precaster interior, loaded to failure at 667 kN



(b) Yield line theory: 1451 kN



(c) Shear-flexure interaction: 654 kN

Fig. 54. Load Case 2.8; credible failure modes for tandem axle (wheel) load straddling seam

6.6 Discussion

Historically it has been customary practice to carry out physical testing of bridge deck slabs representing the load applied by a set of dual rubber tire wheel loads via a 250 x 500 mm steel plate as per AASHTO LRFD Bridge Design Specifications (2007). But such a representation significantly above normal factored loads leads to unrealistically high implied tire pressures at failure which would be strictly excessive and unattainable. High interior failure loads caused bearing pressures beneath the load plate to reach 5200 kPa for Load Case 2.8. Truck tire pressures rarely would exceed 820 kPa (120 psi). Therefore, to mimic such a pressure including a load and impact factor, a pressure of 1700 kPa would seem a reasonable limit for testing. Thus obtaining a shear failure mode in a bridge structure is unlikely. Using larger load plates to reduce the unrealistic pressures observed on the bridge deck, which reached some 5200 kPa, punching-shear would be prevented and a full flexural mechanism would develop. A 400 x 800 mm load plate would be more in keeping to physically examine realistic failure mechanisms in lieu of using the customary 250 x 500 mm load plate specified by AASHTO LRFD Bridge Design Specifications (2007). Consequently, the tests tend to unrealistically change the failure mechanism from a flexural failure to a partial shear failure.

As observed in both load cases, yield line theory provided an excessive estimate of the slab deck capacity. This is due to both the length of yield lines that are required to form a plastic hinge line along with the high moment capacities due to a relatively moderate steel ratio (~1%) coupled with a large lever arm between top and bottom steel. A yield line solution would only be admissible had the deck slab been solely CIP, eliminating the adverse affect of delamination between the CIP pour and SIP panels. However, yield line theory did agree with experimental results that tandem axle loads straddling the seam (Load Case 2.8) have a higher failure load compared to loading a single panel (Load Case 2.4). It is evident that increasing the flexural capacity of the slab due to membrane action is unnecessary as the prediction using yield line theory is already excessively high compared to the observed experimental failure load. The displacements were small enough so compressive membrane effects were not observed.

Membrane action was conservatively ignored, which is appropriate given the excessively high yield line failure load predictions.

The AASHTO LRFD (2007) punching-shear formula underestimated the deck-slab capacity by some 20 to 25% for Load Cases 2.4 and 2.8, respectively. The predicted failure load for the two load cases was identical as the standard punching-shear equation does not wholly consider boundary conditions. The placement of the wheel load affects the yield-line mechanism formed. This changes the theoretical failure load, thus requiring the proposed shear-flexure theory to be used. The punching-shear capacity is partially dependent on the tensile strength of the concrete, however, using a well-graded coarse aggregate will increase the tensile strength more than it does compressive strength (Mindess et al., 2003). Additionally, it has been shown by ASCE-ACI Committee 426 (1974), Lybas et al. (1990) and Fang et al. (1994) that the reinforcement ratio increases the punching-shear capacity of concrete slabs. The AASHTO LRFD (2007) punching-shear equation does not consider either of these factors.

ASCE-ACI Committee 426 (1974) reported research on the punching-shear strength of a reinforced concrete slab-column connection with an axial column load. The boundary conditions were similar to the precast bridge deck experiments with an axial wheel load applied. The experimental results showed yielding of slab reinforcement at low steel ratios across slab boundaries with a ductile flexural failure mechanism occurring. Conversely, at higher reinforcement ratios punching-shear failure occurred with some general yielding seen at slab boundaries. Based on 20 experiments, an idealized theory showed that the axial failure load increased linearly from zero for slab steel ratios up to 0.85% to a value V_{ult} . After this range punching-shear failure governed with the failure load, V_{ult} , remaining the critical load. Experimental loads were higher than the best-fit punching-shear values in most cases, particularly for steel ratios in the vicinity of 0.85 to 1.2%. This suggests that a combined shear-flexural failure is likely to occur when moderate steel ratios exist such as in the research presented in this paper. Similar results were shown by Fang et al. (1994), who also revealed an increase in reinforcement ratio increases the shear capacity of the section.

6.7 Conclusions

Based on the evaluation of the experimental results along with companion analyses the following conclusions can be drawn:

1. A compound shear-flexural mechanism theory was proposed to explain failures observed in dual reinforced-prestressed concrete bridge decks. Code-based shear and flexural theories cannot provide an accurate estimate alone for thick concrete deck slabs constructed in two layers as SIP-CIP. Rather an additive shear-flexural model is needed, as proposed in this paper and validated from the experimental test results. An estimation of the punching-shear failure for the upper CIP reinforced concrete portion and a flexure failure of the bottom SIP precast prestressed panel gave a satisfactory prediction of the failure load within 2% accuracy.
2. Longitudinal displacement profiles were plotted to show the relative displacement between panels when loading on the edge of the seam between precast panels. This provides useful indication on the performance of the seam and whether it adequately transfers load to the adjacent panel. Although the relative displacements between panels measured some 5 mm at loads of approximately 356 kN for a tandem axle load, the relative displacement between panels at loads of 200 kN was less than 1 mm. Hence the half-depth reinforced seam over adjacent panels provides sufficient strength transfer under normal (factored) loads.
3. Finite difference solutions were developed to enable critical curvatures to be established based on measured displacements. This was not entirely successful due to a relatively sparse number of displacement transducers. It is recommended for future experiments of a similar nature that displacement transducers are spaced evenly at an interval of no more than one panel thickness (200 mm) apart.
4. Although the precast experimental tests on the interior bays of a slab-on-girder bridge constructed with precast prestressed deck panels with a reinforced concrete topping revealed a mixed shear-flexure failure mode, such a scenario is unlikely to occur in reality. This is because, even when allowing for factored load effects, the unrealistically high test pressures observed beneath the load plate per AASHTO

LRFD Bridge Design Specifications (2007) cannot be achieved with rubber tire equipment. However, the proposed theory can be used to estimate the capacity and aid in improved design and efficiency of SIP-CIP composite bridge decks.

CHAPTER VII

CONCLUSIONS

7.1 Summary

With the purpose of validating newly proposed full-depth precast prestressed bridge deck overhang panels, two full-scale concrete bridge deck specimens were constructed and experimentally tested. Each specimen consisted of two overhangs and two interior bays, and of sufficient length to place two full-depth precast prestressed overhang panels adjacent to one another. Specimen 1 provided a comparison in performance between a conventional cast-in-place (CIP) overhang slab and the proposed full-depth precast prestressed overhang. Specimen 2 consisted of the proposed full-depth precast prestressed overhang and a similarly constructed “lab-cast” overhang. AASHTO LRFD Bridge Design Specifications (2007) loads were applied at overhangs followed by failure loads on overhangs and interior bays. Results showed that all overhang specimens had negligibly small displacements, of some 0.4 mm, when loading to the maximum factored AASHTO LRFD (2007) load of 267 kN.

Failure loads on the overhang were made critical by moving the load plate to the free edge of the overhang. On the precast overhangs the load plate was placed on the edge of a panel-to-panel seam to characterize the panel-to-panel seam strength. On Specimen 1 the precast prestressed overhang (Load Case 1.6) failed at 374 kN, a factor of 1.40 times greater than the maximum factored AASHTO LRFD (2007) load. Flexural failure occurred on the loaded panel, with a shear failure occurring at the partial-depth panel-to-panel seam. A similar failure occurred on Load Case 2.7, the lab-cast overhang of Specimen 2, at a load of 302 kN. Load Case 1.3, the conventional overhang of Specimen 1, failed at 476 kN, a load 21 percent greater than Load Case 1.6. This difference was explained through the derivation of a new flexural-shear theory for precast overhangs with panel-to-panel seams.

A modified yield line analysis theory was developed to account for the partial debonding of the reinforcing steel at the overhang and panel-to-panel seam. Modifying the internal work equation to account for a shear failure at the panel-to-panel seam, the modified yield line theory was used to analyze Load Cases 1.6 and 2.7 with, respectively, 0.99 and 0.94 experimental to theoretical load ratio accuracies. Traditional yield line theory had poor accuracy with experimental to theoretical load ratios of 0.61 and 0.50 for Load Cases 1.6 and 2.7 respectively. Thus it is evident that modifying the current form of yield line theory to allow for partially developed reinforcing bars on bridge deck overhangs can assist in optimizing reinforcing steel layouts.

Interior load cases were made critical by monotonically loading a trailing axle load at a panel-to-panel seam. Load Case 2.4 had both load plates placed on a single panel at the edge of the panel-to-panel seam while Load Case 2.8 straddled the seam over two panels. The failure loads were a factor of 2.83 and 3.34 greater than the maximum factored AASHTO LRFD (2007) design tandem load of 200 kN. The excessive reserve capacity was attributed to the inability of code-based shear and flexure theories to accurately predict the failure load of concrete bridge deck slabs constructed in two layers. A compound shear-flexural mechanism theory was proposed to explain failures observed in dual reinforced-prestressed concrete bridge decks. An estimation of the punching-shear failure for the upper CIP reinforced concrete portion and a flexure failure of the bottom SIP precast prestressed panel gave a satisfactory prediction of the failure load within 2 percent accuracy.

7.2 Design Considerations

Based on experimental and analytical findings presented in this thesis and summarized in Section 8.1, the following design recommendations for concrete bridge decks are offered to researchers and practitioners:

1. The steel in conventional overhang concrete bridge decks can be optimized through the use of modified yield line theory. The debonding of steel reinforcing bars should be accounted for, providing an accurate prediction of the ultimate

failure mode. Empirical steel ratios set out in Section 9.7.2.5 of AASHTO LRFD (2007) should be used, which is approximately half of that used in the experimental work of this thesis. Sufficient strength will be available in a conventional 915 mm wide bridge deck overhang for all AASHTO girder types.

2. Standard hooks should be used on the end of transverse reinforcing steel at the concrete bridge deck overhangs. This recommendation applies to both precast overhangs and conventional CIP overhangs. In addition to this, longitudinal steel terminating at panel-to-panel seams in precast overhangs should use standard hooks. Thus traditional yield line theory can be used rather than modified yield line theory as bars are able to yield completely along their length. Based on the analyses performed in this thesis using traditional and modified yield line theory, providing standard hooks will increase the load carrying capacity of the overhang sections by some 15 to 25%.
3. Section 9.7.2.6 of AASHTO LRFD Bridge Design Specifications (2007) does not permit the use of empirical design with SIP concrete formwork. This is due to current design codes not providing an analysis method for SIP-CIP concrete bridge decks. A proposed compound shear-flexure theory provided in this thesis for analyzing SIP-CIP interior bridge deck spans can aid in optimizing the steel layout. Use of the empirical formula for top reinforcing in Section 9.7.2.5 of AASHTO LRFD (2007) is therefore expected to have sufficient capacity under the maximum factored AASHTO LRFD (2007) load.
4. Composite pockets in the proposed precast prestressed overhang panel measured 250 x 180 mm. Pockets were reduced to 150 x 150 mm for the lab-cast panels constructed and presented in this thesis. This is recommended for future construction of precast prestressed overhang panels. In the Stage I pour, the pockets should then be positioned between the prestressing strands, not requiring them to be gas-cut out where they intersect pockets. Similarly, reinforcing in the Stage II pour could be placed at the standard 150 mm spacing. Sufficient space was available in the lab-cast 150 mm square pockets to place two 25 mm

diameter threaded rods in each pocket. Where more connectors are needed in areas of high shear more than three pockets should be used. With pockets positioned between prestressing strands no adverse strength or durability affects are expected when using more than three pockets.

5. In all experiments a 250 x 500 mm steel plate as per AASHTO LRFD Bridge Design Specifications (2007). High interior failure loads caused bearing pressures beneath the load plate to reach 5200 kPa for Load Case 2.8. Truck tire pressures rarely would exceed 820 kPa (120 psi). Therefore, to mimic such a pressure including a load and impact factor, a pressure of 1700 kPa would seem a reasonable limit for testing.

7.3 Recommendations for Future Work

The research of this thesis provided a structural evaluation of a full-depth precast concrete bridge deck system. Specifically increasing monotonic loads were applied to critical sections of the precast deck to identify failure modes and validate AASHTO LRFD (2007) strength requirements. Further research listed below would further validate the system, but were outside of the scope of the work performed in this thesis.

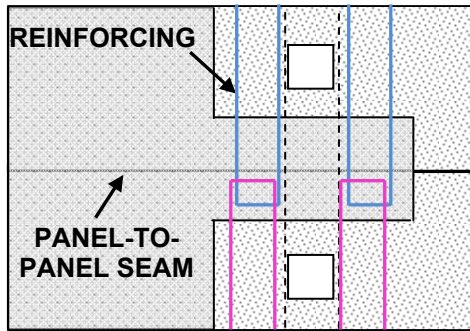
1. The use of minimum isotropic steel as per the empirical design method of AASHTO LRFD (2007) should be evaluated. Thus experiments similar to those conducted in this work should be conducted, to validate the design theory and the efficacy of using minimal reinforcement instead of the reinforcement layout that was examined in this thesis.
2. Quasi-static experiments on full-scale panels that are seated on simply supported prestressed concrete girders should be performed. Under this loading, true field conditions are therefore replicated, and the degree of composite action between the girder and slab via composite pockets can be determined.
3. Highway bridges are subjected to millions of loading cycles during their service lifetime. For this reason it would be advisable to perform fatigue experiments on

the full-depth precast concrete bridge deck system. In particular the fatigue strength of a panel-to-panel seam would be of interest.

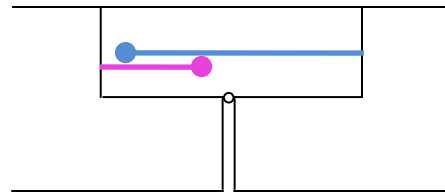
4. Crash barrier and impact loading on the full-depth precast overhang system should be investigated. Although the barrier strength was not investigated in this thesis it is expected that it would perform satisfactorily as the construction is identical to conventional overhang construction.

Additionally, during construction of the experimental specimens, a number of design issues were identified, particularly with the panel-to-panel seam connection at the overhang. Significant time was required to install the C-shaped reinforcing that connected adjacent panels. For this reason it would be advisable to experimentally test two alternative solutions:

5. Hooped transverse reinforcing extending from the Stage II reinforced concrete pour beyond the edge of the panel. The reinforcement would extend approximately 175 mm beyond the edge of the panel, thereby overlapping the adjacent panel reinforcing. Such detail is common in seismic design of reinforced concrete structures, requiring no additional link bars to connect adjacent panels, as shown in Fig. 55(a). This idea could be further extended by having a full-depth overhang along one edge of the precast panel, as drawn in Fig. 55(b). The steel would extend from the overhang in the same fashion into the partial depth seam on the adjacent panel.
6. To eliminate the need for steel placement or special detailing of steel, a full-depth panel-to-panel shear connection should be investigated. This could be similar to the female-to-female shear connections described in detail in Chapter II of this thesis.

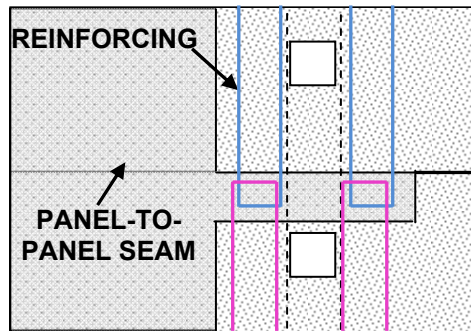


PLAN VIEW
PANEL-TO-PANEL SEAM

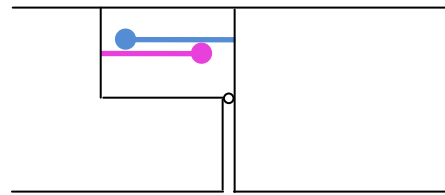


SIDE ELEVATION
PANEL-TO-PANEL SEAM

(a) *Extend reinforcing from Stage II to adjacent panel*



PLAN VIEW
PANEL-TO-PANEL SEAM



SIDE ELEVATION
PANEL-TO-PANEL SEAM

(b) *One full-depth edge per panel with extended reinforcing*

Fig. 55. Schematic of potential improved panel-to-panel connections

REFERENCES

- ACI Committee 318, (2008). *Building code requirements for structural concrete (ACI 318-08) and commentary (ACI 318R-08)*, Farmington Hills, Michigan.
- American Association of State Highway and Transportation Officials (AASHTO). (2007). "Load and Resistance Factor Design (LRFD)." *Bridge design specifications*. 4th Edition, Washington, D.C.
- ASCE-ACI Committee 426, (1974). "The shear strength of reinforced concrete members – slabs." *J. of the Struct. Div.*, 100, 1543-1591.
- Badie, S.S., Tadros, M.K., and Girgis, A.F., (2006). "Full-depth precast concrete bridge deck panel systems." *National Cooperative Highway Research Board Report 584*, Transportation Research Board, Washington, D.C.
- Beal, D.M., (1982). "Load capacity of concrete bridge decks." *J. of the Struct. Div.*, 108(ST4), 814-832.
- Biswas, M., (1986). "Precast bridge deck design systems." *PCI Journal*, 31(2), 40-94.
- Buth, E., Furr, H.L., and Jones, H.L., (1972). "Evaluation of a prestressed panel, cast-in-place concrete bridge." *Research Report 145-3*, Texas Transportation Institute, Texas A&M University, College Station.
- Csagoly, P.F., and Lybas, J.M., (1989). "Advanced design method for concrete bridge deck slabs," *ACI Conc. International*, 11(5), 53-63.

- Fagundo, F.E., Tabatabai, H., Soongswang, K., Richardson, J.M., and Callis, E.G., (1985). "Precast panel composite bridge decks." *ACI Conc. International*, 7(5), 59-65.
- Fallaha, S., Sun, C., Lafferty, M., and Tadros, M., (2004). "High performance precast concrete NUDECK panel system for Nebraska's Skyline Bridge." *PCI Journal*, 49(5), 40-50.
- Fang, I.K., Lee, J.H., and Chen, C.R., (1994). "Behavior of partially restrained slabs under concentrated load." *ACI Struct. J.*, 91(2), 133-139.
- Goldberg, D., (1987). "Precast prestressed concrete bridge deck panels." *PCI Journal*, 32(2), 26-45.
- Graddy, J.C., Kim, J., Whitt, J.H., Burns, N.H., and Klingner, R.E., (2002). "Punching-shear behaviour of bridge decks under fatigue loading." *ACI Struct. J.*, 99(3), 257-266.
- Henley, M.D., (2009). "Shear connections for the development of a full-depth precast concrete deck system". *Master of Science Thesis*, Texas A&M University, College Station, Texas.
- Hewitt, B.E., and Batchelor, B deV., (1975). "Punching shear strength of restrained slabs." *J. of the Struct. Div.*, 101(ST9), 1837-1853.
- Hieber, D.G, Wacker, J.M., Eberhard, M.O., and Stanton, J.F., (2005). "State-of-the-art report on precast concrete systems for rapid construction of bridges." *Technical Report WA-RD 594.1*, Washington State Transportation Center, University of Washington, Seattle.

Hornbeck, R.W., (1982). *Numerical methods*, QPI Series, Prentice Hall, New York.

Issa, M., Idriss, A., Kaspar, I., and Khayyat, S., (1995). "Full-depth precast, prestressed concrete bridge deck panels." *PCI Journal*, 40(1), 74-85.

Issa, M., Riberio do Valle, C.L., Abdalla, H.A., and Islam, S., (2003). "Performance of transverse joint grout materials in full-depth precast concrete bridge deck systems." *PCI Journal*, 48(4), 92-103.

Jones, H.L. and Furr, H.L., (1970). "Study of in-service bridges constructed with prestressed panel sub-decks." *Research Report 145-1*, Texas Transportation Institute, Texas A&M University, College Station.

Klingner, R.E. and Bieschke, L.A., (1988). "Effects of transverse panel strand extensions on the behavior of precast prestressed panel bridges." *PCI Journal*, 33(1), 68-88.

Lybas, J.M., Hays, C.O., and Guevara, J.O., (1990). "Further tests of the punching shear strength of lightly reinforced isotropic bridge decks." *Technical Report 0413-2488*, Florida Department of Transportation, University of Florida, Gainesville.

Mander, T.J., Henley, M.D., Scott, R.M., Hite Head, M., Mander, J.B., and Trejo, D., (2009). "Experimental investigation of full-depth precast overhang panels for concrete bridge decks." *ASCE Structures Congress*, Austin, Texas.

Mander, T.J., and Urmson, C.R., (2008). "Numerical models of reinforced concrete members." *CVEN621: Advanced Reinforced Concrete Design*, Texas A&M, College Station.

- Menegotto, E., and Pinto, P.E., (1973). "Method of analysis for cyclically loaded R.C. frames including changes in geometry and non-elastic behavior of elements under combined normal force and bending." *Int. Assoc. for Bridge and Struct. Eng. (IABSE) Rep.*, 13, 15-22.
- Merrill, B.D., (2002). "Texas' use of precast concrete stay-in-place forms for bridge decks." *TxDOT Concrete Bridge Conference*, Fort Worth, Texas.
- Mindess, S., Young, J.F., and Darwin, D., (2003). *Concrete*, Second Edition, Pearson Education Inc., Upper Saddle River, New Jersey.
- Mufti, A.A. and Newhook, J.P., (1998). "Punching shear strength of restrained concrete bridge deck slabs." *ACI Struct. J.*, 95(4), 375-381.
- Muratli, H., Klingner, R.E., and Graves, H.L., (2004). "Breakout capacity of anchors in concrete – part 2: shear." *ACI Struct. J.*, 101(6), 821-829.
- Nottingham, D., (1996). "Joint grouting in Alaskan bridges and dock decks." *Concrete International*, 18(2), 45-48.
- Olgaard, J., Slutter, R., and Fisher, J., (1971). "Shear strength of stud connectors in lightweight and normal weight concrete." *Eng. J. AISC*, 8(2), 55-64.
- Park, R., and Gamble, W.L., (2000). *Reinforced concrete slabs*, Second Edition, John Wiley & Sons, Inc., New York.
- Popovics, S., (1973). "A numerical approach to the complete stress-strain curve of concrete." *Cement and Concrete Research*, 3(4), 583-599.

- Scholz, D.P., Wallenfelsz, J.A., Lijeron, C., and Roberts-Wollmann, C.L., (2007). “Recommendations for the connection between full-depth precast bridge deck panel systems and precast I-beams.” *Report No. 07-CR17*, Virginia Transportation Research Council, Charlottesville.
- Shirvani, M., Klingner, R.E., and Graves, H.L., (2004). “Breakout capacity of anchors in concrete – part 1: tension.” *ACI Struct. J.*, 101(6), 812-820.
- Slutter, R.G. and Driscoll, G.C. (1965). “Flexural strength of steel-concrete composite beams.” *J. Struct. Eng.*, 91(2), 71-99.
- Sprinkel, M.M., (1985). “Prefabricated bridge elements and systems.” *NCHRP Synthesis 119*, Transportation Research Board, Washington D.C.
- Tadros, M.K. and Baishya, M.C., (1998). “Rapid replacement of bridge decks.” *NCHRP Report 407*, National Cooperative Highway Research Program, Washington D.C.
- Taly, N., (1998). *Design of Modern Highway Bridges*, McGraw-Hill Companies, Inc., New York.
- Taylor, R. and Hayes, B., (1965). “Some tests on the effect of edge restraint on punching shear in reinforced concrete slabs.” *Magazine of Concrete Research*, 17, 39-44.
- Texas Department of Transportation (TxDOT). (2004). *Standard Specifications for Construction and Maintenance of Highways, Streets and Bridges*, State Publications Clearinghouse, Item 421, 516-535, (available online).
- Trejo, D., Hite, M., Mander, J., Mander, T., Henley, M., Scott, R., Ley, T., and Patil, S., (2008). “Development of a precast bridge deck overhang system for the Rock Creek

Bridge.” *Technical Report 0-6100-2*, Texas Transportation Institute, Texas A&M University, College Station.

Tsui, C.K., Burns, N.H., and Klingner, R.E., (1986). "Behavior of Ontario-type bridge deck on steel girders: negative moment region and load capacity." *Research Report 350-3*, Center for Transportation Research Report, University of Texas at Austin.

Xue, W., Ding, M., Wang, H., and Luo, Z., (2008). “Static behavior and theoretical model of stud shear connectors.” *J. Bridge Eng.*, 13(6), 623-634.

Yamane, T., Tadros, M.K., Badie, S.S., and Baishya, M.C., (1998). “Full depth precast, prestressed concrete bridge deck system.” *PCI Journal*, 43(3), 50-66.

Zheng, Y., Robinson, D., Taylor, S., Cleland, D., and Shaat, A., (2008). “Analysis of compressive membrane action in concrete slabs.” *J. Bridge Eng.*, 161(1), 21-31.

APPENDIX I

FULL-DEPTH PRESTRESSED

OVERHANG PANEL DRAWINGS

FABRICATIONS NOTES:
 All concrete is Class H per TxDOT 2004 Standard Specification required. Minimum 28 day strength $f_c = 34$ MPa, and release strength 27 MPa.
 Panels design to AASHTO LRFD Bridge Design Specifications for HL93 loading
 Strands must be released with placement of Stage II concrete 24 hours later
 Remove laitance from top surface with light water blast before placement of Stage II
 All chamfers 20 mm

TRANSVERSE PANEL REINFORCEMENT:

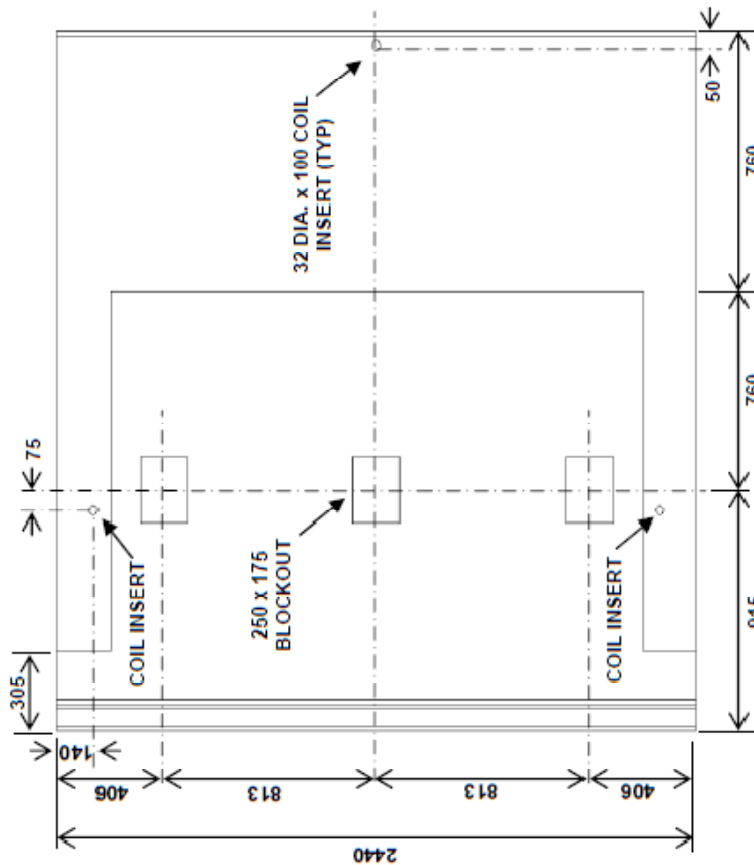
Stage I:
 Use 8.5 mm dia (1800 MPa) prestressing strands with an initial tension of 72 kN per strand.
 Place prestressing strands at panel centroid and space at 150 mm centers
 Prestressing strands intersecting the breakout shall be removed prior to shipping

Stage II:
 Reinforce and space as per drawings. Provide 50 mm clear cover to top surface of bars A1 and A2

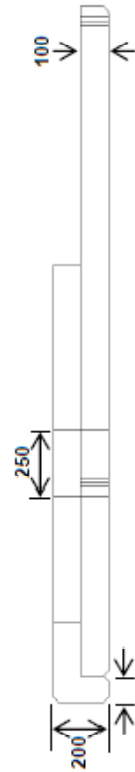
LONGITUDINAL PANEL REINFORCEMENT:

Stage I:
 Use deformed welded wire mesh (WWR) (ASTM A497) providing 485 mm²/m of panel width. Provide transverse wires to ensure handling of reinforcement. One splice per panel is allowed.

Stage II:
 Reinforce and space as per drawings, under transverse reinforcing



PLAN VIEW



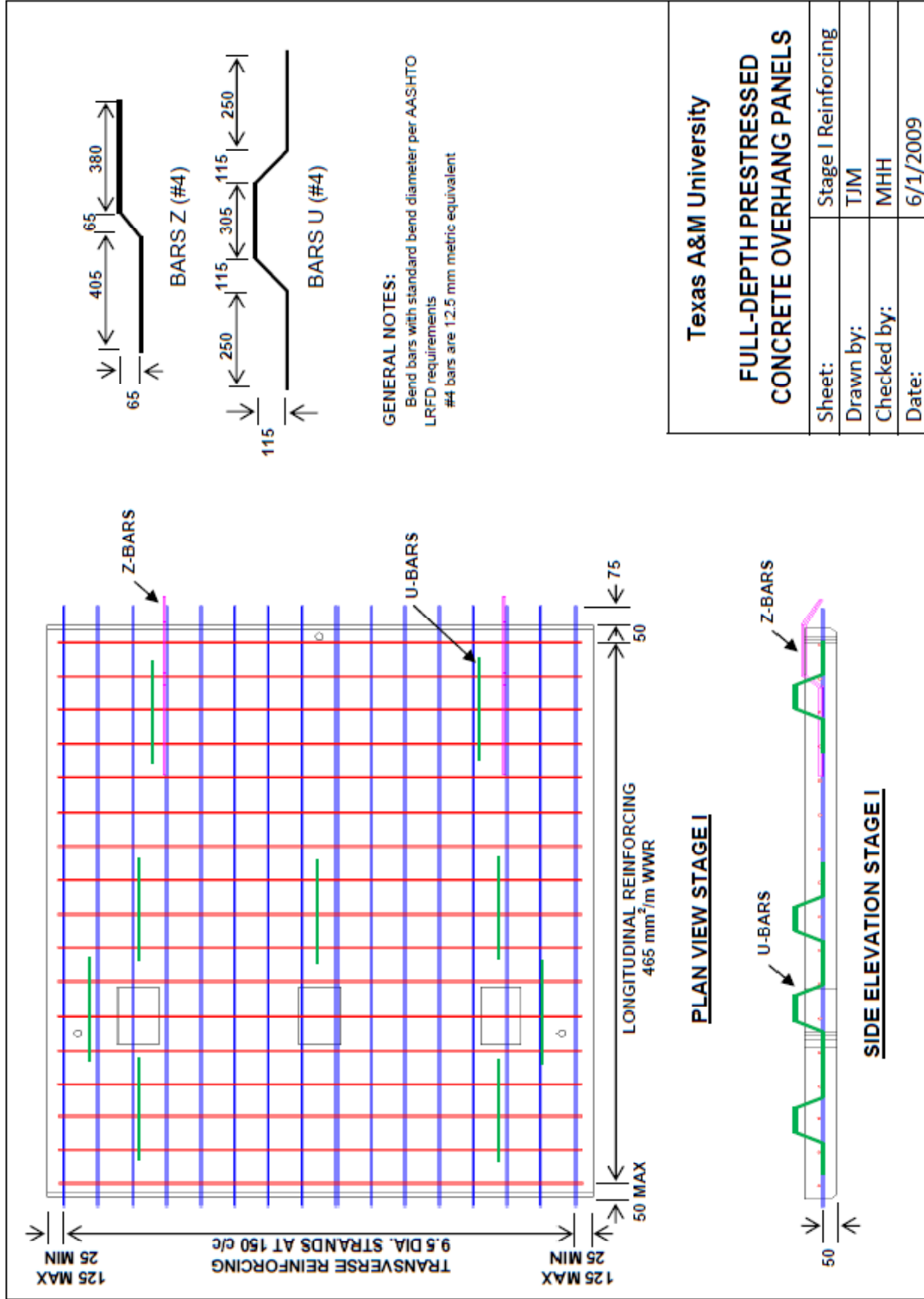
SIDE ELEVATION

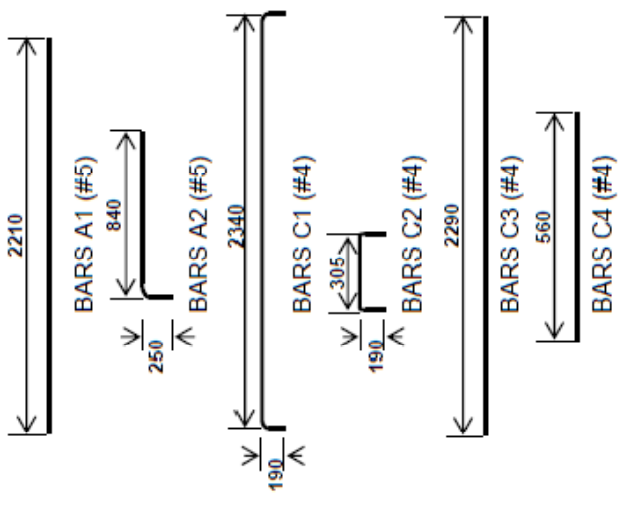
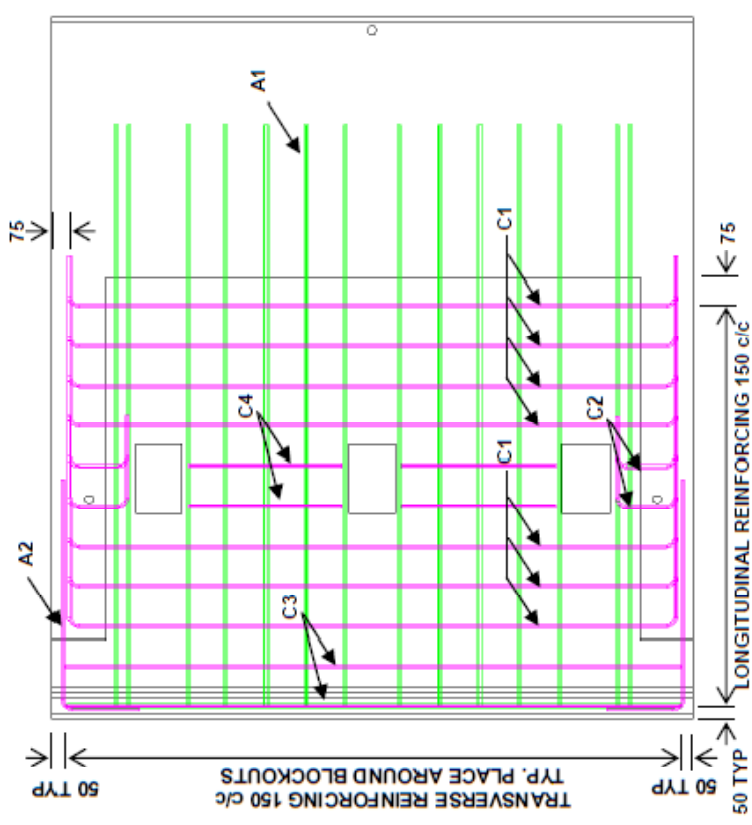
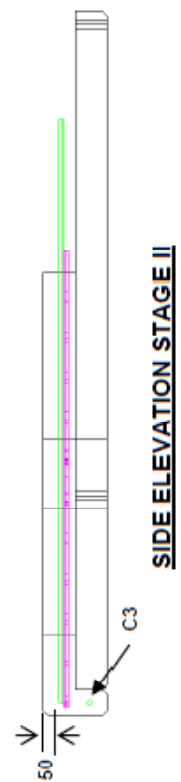
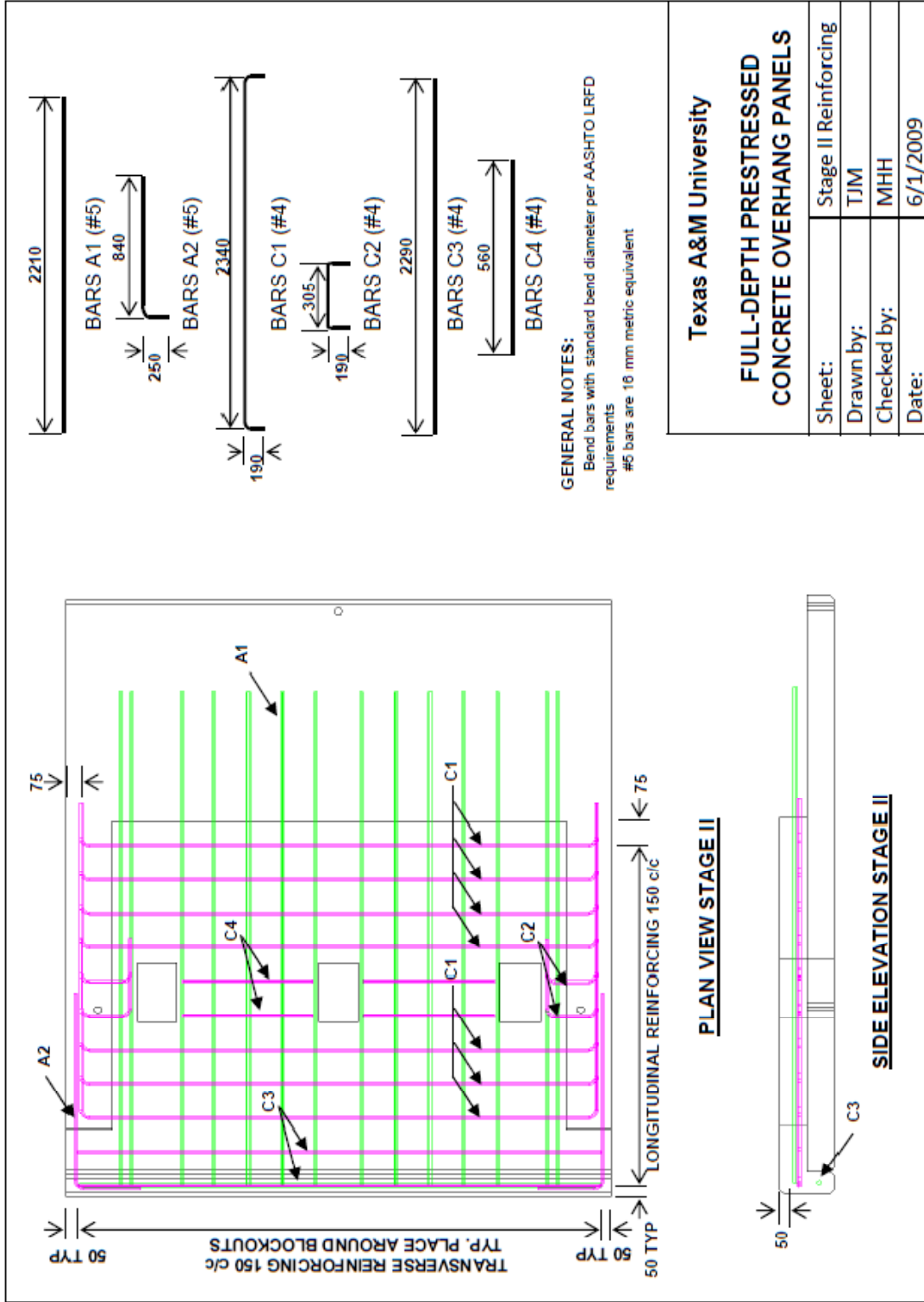
All dimensions given in mm

Texas A&M University

FULL-DEPTH PRESTRESSED CONCRETE OVERHANG PANELS

Sheet:	Dimensions only
Drawn by:	TJM
Checked by:	MHH
Date:	6/1/2009





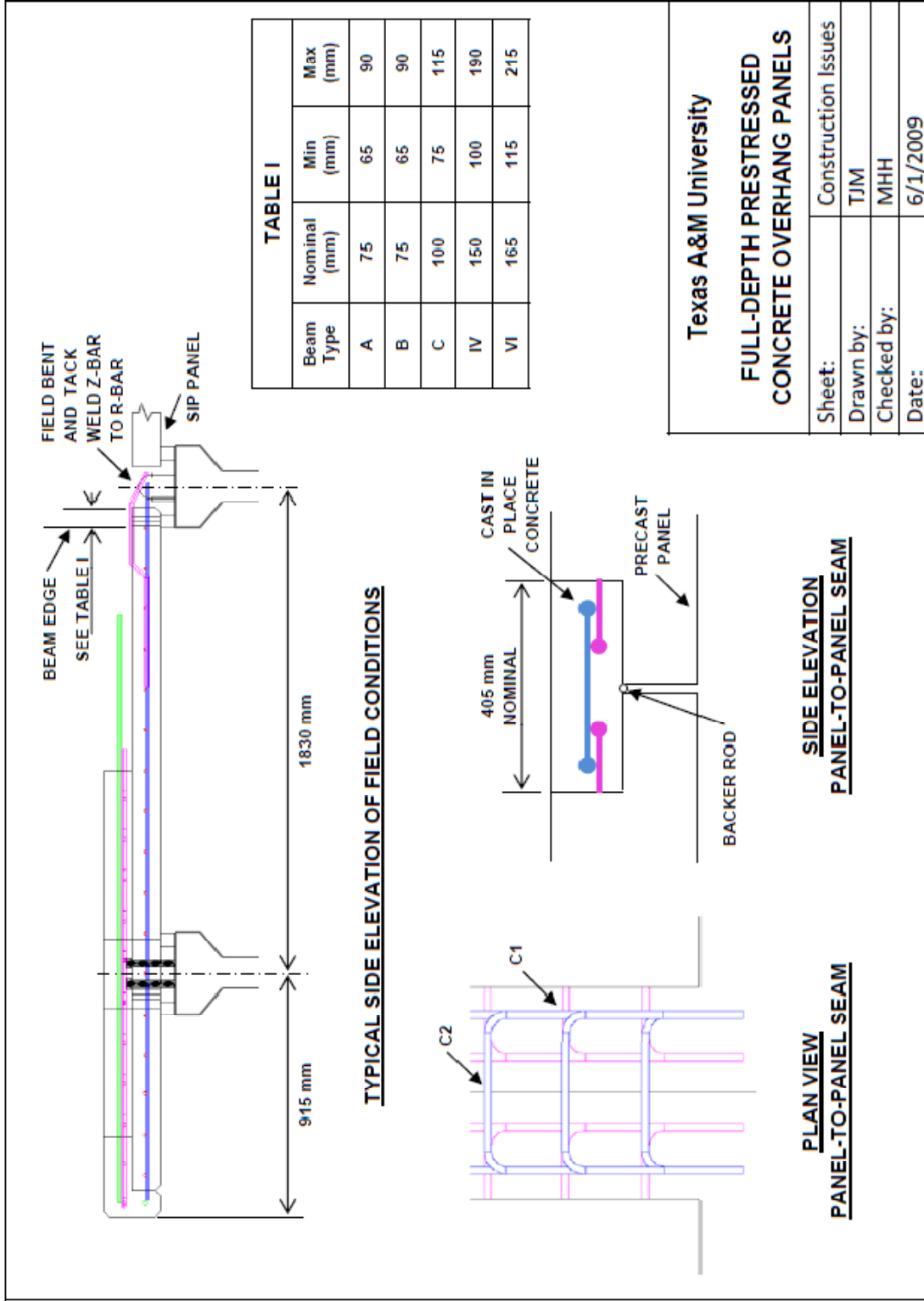


TABLE I

Beam Type	Nominal (mm)	Min (mm)	Max (mm)
A	75	65	90
B	75	65	90
C	100	75	115
IV	150	100	190
VI	165	115	215

Texas A&M University

FULL-DEPTH PRESTRESSED CONCRETE OVERHANG PANELS

Sheet: Construction Issues
 Drawn by: TJM
 Checked by: MHH
 Date: 6/1/2009

**SIDE ELEVATION
 PANEL-TO-PANEL SEAM**

**PLAN VIEW
 PANEL-TO-PANEL SEAM**

APPENDIX II
FINITE DIFFERENCE THEORY

Introduction

The experiments used a longitudinal and transverse line of displacement transducers to measure slab deflections. Using these vertical displacement measurements it is possible to infer curvatures using the method of finite differences. Because certain key displacements (such as the end of the slab) were not measured, and not all displacement transducers were evenly spaced it was necessary to develop new finite difference equations to solve for the curvature, ϕ , given by

$$\phi = \frac{d^2z}{dx^2} \quad (A1)$$

where z = measured deflection and x the position along the slab.

Unequally spaced nodes

For second-order accuracy two common cases may exist. For interior nodes, central differences are applied. In the case where the edge of the slab is approached forward or backward differences are applicable. These cases are represented schematically in Fig. A1. Formulae for central, forward and backward differences derived to allow for unequally spaced nodes using a factor, γ , to scale the standard spacing, Δx .

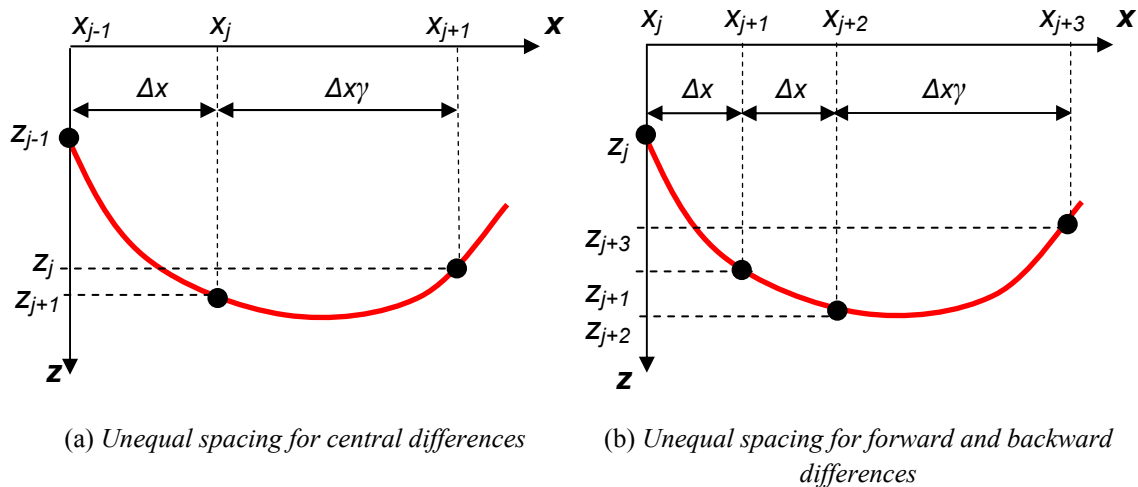


Fig. A1. Finite difference formulation for unevenly spaced nodes

Using a cubic polynomial, differentiating twice and solving for the coefficients leads to the following equations for central, forward, and backward differences,

$$\text{CENTRAL:} \quad z_j'' = \frac{z_{j-1} - (1+\gamma)z_j + \gamma z_{j+1}}{\frac{1}{2}\gamma\Delta x^2(\gamma+1)} \quad (A2)$$

$$\text{FORWARD:} \quad z_j'' = \frac{\gamma(\gamma+1)(\gamma+5)z_j - 2\gamma(\gamma+2)(\gamma+4)z_{j+1} + (\gamma+1)(\gamma+2)(\gamma+3)z_{j+2} - 6z_{j+3}}{\gamma\Delta x^2(\gamma+1)(\gamma+2)} \quad (A3)$$

$$\text{BACKWARD:} \quad z_j'' = \frac{\gamma(\gamma+1)(\gamma+5)z_j - 2\gamma(\gamma+2)(\gamma+4)z_{j-1} + (\gamma+1)(\gamma+2)(\gamma+3)z_{j-2} - 6z_{j-3}}{\gamma\Delta x^2(\gamma+1)(\gamma+2)} \quad (A4)$$

in which j = node number, z_j = deflection of the j^{th} node (etc), and Δx = spacing between nodes. The curvature at each node point along the slab can be written in matrix form, denoting the node at the free end as 1.

$$\{\phi\} = [C]\{z\} \quad (A5)$$

in which $\{\phi\} = \{\phi_1 \ \phi_2 \ \phi_3 \ \dots \ \phi_n\}^T$ (A6)

$$\{z\} = \{z_1 \ z_2 \ z_3 \ \dots \ z_n\}^T \quad (A7)$$

[C] = matrix of finite differences coefficients defined as

$$[C] = \frac{1}{(\Delta x)^2} \begin{bmatrix} 0.55 & -1.5 & 1.75 & -0.8 & 0 \\ 0.25 & -0.50 & 0.25 & 0 & 0 \\ 0 & 1 & -3 & 2 & 0 \\ 0 & 0 & 1 & -2 & 1 \\ 0 & -0.25 & 2.5 & -4 & 1.75 \end{bmatrix} \quad (A8)$$

Note that $\Delta x = 380$ mm, with γ modified according to the position of the node ($\gamma = 1/2$ or 2). The formulas used to derive (A8) are provided based on (A2) to (A4) using the appropriate value of γ . Equations following provide the finite difference coefficients.

CENTRAL using (A2):

Two cases exist:

(i) $\gamma = 2$

$$z_j'' = \frac{z_{j-1} - 3z_j + 2z_{j+1}}{3(\Delta x)^2}$$

(ii) $\gamma = 1/2$

$$z_j'' = \frac{8z_{j-1} - 12z_j + 4z_{j+1}}{12(\Delta x)^2}$$

FORWARD using (A3):

Two cases exist:

(i) $\gamma = 2$

$$z_j'' = \frac{7z_j - 16z_{j+1} + 10z_{j+2} - z_{j+3}}{4(\Delta x)^2}$$

(ii) $\gamma = 1/2$

$$z_j'' = \frac{2.2z_j - 6z_{j+1} + 7z_{j+2} - 3.2z_{j+3}}{4(\Delta x)^2}$$

BACKWARD using (A4):

Two cases exist:

(i) $\gamma = 2$

$$z_j'' = \frac{7z_j - 16z_{j-1} + 10z_{j-2} - z_{j-3}}{4(\Delta x)^2}$$

(ii) $\gamma = 1/2$

$$z_j'' = \frac{2.2z_j - 6z_{j-1} + 7z_{j-2} - 3.2z_{j-3}}{4(\Delta x)^2}$$

Equally spaced nodes

If $\gamma = 1$ is substituted into (A2) to (A4), the following well-known results are obtained for equally spaced nodes (Hornbeck, 1982):

$$\text{CENTRAL:} \quad z_j'' = \frac{z_{j-1} - 2z_j + z_{j+1}}{\Delta x^2} \quad (A9)$$

$$\text{FORWARD:} \quad z_j'' = \frac{2z_j - 5z_{j+1} + 4z_{j+2} - z_{j+3}}{\Delta x^2} \quad (A10)$$

$$\text{BACKWARD:} \quad z_j'' = \frac{2z_j - 5z_{j-1} + 4z_{j-2} - z_{j-3}}{\Delta x^2} \quad (A11)$$

These formulae can be applied to Specimen 2, which had a standard spacing for measured displacements of $\Delta x = 190$ mm. Boundary conditions need to be considered at the edge of the slab as neither moment nor shear exist, hence $z''(x = 0) = 0$ and $z'''(x = 0) = 0$, respectively. Let the (unmeasured) free end position be x_0 , with points x_1, x_2, x_3 and so on spaced uniformly from this point. From (A10), forward differences with no moment at the free end, $z''(x_0) = 0$

$$z_0''(x_0) = 0 = 2z_0 - 5z_1 + 4z_2 - z_3 \quad (A12)$$

Similarly, forward differences with no shear, $z'''(x_0) = 0$, leads to

$$z_0'''(x_0) = 0 = -5z_0 + 18z_1 - 24z_2 + 14z_3 - 3z_4 \quad (A13)$$

Combining (A12) and (A13) yields:

$$z_0 = 3.05z_1 - 3.4z_2 + 1.65z_3 - 0.3z_4 \quad (A14)$$

Substituting (A14) into (A9) leads to a solution for the first node point Δx from the end of the slab with the correct zero moment and shear boundary conditions:

$$z_1'' = \frac{1.05z_1 - 2.4z_2 + 1.65z_3 - 0.3z_4}{\Delta x^2} \quad (A15)$$

At the seam between the panels, there is shear and moment, permitting the forward or backward finite difference formulae to be used, as given by (A10) and (A11), respectively.

$$[C] = \frac{1}{(\Delta x)^2} \begin{bmatrix} 1.05 & -2.4 & 1.65 & -0.3 & 0 & 0 & 0 & 0 \\ 1 & -2 & 1 & 0 & 0 & 0 & 0 & 0 \\ 0 & 1 & -2 & 1 & 0 & 0 & 0 & 0 \\ 0 & 0 & 1 & -2 & 1 & 0 & 0 & 0 \\ 0 & 0 & 0 & 1 & -2 & 1 & 0 & 0 \\ 0 & 0 & 0 & 0 & 1 & -2 & 1 & 0 \\ 0 & 0 & 0 & 0 & 0 & 1 & -2 & 1 \\ 0 & 0 & 0 & 0 & 2 & -5 & 4 & -1 \end{bmatrix} \quad (A16)$$

where Δx = spacing between nodes, which was taken as 190 mm

APPENDIX III
MOMENT-CURVATURE THEORY

Introduction

In order to characterize the behavior of critical bridge deck sections subject to flexure, an algorithm was developed to compute the moment-curvature response for various reinforcing steel layouts. Measured material properties were implemented in the analysis and modeled using equations developed by Menegotto-Pinto (1973) and Popovics (1973). This appendix is adapted from work done by Mander and Urmson (2008) for moment-curvature analyses of reinforced concrete columns.

Material Modeling Procedures

Steel Behavior

A schematic diagram of the positive stress-strain curve for reinforcing steel is shown in Fig. A2. Behavior in the elastic region is defined by Young's Modulus, E_s , until it reaches the yield stress, f_y . A yield plateau may occur after which strain-hardening commences at the strain-hardening strain, ϵ_{sh} . The stress increases as a function of the strain hardening modulus until the ultimate stress f_{su} is reached at the ultimate strain ϵ_{su} .

Numerical modeling of the steel stress-strain curve is achieved using the Menegotto-Pinto Equation (1973) in the elastic region and at the yield plateau. For behavior in the strain-hardening region, a power-law equation is used:

$$Y = X^P$$

where Y is the normalized change in stress, X is the normalized change in strain, and P is a shape parameter based on the slope of the strain-hardening curve. Thus combining with the Menegotto-Pinto Equation (1973) the stress-strain behavior of steel can be modeled using (A17):

$$f_s = \frac{E_s \varepsilon_s}{\left\{1 + \left|\frac{\varepsilon_s}{\varepsilon_y}\right|^{20}\right\}^{0.05}} + (f_{su} - f_{sy}) \left[1 - \frac{|\varepsilon_{su} - \varepsilon_s|^p}{\{|\varepsilon_{su} - \varepsilon_{sh}|^{20p} + |\varepsilon_{su} - \varepsilon_s|^{20p}\}^{0.005}}\right] \quad (\text{A17})$$

where

$$p = \frac{E_{sh}(\varepsilon_{su} - \varepsilon_{sh})}{(f_{su} - f_y)}$$

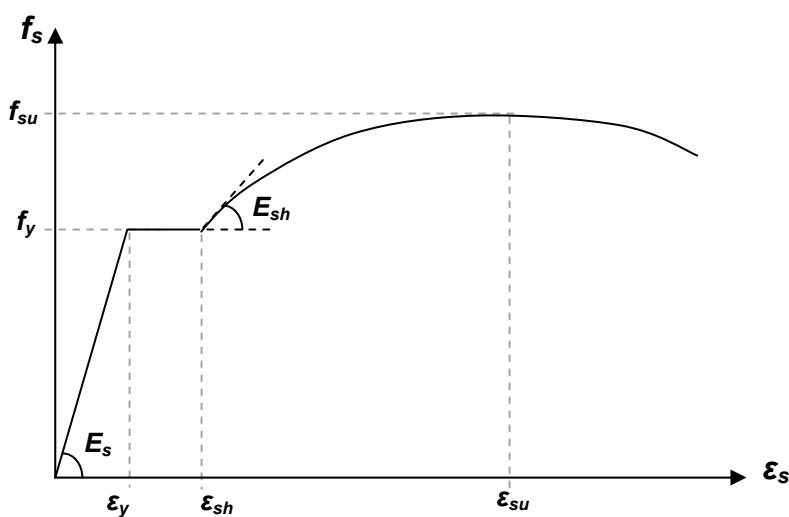


Fig. A2. Schematic representation of steel stress-strain behavior

The steel stress-strain curves provided in Chapter III of this thesis are individually modeled. Key parameters are determined by comparison with actual material test stress-strain plots. Fig. A3 shows the comparison between the measured properties and those modeled using the selected stress-strain parameters for the precast #4 (12.5 mm) mild reinforcing bars. It is evident that a clear correlation exists between the two plots. The values used for all other reinforcing steel are provided in Table A1. Stress-strain curves from Taly (1998) for 1800 MPa prestressing strand were used as they could not be accurately tested in the High Bay Structural and Materials Testing Laboratory.

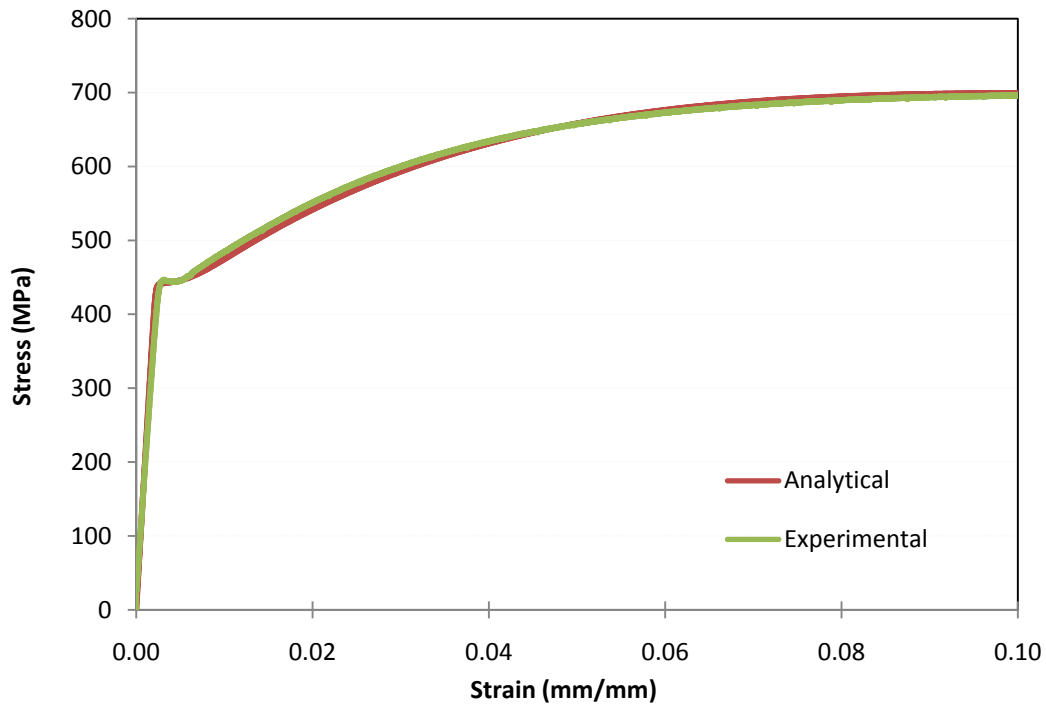


Fig. A3. Analytical and experimental stress-strain plots for the precast #4 (12.5mm) mild reinforcing

Table A1. Stress-strain properties used for modeling steel

STEEL TYPE	f_y MPa	f_{su} MPa	ϵ_y mm/mm	ϵ_{sh} mm/mm	ϵ_{su} mm/mm	E_{sh} MPa	ρ
CIP - #5	470	660	0.0024	0.012	0.2	6500	6.43
Precast -#5	420	690	0.0021	0.003	0.12	4500	1.95
CIP - #5	420	650	0.0021	0.01	0.15	5000	3.04
Precast - #4	440	700	0.0022	0.0058	0.12	8500	3.73
9.5 mm strand	1600	1900	0.0080	0.009	0.06	6500	1.11

Concrete Behavior

Fig. A4 presents a schematic of the stress-strain behavior of unconfined concrete. Using Popovics's Equation (1973) the behavior is described using (A18) based on the

compressive strength, f'_c , the compressive strain, the crushing strain ϵ_{co} , the initial chord Young's Modulus, E_{ci} , and the secant modulus, E_{sec} .

$$\frac{f'_c}{f_c} = \frac{n \left(\frac{\epsilon_c}{\epsilon_{co}} \right)}{n - 1 + \left(\frac{\epsilon_c}{\epsilon_{co}} \right)^n} \quad (\text{A18})$$

where

$$n = \frac{E_c}{E_c - E_{sec}} \quad \text{and} \quad E_{sec} = \frac{f'_c}{\epsilon_{co}}$$

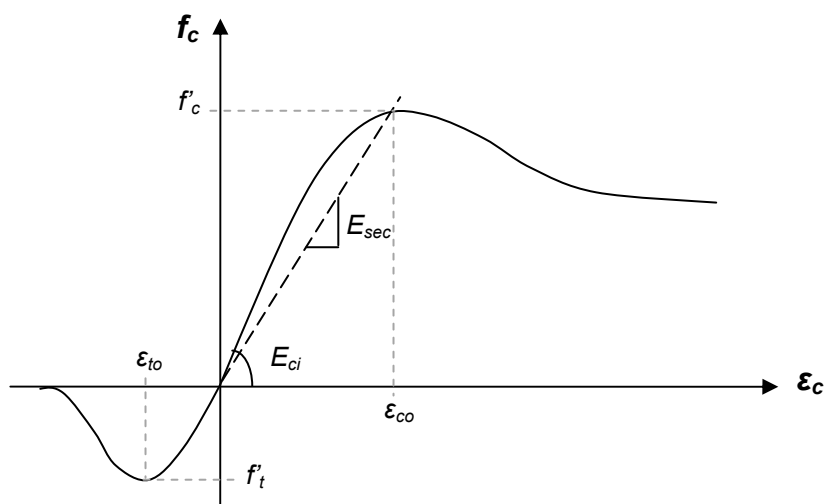


Fig. A4. Schematic representation of concrete stress-strain behavior

Uniaxial compression tests performed on the concrete cylinders presented in Chapter III only measured the compressive strength. Thus assumptions were made regarding the elastic modulus and compressive strain, based on ACI Committee 318 (2008) guidelines.

Moment-Curvature Analysis

Aim of Analysis and Mathematical Basis

Moment-curvature analyses are performed to relate the capacity of reinforced concrete deck sections in the form of bending moments to the deformation in the form of

curvatures. For the general case, the load-capacity relationship for a structural member can be described by the following relationship:

$$\begin{Bmatrix} N \\ M \end{Bmatrix} = \begin{bmatrix} EA & EZ \\ EZ & EI \end{bmatrix} \begin{Bmatrix} \varepsilon_0 \\ \phi \end{Bmatrix} \quad (\text{A19})$$

where N is the applied axial load, M is the applied bending moment, EA is the axial rigidity of the member, EI is the flexural rigidity of the member, EZ represents the non-linear coupling between axial load and bending moment, ε_0 is the strain of the section taken at some reference point, and ϕ is the curvature.

The form of (A19) is highly non-linear in the case of reinforced concrete, especially for post-yield behavior. Hence it can be written in differential form using partial derivatives to allow for this non-linearity:

$$\begin{Bmatrix} dN \\ dM \end{Bmatrix} = \begin{bmatrix} \frac{\partial N}{\partial \varepsilon} & \frac{\partial N}{\partial \phi} \\ \frac{\partial M}{\partial \varepsilon} & \frac{\partial M}{\partial \phi} \end{bmatrix} \begin{Bmatrix} d\varepsilon_0 \\ d\phi \end{Bmatrix} \quad (\text{A20})$$

An analytical solution of (A20) would require a continuous function of the quantities shown. Since this is almost impossible to find, a numerical approach is used in which the equation is solved incrementally. To do this, (A20) must be linearized for small increments of load and deformation:

$$\begin{Bmatrix} \Delta N \\ \Delta M \end{Bmatrix} = \begin{bmatrix} \frac{\partial N}{\partial \varepsilon} & \frac{\partial N}{\partial \phi} \\ \frac{\partial M}{\partial \varepsilon} & \frac{\partial M}{\partial \phi} \end{bmatrix} \begin{Bmatrix} \Delta\varepsilon_0 \\ \Delta\phi \end{Bmatrix} \quad (\text{A21})$$

Discretization of Section

In order to carry out a moment-curvature analysis, the axial load and bending moment acting on the section due to a given curvature and reference strain need to be computed. These can be found by integrating the stresses across the section as follows:

$$N = \int \sigma b_z dz \quad (\text{A22})$$

$$M = \int \sigma z b_z dz \quad (\text{A23})$$

In order to avoid complex analytical integration, the section is discretized as shown in Fig. A5. The strain profile for the entire section can be found for a given curvature and reference strain. Hence the bending moment and axial load in the section can be found for any given curvature and reference strain via numerical integration.

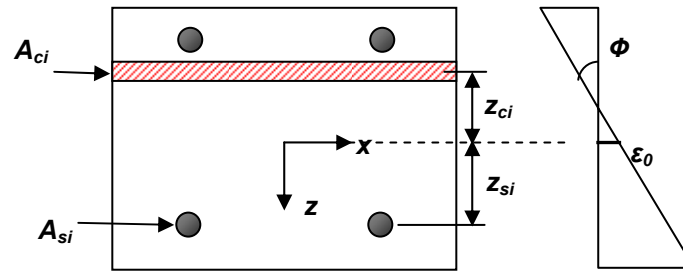


Fig. A5. Discretization of section and section strain

The discretized section consists of steel area elements, confined concrete area elements and unconfined concrete area elements. Each element has an associated depth y_i and area A_i which can be put into vectors for each type of element. Based on the section strain profile, the strain can be found in each element:

$$\varepsilon(z) = \varepsilon_0 + \phi z \quad (\text{A24})$$

or in vector form:

$$\{\varepsilon\} = \{\varepsilon_0\} + \phi\{z\} \quad (\text{A25})$$

Using the material stress-strain relationships previously described, the stress f_i in each element can be found. Using the trapezium rule to implement (A22) and (A23) numerically, we obtain the following expressions for P and M :

$$N = \sum_{i=1}^{ns} f_{si} A_{si} + \sum_{j=1}^{nc} f_{cj} A_{cj} \quad (\text{A26})$$

$$M = \sum_{i=1}^{ns} f_{si} A_{si} z_{si} + \sum_{j=1}^{nc} f_{cj} A_{cj} z_{cj} \quad (\text{A27})$$

Thus (A26) and (A27) can be rewritten in matrix form in order to improve computational efficiency:

$$N = \{f_s\}^T \{A_s\} + \{f_c\}^T \{A_c\} \quad (\text{A28})$$

$$M = \{f_s\}^T \{A_s\} \{z_s\} + \{f_c\}^T \{A_c\} \{z_c\} \quad (\text{A29})$$

Analysis Procedure

In order to compute the moment-curvature relationship of a reinforced concrete member, the second line of (A21) is used where successive increments of curvature $\Delta\phi$ are applied to the section, and the reference strain ε_o is modified so that the difference between the axial load in the section and the applied axial load is minimized. This is carried out in six steps as follows:

- STEP 1: An increment of curvature is added to the last successful solution, giving the new total curvature:

$$\phi_k = \phi_{k-1} + \Delta\phi \quad (\text{A30})$$

- STEP 2: The required change in reference strain is computed so that force equilibrium is achieved for the section under the new strain profile:

$$\Delta\varepsilon_{ok} = \frac{\Delta N - \left(\frac{\partial N}{\partial \phi}\right)_{k-1} \Delta\phi}{\left(\frac{\partial N}{\partial \varepsilon}\right)} \quad (\text{A31})$$

This is then added to the current reference strain to obtain the new total reference strain:

$$\varepsilon_{ok} = \varepsilon_{ok-1} + \Delta\varepsilon_{ok} \quad (\text{A32})$$

- STEP 3: The new strain profile is determined as given in (A25).
- STEP 4: The stresses are determined for each element and integrated across the section to obtain N using (A28). The out-of-balance axial load is obtained at this stage for use in the next iteration.
- STEP 5: The axial load tolerance limit is checked. If the axial load error is greater than that allowed for in the tolerance, the curvature step is set to zero, and Steps 2 to 5 are repeated until the axial load error is within the tolerance.
- STEP 6: When the tolerance is reached, M is calculated using (A29). The non-linear coupling term is then calculated for the next curvature step:

$$\left(\frac{\partial N}{\partial \phi}\right)_k = \frac{N_{k+\Delta\phi} - N_k}{\phi_{k+\Delta\phi} - \phi_k} \quad (\text{A33})$$

VITA

Thomas John Mander graduated from the University of Canterbury, New Zealand, as a Senior Scholar in November 2007 where he received his Bachelor of Engineering (Honors) from the Department of Civil Engineering. In January 2008 he began his Master of Science at Texas A&M in College Station, Texas as a Graduate Assistant Researcher for Dr. Monique Hite Head. He was in the structures program, from which he received his Master of Science degree in August 2009. His research interests include structural design and plastic analysis of concrete structures, and damage avoidance design of concrete and steel structures.

Thomas Mander is working as a Consultant in the Structures Section for Baker Engineering and Risk Consultants in San Antonio, Texas. He can be reached at BakerRisk, 3330 Oakwell Court, Suite 100, San Antonio, Texas 78218-3024. His email address is tman10usa@hotmail.com.